12-2013

Numerical Study of Hubbard Model for Iron-based Superconductors

Qinlong Luo
University of Tennessee - Knoxville, qluo@utk.edu

To the Graduate Council:

I am submitting herewith a dissertation written by Qinlong Luo entitled "Numerical Study of Hubbard Model for Iron-based Superconductors." I have examined the final electronic copy of this dissertation for form and content and recommend that it be accepted in partial fulfillment of the requirements for the degree of Doctor of Philosophy, with a major in Physics.

Elbio R. Dagotto, Major Professor

We have read this dissertation and recommend its acceptance:

Adriana Moreo, Norman Mannella, David Mandrus

Accepted for the Council:

Carolyn R. Hodges

Vice Provost and Dean of the Graduate School

(Original signatures are on file with official student records.)

Numerical Study of Hubbard Model for Iron-based Superconductors

A Dissertation Presented for the

Doctor of Philosophy

Degree

The University of Tennessee, Knoxville

Qinlong Luo

December 2013

To my family

Acknowledgments

Foremost, I would like to express my deepest appreciation to Professor Elbio Dagotto, who directed my dissertation and research projects, for his great patience, enthusiasm, and encouragement. Without his guidance, I would not be able to finish this dissertation. I could not imagine having a better advisor for my Ph.D study. In addition, I want to thank Professor Adriana Moreo, for her guidance on my research projects and insightful comments.

My sincere thanks also go to Dr. Rong Yu, Dr. Shuai Dong, Dr. Maria Daghofer, Dr. George Martins and Dr. Daoxin Yao who taught me physics and computer skills as well. I would like to thank Dr. Gonzalo Alvarez, for helping me develop my computer programs. I also want to thank my colleagues: Dr. Shuhua Liang, Dr. Andrew Nicholson, and Dr. Xiaotian Zhang for discussing with me and answering my questions. Additionally, a special thank you to Dr. Shuhua Liang for providing his great plotting software for free.

Finally, I would like to thank my family for their infinite support.

Abstract

This thesis addresses the numerical and analytical study of the iron-based superconductors, mainly using the multi-orbital Hubbard model and Hartree-Fock approximation. The text starts with an introduction to the new iron-based superconductors, followed by a theoretical description of the multi-orbital Hubbard model and Hartree-Fock approximations. The numerical study of the Hubbard model in momentum space is described next, where the phase diagrams for three- and five-orbital Hubbard models are provided. The physically "realistic" regime of couplings is highlighted, to guide future theoretical work into the proper region of parameters of Hubbard models for iron-based superconductors. What goes next is the numerical investigation of the two-orbital Hubbard model for the pnictides, using the real-space Hartree-Fock approximation on finite clusters. In this study, the charge stripes states are stabilized, upon electron doping. The observed patterns correspond to charge stripes oriented perpendicular to the direction of the spin stripes of the undoped magnetic ground state. After the iron pnictides, the numerical study of the magnetic state of $K_{0.8}Fe_{1.6}Se_2$ [potassium iron selenide] is presented, by applying the real-space Hartree-Fock approximation to the five-orbital Hubbard model. This study employed a 10×10 iron cluster with iron vacancies order. An insulating state with the same spin pattern as observed experimentally, involving 2×2 ferromagnetic plaquettes coupled with one another antiferromagnetically, is found to be stable in the phase diagram of the Hubbard model at intermediate Hubbard and Hund couplings. Another similar study of the magnetic state of the two-leg ladder selenide compound $BaFe_2Se_3$ [barium

iron selenide] has unveiled a dominant spin arrangement involving ferromagnetically ordered 2×2 iron-superblocks, that are antiferromagnetically coupled among them, and also another state with parallel spins along the rungs and antiparallel along the legs of the ladders. Both of these two states are observed via neutron scattering experiments. Finally, the magnetic phase diagram of a five-orbital Hubbard model for the iron-based superconductors is studied varying the electronic density n and the Hubbard interaction U, at a fixed Hund coupling $J/U = 0.25$. Several qualitative trends and a variety of competing magnetic states are observed in this investigation.

Table of Contents

List of Tables

List of Figures

Chapter 1

Introduction

1.1 Overview

The discovery of superconductivity in iron-based superconductors [Kamihara et al. (2008)] has attracted considerable interest in the condensed matter physics community [Johnston (2010); Dagotto (2013)]. The high-T_c superconductivity can be observed by doping or by pressurizing the undoped parent compound, which from the perspective of transport is a (bad) semimetal. The highest transition temperature T_c for iron-based superconductors is 56 K in $Gd_{1-x}Th_xFeAsO$ [Wang et al. (2008)].

This newly discovered superconductors share many similarities with the cuprates – the first high-T_c superconductors –, such as: both families have layered structures which are Fe-As layers for pnictides and Cu-O layers for cuprates; and both parent compounds are magnetic, with wavevector $(\pi, 0)$ in the case of the pnictides [Lynn and Dai (2009); Lumsden and Christianson (2010)] and (π, π) for the cuprates, in the notation of the square lattice defined by Fe or Cu. However, a significant difference between these two high-T_c superconductors is that the undoped parent compound is a Mott insulator for the cuprates, while it is a (bad) semimetal for the pnictides. This suggests that the regime of a large Hubbard coupling U, widely used in the context of

the cuprates, may not be appropriate for a theoretical description of the iron-based superconductors.

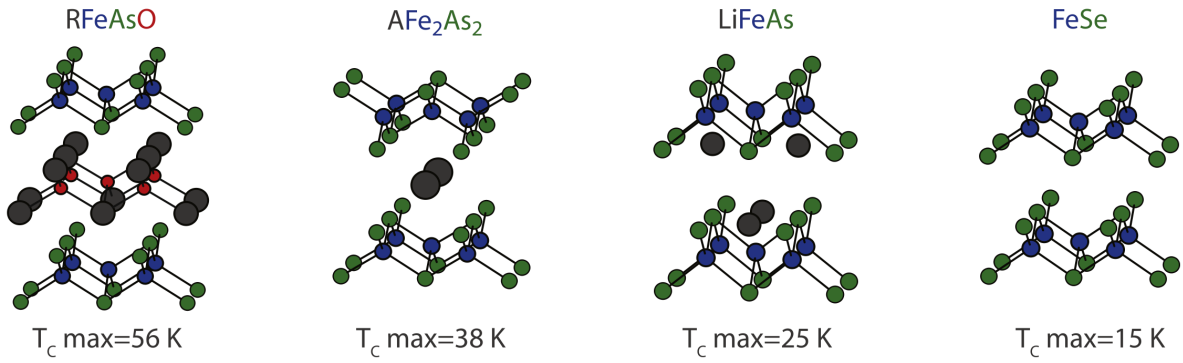

Figure 1.1: Crystal structure of the iron pnictides 1111, 122, 111, and 11 families. Blue solid balls represent Fe atoms and green ones represent As or Se atoms. Reproduced from Ref.[Lumsden and Christianson (2010)].

The superconductivity was first observed in iron pnictides ($LaFeAsO_{1-x}F_x$) in 2008 with $T_c = 26K$ [Kamihara et al. (2008)]. The undoped parent compounds of the iron pnictides all have similar layered structures, as shown in Fig.1.1. Generally, the crystal structures of these parent compounds are tetragonal at room temperature but become orthorhombic at low temperature. Indeed, the parent compounds undergo a tetragonal to orthorhombic structural transition accompanied by a magnetic transition which exhibits a SDW state below the transition temperature T_{SDW}. The structural phase transition is believed to be driven by magnetic interactions, as the lower symmetry allows the magnetic frustration to be relieved and the system to order [Lynn and Dai (2009)]. At low temperature, the magnetic structure within the a-b plane is identical for "1111" and "122" systems, as shown in Fig.1.2. It consists of chains of Fe spins which are parallel to each other along the shorter b-axis (typical spacing $5.68\mathring{A}$ in LaOFeAs [Lynn and Dai (2009)]), while the spins are coupled antiferromagnetically along the longer a-axis (typical spacing $5.71\mathring{A}$ in

LaOFeAs [Lynn and Dai (2009)]). The direction of the spins are along the a-axis. It is impossible for this type of magnetic structure to survive in tetragonal symmetry, which is the origin of the structural distortion. Typically, the magnetic moment is around 0.5 μ_B for "1111" system, except for CeFeAsO where it is 0.8 μ_B, whereas the magnetic moment of "122" system is slightly less than 1.0 μ_B. However, a big difference appears in the magnetic moment for the "11" systems which is around 2.0 μ_B (its wavevector is $(\frac{\pi}{2}, \frac{\pi}{2})$). The relatively small values of the magnetic moments observed for the parent compounds also indicate that the AF order is a spin-density-wave (SDW) arising from itinerant electrons [Johnston (2010)].

Experimentally, the phase diagrams (Fig.1.3) with hole or electron doping show the competitions between magnetism and superconductivity [Zhao et al. (2008); Luetkens et al. (2009); Drew et al. (2009); Margadonna et al. (2009); Chu et al. (2009); Khasanov et al. (2009)]. For some materials, such as CeFeAsO the magnetic order phase is completely suppressed by superconductivity with the doping of F [Zhao et al. (2008)]. For others, such as SmFeAsO, the magnetism is partly suppressed by superconductivity resulting in the coexistence of magnetism and superconductivity [Drew et al. (2009)], which is a very interesting feature of iron-based superconductors, as well as cuprates. It is believed that optimal superconductivity happens when the long-range SDW order is suppressed by doping or via pressure, but dynamic short-range antiferromagnetic spin correlations survive.

The iron-based superconductors have a very complicated band dispersion, which contributes to very interesting Fermi surface (FS) as well. The angle-resolved photoemission spectroscopy (ARPES) is a powerful technique to study these materials, which can provide considerable detailed information about the electronic structure. A typical Fermi surface of $BaFe_2As_2$ in the SDW state [Yi et al. (2009)] is shown in Fig.1.4. The observed Fermi surfaces contain two hole-like pockets around the center of the Brillouin zone (BZ) and one electron-like pocket around the corners. Beside these pockets, four "satellite" pockets can be observed around the hole pockets, due to the cross-shaped band near the Γ point.

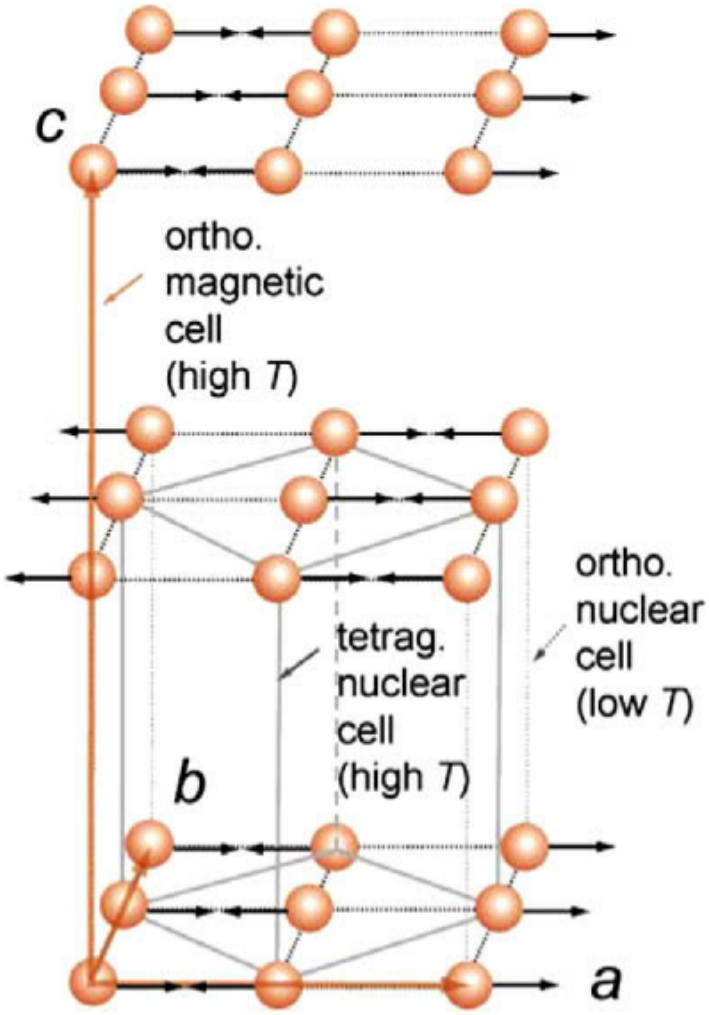

Figure 1.2: Magnetic structure for the iron spins in the "1111" and "122" systems. The in-plane spin configuration and spin direction are identical for all these materials, where the spins are parallel along the orthorhombic b-axis, antiparallel along the a-axis, and with the spin direction along a. Along the more weakly coupled c-axis the arrangement can be either parallel (ferro) or antiparallel (antiferro). All the structures are simple commensurate magnetic structures. Reproduced from Ref.[Lynn and Dai (2009)].

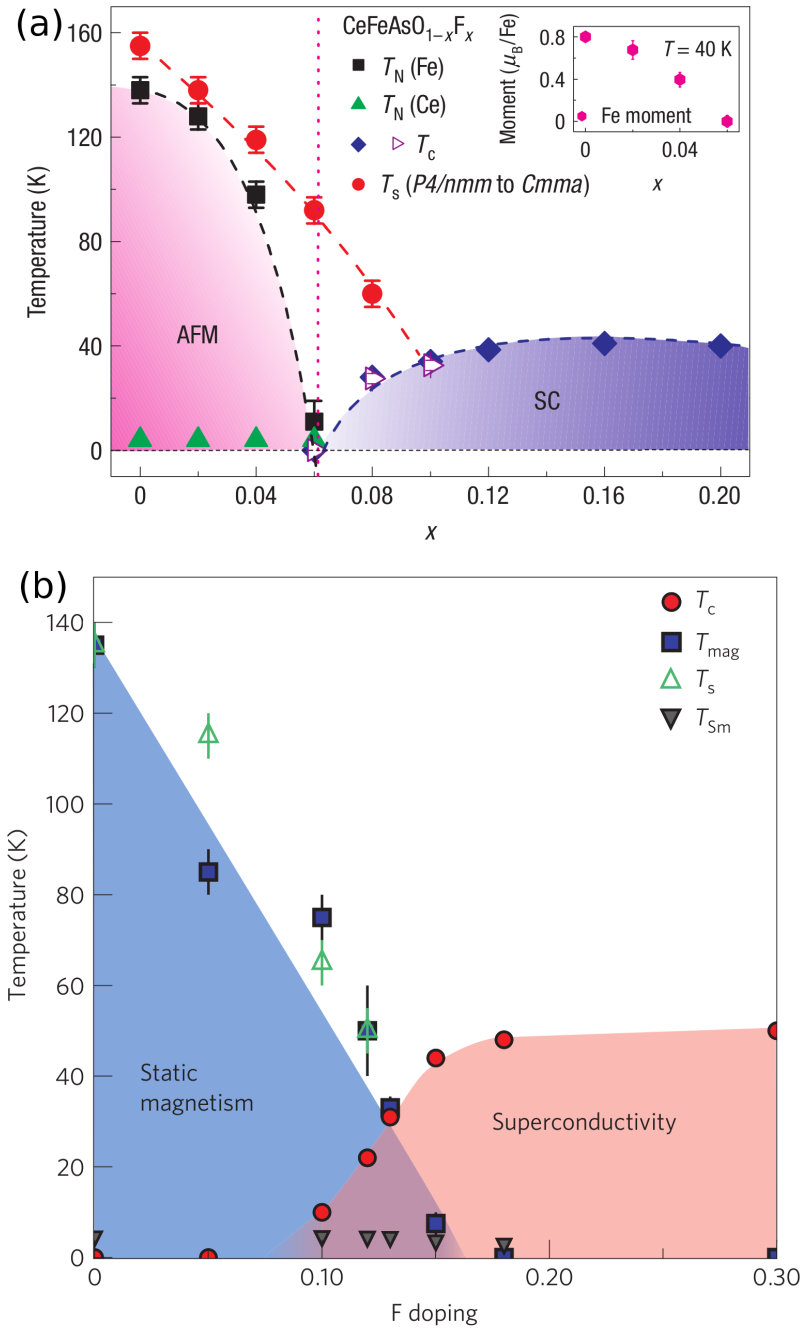

Figure 1.3: Experimentally determined phase diagram for (a) CeFeAsO and (b) SmFeAsO. Reproduced from Ref.[Zhao et al. (2008)] and Ref.[Drew et al. (2009)].

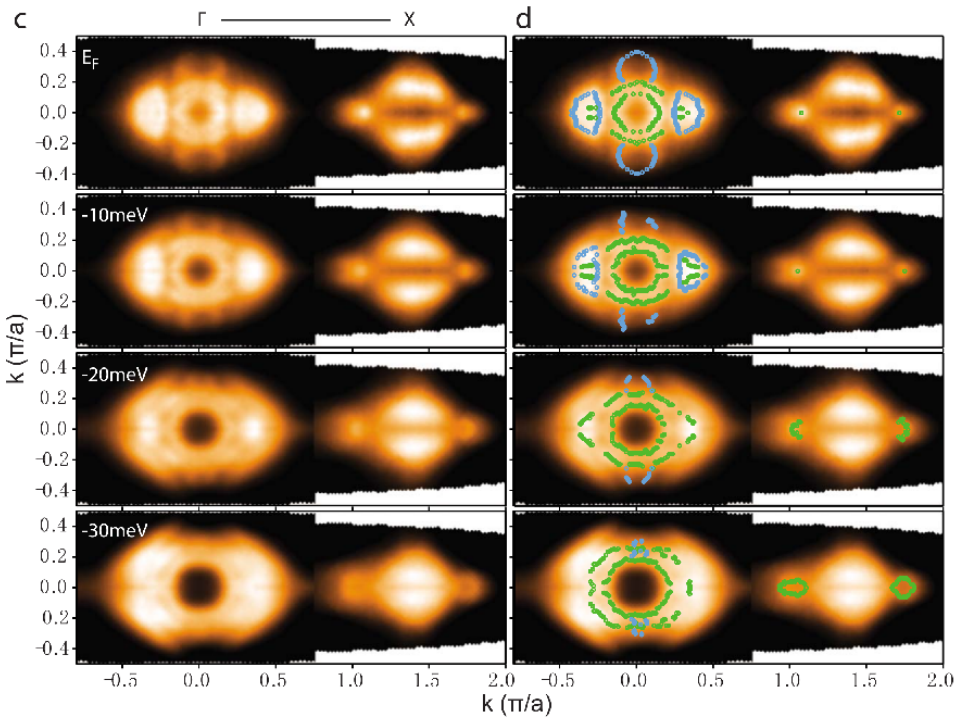

Figure 1.4: Constant energy mapping of $BaFe_2As_2$ in the SDW state, measured at $T = 20K$. (c) Constant energy maps across the Γ-X region at E_B=0, 10 meV, 20 meV, and 30 meV. (d) Maps in (c) overlaid with dots marking the constant energy contours of the bands. Green marks donote hole-like features while blue marks denote electron-like features. Reproduced from Ref.[Yi et al. (2009)].

Among the most exciting developments in the field of Fe-based superconductors is the discovery of superconductivity with $T_c \sim 30$ K in the heavily electron-doped 122 iron chalcogenides $K_{0.8}Fe_{2-x}Se_2$ and (Tl,K)$Fe_{2-x}Se_2$ compounds [Guo et al. (2010)]. A typical crystal structure is shown in Fig.1.5, which shows a similar layered structure as iron pnictides. However, these materials contain ordered Fe vacancies in the FeSe layers, increasing the complexity of these systems.. At the special composition $K_{0.8}Fe_{1.6}Se_2$ with the iron vacancies in a $\sqrt{5} \times \sqrt{5}$ arrangement, neutron scattering studies [Bao et al. (2011); Ye et al. (2011)] of this (insulating) compound have revealed an unusual magnetic order. This magnetic state involves 2×2 iron blocks with their four spins ferromagnetically ordered, large ordering temperatures, and concomitant large magnetic moments $\sim 3.3\ \mu_B$/Fe. The 2×2 blocks are antiferromagnetically coupled among them. Phase separation tendencies have also been reported in this type of insulators [Ricci et al. (2011)].

Some photoemission experiments have been carried out for the iron selenides, showing the absence of hole pockets at the center of the FS. For example, ARPES experiment for (Tl, K)$Fe_{1.78}Se_2$ revealed a Fermi surface (shown in Fig.1.6) with only electron-like pockets at wavevectors $(\pi, 0)$ and $(0, \pi)$ [Wang et al. (2011b)], showing that the Fermi surface nesting of hole and electron pockets is not sufficient to understand these materials [Dai and Dagotto (2012)]. Moreover, the resistivity of these materials displays a behavior corresponding to an insulator in a robust range of the Fe concentration x, suggesting that SC may arise from the doping of a Mott insulator, as in the cuprates [Fang et al. (2011)].

Recent experiments have shown the possibility of phase separation in the iron Chalcogenides, which can explain some puzzling properties of these compounds. Two competing phases are observed experimentally in several length scales, including a superconducting (SC) phase without iron-vacancies and a magnetic phase with iron-vacancies. Ref. [Chen et al. (2011)] reported that ARPES and high-resolution TEM results showed phase separation at nanometer scale between SC and semiconducting phases and the AFM insulating phases, and one of the insulating phases has the

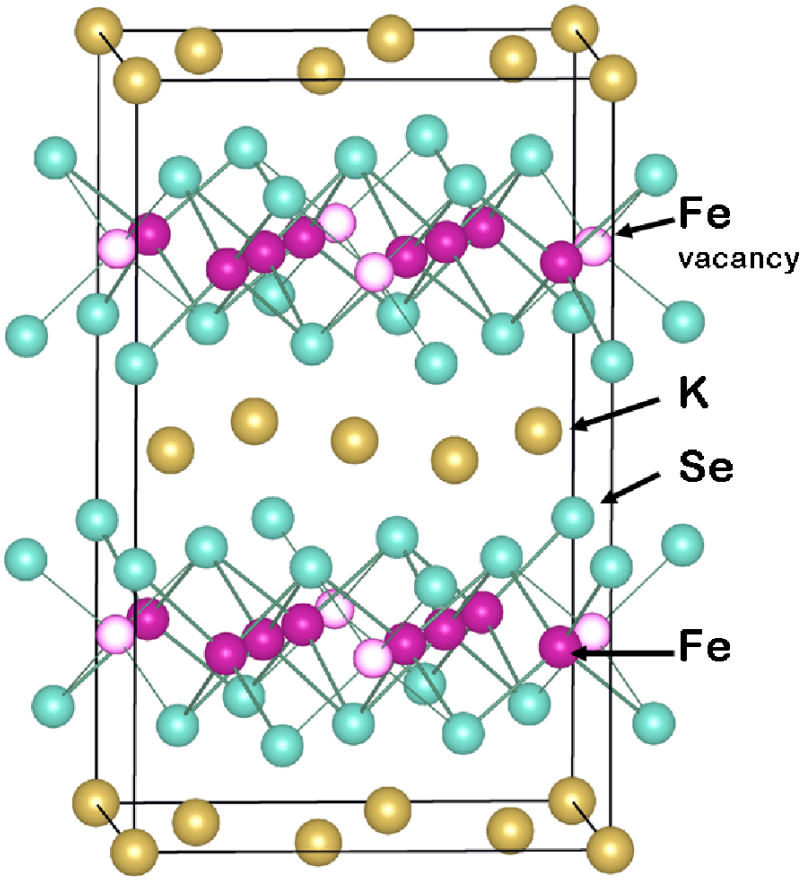

Figure 1.5: Crystal structure of $A\mathrm{Fe}_x\mathrm{Se}_2$, where A is an alkali metal element (K in the figure). Iron vacancies will show up if $x<2$. Reproduced from Ref.[Bao et al. (2011)]

$\sqrt{5} \times \sqrt{5}$ iron-vacancy order. Moreover, Scanning Tunneling Microscopy (STM) results have also shown two phases in thin films of $K_xFe_{2-y}Se_2$: an insulating phase with $\sqrt{5} \times \sqrt{5}$ iron-vacancy order and a vacancy-free SC phase with the composition KFe_2Se_2 [Wei Li and Xue (2012)]. Another STM study of $K_{0.73}Fe_{1.67}Se_2$ by [Cai et al. (2012)] showed the coexisting of the SC phase and a so-called $\sqrt{2} \times \sqrt{2}$ charge-density modulation microscopically. Phase separation in alkali iron selenides are also reported from Raman scattering, transmission electron microscopy and optical spectroscopy experiments. Some other techniqes (muon-spin rotation and x-ray) are also used to investigate these compounds and demonstrated the coexistence of the SC phase and magnetic phase. For a detail review of alkali iron selenides, please refer to [Dagotto (2013)] and references therein.

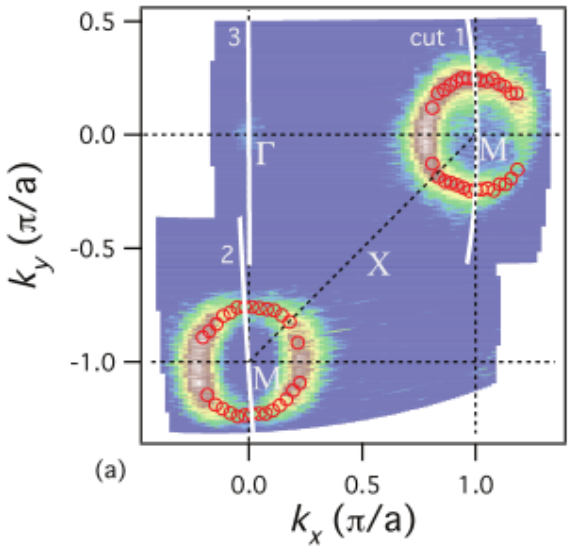

Figure 1.6: Momentum-resolved photoemission intensity mapping of $Tl_{0.63}K_{0.37}Fe_{1.78}Se_2$ in the normal state, measured at $T = 20K$. Reproduced from Ref.[Wang et al. (2011b)].

Several theoretical efforts have also addressed the exotic magnetic state that appears in the presence of vacancies. Band structure calculations described this state

as an antiferromagnetic insulator with a gap ∼0.4-0.6 eV [Cao and Dai (2011a,b); Yan et al. (2011)]. Several model Hamiltonian calculations have also been presented and, in particular, two publications are important to compare our results against. Yu et al. (2011) analyzed this problem using a phenomenological J_1-J_2 spin model (see also Ref.[Cao and Dai, 2011a,b]) with nearest-neighbors (NN) and next-NN terms superexchange couplings, studied via classical Monte Carlo. In this analysis the couplings inside the 2×2 plaquettes and those between plaquettes were allowed to be different, and also to take positive or negative values. Five antiferromagnetic phases, including the phase found experimentally [Bao et al. (2011)] in $K_{0.8}Fe_{1.6}Se_2$, which was dubbed "AF1", were found varying the J_1 and J_2 couplings [Fang et al. (2012)]. From a different perspective that relies on a two-orbital (d_{xz} and d_{yz}) spin-fermion model for pnictides, and with tetramer lattice distortion incorporated, Yin et al. (2012) studied the regime of electronic density n=1 (one electron per Fe), where they also reported the presence of an AF1 state, found competing with a "C" type state with wavector $(\pi, 0)$.

Recently, considerable interest was generated by studies of $BaFe_2Se_3$ (the "123" compound) [Svitlyk et al. (2013); Caron et al. (2011); Lei et al. (2011); Saparov et al. (2011); Caron et al. (2012); Nambu et al. (2012)], since this material contains chains made of $[Fe_2Se_3]^{2-}$ building blocks separated by Ba. These effective two-leg iron ladders in $BaFe_2Se_3$ are cut-outs of the layers of edge-sharing $FeSe_4$ tetrahedra normally found in layered chalcogenides. Each double chain consists of pairs of iron atoms (the "rungs") located one next to the other forming a one dimensional arrangement perpendicular to those rungs, defining indeed a two-leg ladder structure, which increase the similarity to the Cu-oxide high-T_c superconductors. The Cu-oxide-ladder spin state is dominated by rung spin-singlets, and a tendency to superconduct upon doping [Dagotto et al. (1992); Dagotto and Rice (1996)]. In particular, the compound $SrCu_2O_3$ is the Cu-based analog of $BaFe_2Se_3$ [Dagotto (1999)].

The $BaFe_2Se_3$ "ladder" compound is an insulator, with a resistivity displaying an activation energy between Δ∼0.13 eV [Nambu et al. (2012)] and Δ∼0.178 eV

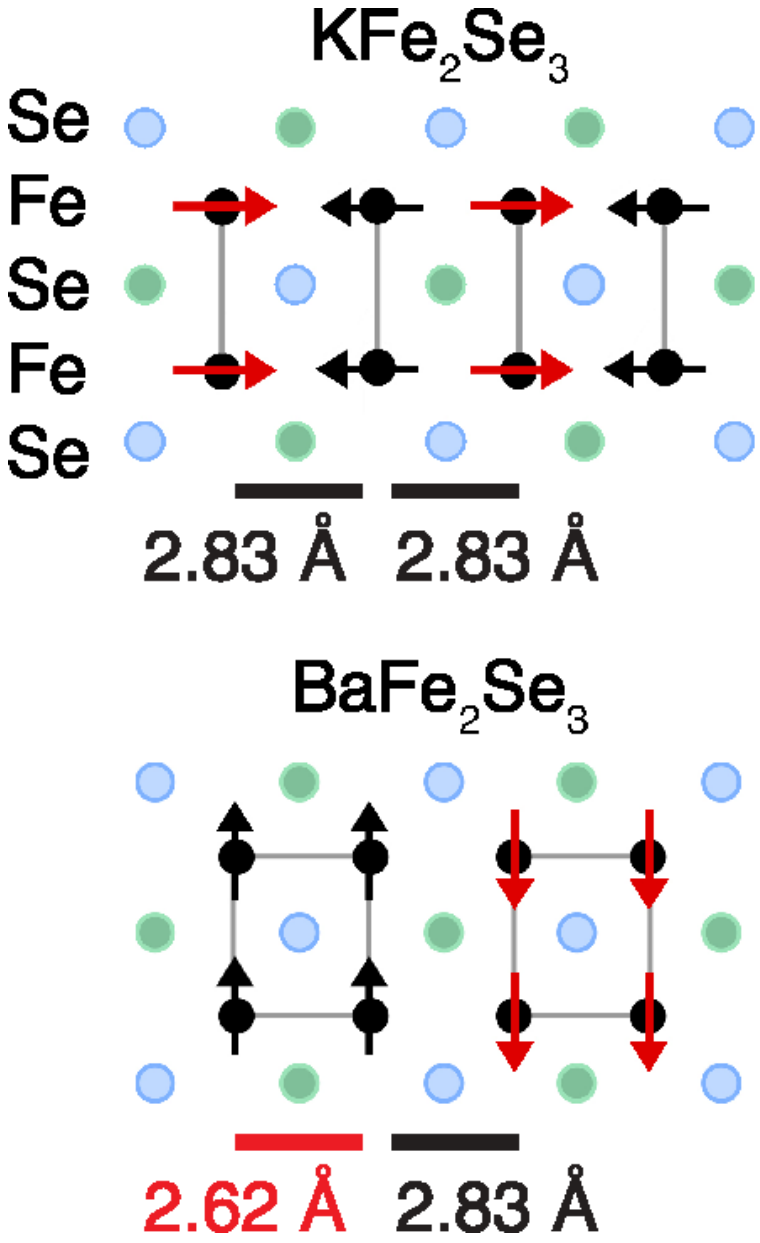

Figure 1.7: Magnetic order of the two-leg ladders for the cases of KFe_2Se_3 and $BaFe_2Se_3$ obtained using neutron diffraction. Reproduced from Ref.[Caron et al. (2012)].

[Lei et al. (2011)]. It has long-range antiferromagnetic (AFM) order at ∼250 K, with low-temperature magnetic moments ∼2.8 μ_B, and it displays short-range AFM correlations at higher temperatures (in particular ξ∼35Å at room-T) [Caron et al. (2011); Lei et al. (2011); Saparov et al. (2011)]. Upon cooling, the magnetic order presumably settles along the ladder directions first, and then weaker interladder interactions establish the long-range order. Neutron diffraction studies [Caron et al. (2011); Nambu et al. (2012)] reported a dominant magnetic order at low-T involving blocks of four iron atoms with their moments aligned, coupled antiferromagnetically along the ladder direction (Fig.1.7). The ferromagnetic 2×2 building blocks present in the block-AFM state of the ladders are the same blocks reported before in $K_{0.8}Fe_{1.6}Se_2$, with the iron vacancies in the $\sqrt{5}\times\sqrt{5}$ distribution. When the 123-ladder material is doped with K as in $Ba_{1-x}K_xFe_2Se_3$, experimentally it is known that the magnetic state evolves from the block-AFM state, through a spin glass, eventually arriving for KFe_2Se_3 to the spin state also displayed in Fig.1.7, where the spins in the same rung are coupled ferromagnetically but they are antiferromagnetically ordered in the long ladder direction [Caron et al. (2012)]. Note that in $BaFe_2Se_3$ the valence of Fe is expected to be 2+, if those of Ba and Se are +2 and -2, respectively, giving an electronic density n=6.0. But in KFe_2Se_3, K has valence +1, thus rendering the average valence of Fe to be +2.5, that corresponds to an electronic density n=5.5.

Beside the "ladder" materials, another novel avenue of research motivated by the iron-based superconductors has been expanding. It consists of replacing entirely Fe by another 3d transition element such as Mn or Co. The average electronic population of these elements in the new compounds is different from that of iron, but the crystal structures are similar. In the case of the 100% replacement of Fe by Mn, the compound $BaMn_2As_2$ was found to develop a G-type antiferromagnetic (AFM) state with staggered spin order, a Néel temperature of 625 K, and a magnetic moment of 3.88μ_B/Mn at low temperatures [Singh et al. (2009)]. The G-type AFM order is very robust, as recent investigations of $Ba_{1-x}K_xMn_2As_2$ have unveiled [Lamsal et al. (2013)]. This state emerges naturally from the population n=5 at each Mn atom,

namely one electron per $3d$ orbital. In the other limit of full Co substitution for Fe, such as for the case of $SrCo_2As_2$, the material has a complex Fermi surface and there are tendencies to magnetic order in the form of spin fluctuations in the C-type channel [Jayasekara et al. (2013)], although $ab-initio$ calculations suggest that a ferromagnetic instability can also occur. Note that ferromagnetic tendencies have been reported for LaCoOX (X=P,As) as well [Yanagi et al. (2008)].

Chapter 2

Models and Techniques

2.1 Multi-orbital Hubbard Model

In order to study the magnetic and superconducting properties of the pnictides, a considerable effort has already started using multiorbital model Hamiltonians [Raghu et al. (2008); Kuroki et al. (2008); Daghofer et al. (2008); Korshunov and Eremin (2008); Si and Abrahams (2008); Seo et al. (2008); Lorenzana et al. (2008); Yu et al. (2009); Sknepnek et al. (2009); Moreo et al. (2009b,a); Graser et al. (2009); Chen et al. (2009); Caldern et al. (2009); Bascones et al. (2010); Lee et al. (2009); Lee and Wen (2008); Laad and Craco (2009); Daghofer et al. (2010b); Wang et al. (2010); Daghofer et al. (2010a)]. From ARPES experiments and *ab-initio* calculations for Fe-based materials, all five d-orbitals of Fe dominate the bands near the Fermi energy, while the As $4p$ orbitals contribute more to the bands below the Fermi energy [Cao et al. (2008)]. Therefore, it is reasonalbe to employ multi-orbital Hubbard models to investigate these iron-based supercoductors, including Two-, Three- and Five-orbital Hubbard models.

The total Hamiltonian is $H = H_{\rm TB} + H_{\rm int}$. The first term is the kinetic energy $H_{\rm TB}$, and it reads:

$$H_{\rm TB} = \sum_{<\mathbf{i},\mathbf{j}>} \sum_{\alpha,\beta,\sigma} t_{ij}^{\alpha\beta} (c^{\dagger}_{\mathbf{i},\alpha,\sigma} c_{\mathbf{j},\beta,\sigma} + h.c.), \tag{2.1}$$

where $c^{\dagger}_{\mathbf{i},\alpha,\sigma}$ creates an electron with spin σ in the orbital α of site $\mathbf{i}$, and $t_{ij}^{\alpha\beta}$ refers to the tunneling amplitude of a particle hopping from orbital α at site $\mathbf{i}$ to orbital β at site $\mathbf{j}$.

The second term is the Coulombic interaction H_{int}, reads:

$$\begin{aligned} H_{\text{int}} &= H_1 + H_2 + H_3 + H_4 \\ &= U\sum_{\mathbf{i},\alpha} n_{\mathbf{i},\alpha,\uparrow} n_{\mathbf{i},\alpha,\downarrow} + (U' - \frac{J}{2}) \sum_{\mathbf{i},\alpha<\beta} n_{\mathbf{i},\alpha} n_{\mathbf{i},\beta} - 2J \sum_{\mathbf{i},\alpha<\beta} \mathbf{S}_{\mathbf{i},\alpha} \cdot \mathbf{S}_{\mathbf{i},\beta} \\ &\quad + J \sum_{\mathbf{i},\alpha<\beta} (c^{\dagger}_{\mathbf{i},\alpha,\uparrow} c^{\dagger}_{\mathbf{i},\alpha,\downarrow} c_{\mathbf{i},\beta,\downarrow} c_{\mathbf{i},\beta,\uparrow} + h.c.), \end{aligned} \tag{2.2}$$

where $\mathbf{S}_{\mathbf{i},\alpha}$ ($n_{\mathbf{i},\alpha}$) is the spin (charge density) of orbital α at site $\mathbf{i}$, and $n_{\mathbf{i},\alpha} = n_{\mathbf{i},\alpha,\uparrow} + n_{\mathbf{i},\alpha,\downarrow}$. The first two terms ($H_1$ and H_2) give the energy cost of having two electrons located in the same orbital or in different orbitals, both at the same site, respectively. The third term (H_3) contains the Hund's rule coupling that favors the ferromagnetic (FM) alignment of the spins in different orbitals at the same lattice site. The "pair-hopping" term is in the forth term (H_4) and its coupling is equal to J by symmetry. The relation $U' = U - 2J$ between the Kanamori parameters has been used here [Dagotto et al. (2001)].

2.2 Hartree-Fock Approximation

2.2.1 Hartree-Fock Approximation in Real Space

To study the ground state properties of the multi-orbital Hubbard model, the Hartree Fock (HF) approximation will be applied to the Coulombic interaction. It will not affect the kinetic term since this kinetic term is already quadratic. The HF approximation is one kind of Mean-field approximation that includes two parts: the Hartree approximation and the Fock approximation. In the Hartree-Fock

approximation, a pair of operators can be replaced by a mean value, using the identity:

$$c^{\dagger}_{\mathbf{i},\alpha,\sigma}c_{\mathbf{i}',\alpha',\sigma'} = \langle c^{\dagger}_{\mathbf{i},\alpha,\sigma}c_{\mathbf{i}',\alpha',\sigma'}\rangle + (c^{\dagger}_{\mathbf{i},\alpha,\sigma}c_{\mathbf{i}',\alpha',\sigma'} - \langle c^{\dagger}_{\mathbf{i},\alpha,\sigma}c_{\mathbf{i}',\alpha',\sigma'}\rangle), \tag{2.3}$$

where the last term $c^{\dagger}_{\mathbf{i},\alpha,\sigma}c_{\mathbf{i}',\alpha',\sigma'} - \langle c^{\dagger}_{\mathbf{i},\alpha,\sigma}c_{\mathbf{i}',\alpha',\sigma'}\rangle$ can be considered as a fluctuation around the mean value, which is very small comparing to the mean value in the Hartree-Fock approximation. Therefore, the Hartree approximation of H_1 can be written as:

$$\begin{aligned} H_1^H &= U\sum_{\mathbf{i},\alpha} n_{\mathbf{i},\alpha,\uparrow}n_{\mathbf{i},\alpha,\downarrow} \\ &= U\sum_{\mathbf{i},\alpha}(\langle n_{\mathbf{i},\alpha,\uparrow}\rangle + n_{\mathbf{i},\alpha,\uparrow} - \langle n_{\mathbf{i},\alpha,\uparrow}\rangle) \times (\langle n_{\mathbf{i},\alpha,\downarrow}\rangle + n_{\mathbf{i},\alpha,\downarrow} - \langle n_{\mathbf{i},\alpha,\downarrow}\rangle) \\ &\approx U\sum_{\mathbf{i},\alpha}(n_{\mathbf{i},\alpha,\uparrow}\langle n_{\mathbf{i},\alpha,\downarrow}\rangle + n_{\mathbf{i},\alpha,\downarrow}\langle n_{\mathbf{i},\alpha,\uparrow}\rangle - \langle n_{\mathbf{i},\alpha,\uparrow}\rangle\langle n_{\mathbf{i},\alpha,\downarrow}\rangle) \end{aligned} \tag{2.4}$$

and the Fock approximation of H_1 can be written as:

$$\begin{aligned} H_1^F &= -U\sum_{\mathbf{i},\alpha}(c^{\dagger}_{\mathbf{i},\alpha,\uparrow}c_{\mathbf{i},\alpha,\downarrow})(c^{\dagger}_{\mathbf{i},\alpha,\downarrow}c_{\mathbf{i},\alpha,\uparrow}) \\ &= -U\sum_{\mathbf{i},\alpha}(\langle c^{\dagger}_{\mathbf{i},\alpha,\uparrow}c_{\mathbf{i},\alpha,\downarrow}\rangle + c^{\dagger}_{\mathbf{i},\alpha,\uparrow}c_{\mathbf{i},\alpha,\downarrow} - \langle c^{\dagger}_{\mathbf{i},\alpha,\uparrow}c_{\mathbf{i},\alpha,\downarrow}\rangle) \times \\ &\qquad (\langle c^{\dagger}_{\mathbf{i},\alpha,\downarrow}c_{\mathbf{i},\alpha,\uparrow}\rangle + c^{\dagger}_{\mathbf{i},\alpha,\downarrow}c_{\mathbf{i},\alpha,\uparrow} - \langle c^{\dagger}_{\mathbf{i},\alpha,\downarrow}c_{\mathbf{i},\alpha,\uparrow}\rangle) \\ &\approx -U\sum_{\mathbf{i},\alpha}(\langle c^{\dagger}_{\mathbf{i},\alpha,\uparrow}c_{\mathbf{i},\alpha,\downarrow}\rangle c^{\dagger}_{\mathbf{i},\alpha,\downarrow}c_{\mathbf{i},\alpha,\uparrow} + \langle c^{\dagger}_{\mathbf{i},\alpha,\downarrow}c_{\mathbf{i},\alpha,\uparrow}\rangle c^{\dagger}_{\mathbf{i},\alpha,\uparrow}c_{\mathbf{i},\alpha,\downarrow} - \langle c^{\dagger}_{\mathbf{i},\alpha,\uparrow}c_{\mathbf{i},\alpha,\downarrow}\rangle\langle c^{\dagger}_{\mathbf{i},\alpha,\downarrow}c_{\mathbf{i},\alpha,\uparrow}\rangle). \end{aligned} \tag{2.5}$$

Those terms of second order in the deviation from the mean-field values, which are ($n_{\mathbf{i},\alpha,\sigma}$ - $\langle n_{\mathbf{i},\alpha,\sigma}\rangle$), are all neglected in the Hartree-Fock approximation. In total, the Hartree-Fock approximation of H_1 can be written as the sum of the Hartree part

and Fock part:

$$
\begin{aligned}
H_1 \approx\ & U\sum_{\mathbf{i},\alpha}(n_{\mathbf{i},\alpha,\uparrow}\langle n_{\mathbf{i},\alpha,\downarrow}\rangle + n_{\mathbf{i},\alpha,\downarrow}\langle n_{\mathbf{i},\alpha,\uparrow}\rangle - \langle n_{\mathbf{i},\alpha,\uparrow}\rangle\langle n_{\mathbf{i},\alpha,\downarrow}\rangle) \\
& -U\sum_{\mathbf{i},\alpha}(\langle c^{\dagger}_{\mathbf{i},\alpha,\uparrow}c_{\mathbf{i},\alpha,\downarrow}\rangle c^{\dagger}_{\mathbf{i},\alpha,\downarrow}c_{\mathbf{i},\alpha,\uparrow} + \langle c^{\dagger}_{\mathbf{i},\alpha,\downarrow}c_{\mathbf{i},\alpha,\uparrow}\rangle c^{\dagger}_{\mathbf{i},\alpha,\uparrow}c_{\mathbf{i},\alpha,\downarrow} - \langle c^{\dagger}_{\mathbf{i},\alpha,\uparrow}c_{\mathbf{i},\alpha,\downarrow}\rangle\langle c^{\dagger}_{\mathbf{i},\alpha,\downarrow}c_{\mathbf{i},\alpha,\uparrow}\rangle).
\end{aligned} \tag{2.6}
$$

Following the same procedure as for H_1, the Hartree-Fock approximation to H_2 reads:

$$
\begin{aligned}
H_2 &= (U' - \frac{J}{2})\sum_{\mathbf{i},\alpha<\beta} n_{\mathbf{i},\alpha}n_{\mathbf{i},\beta} \\
&= (U' - \frac{J}{2})\sum_{\mathbf{i},\alpha<\beta}(n_{\mathbf{i},\alpha,\uparrow} + n_{\mathbf{i},\alpha,\downarrow})(n_{\mathbf{i},\beta,\uparrow} + n_{\mathbf{i},\beta,\downarrow}) \\
&= (U' - \frac{J}{2})\sum_{\mathbf{i},\alpha<\beta}(c^{\dagger}_{\mathbf{i},\alpha,\uparrow}c_{\mathbf{i},\alpha,\uparrow}c^{\dagger}_{\mathbf{i},\beta,\uparrow}c_{\mathbf{i},\beta,\uparrow} + c^{\dagger}_{\mathbf{i},\alpha,\uparrow}c_{\mathbf{i},\alpha,\uparrow}c^{\dagger}_{\mathbf{i},\beta,\downarrow}c_{\mathbf{i},\beta,\downarrow} \\
&\qquad +c^{\dagger}_{\mathbf{i},\alpha,\downarrow}c_{\mathbf{i},\alpha,\downarrow}c^{\dagger}_{\mathbf{i},\beta,\uparrow}c_{\mathbf{i},\beta,\uparrow} + c^{\dagger}_{\mathbf{i},\alpha,\downarrow}c_{\mathbf{i},\alpha,\downarrow}c^{\dagger}_{\mathbf{i},\beta,\downarrow}c_{\mathbf{i},\beta,\downarrow}) \\
&\approx (U' - \frac{J}{2})\sum_{\mathbf{i},\alpha<\beta}[(n_{\mathbf{i},\alpha,\uparrow} + n_{\mathbf{i},\alpha,\downarrow})(\langle n_{\mathbf{i},\beta,\uparrow}\rangle + \langle n_{\mathbf{i},\beta,\downarrow}\rangle) \\
&\quad +(n_{\mathbf{i},\beta,\uparrow} + n_{\mathbf{i},\beta,\downarrow})(\langle n_{\mathbf{i},\alpha,\uparrow}\rangle + \langle n_{\mathbf{i},\alpha,\downarrow}\rangle) - (\langle n_{\mathbf{i},\alpha,\uparrow}\rangle + \langle n_{\mathbf{i},\alpha,\downarrow}\rangle)(\langle n_{\mathbf{i},\beta,\uparrow}\rangle + \langle n_{\mathbf{i},\beta,\downarrow}\rangle)] \\
&\quad -(U' - \frac{J}{2})\sum_{\mathbf{i},\alpha<\beta} \\
&\quad [(\langle c^{\dagger}_{\mathbf{i},\alpha,\uparrow}c_{\mathbf{i},\beta,\uparrow}\rangle c^{\dagger}_{\mathbf{i},\beta,\uparrow}c_{\mathbf{i},\alpha,\uparrow} + \langle c^{\dagger}_{\mathbf{i},\beta,\uparrow}c_{\mathbf{i},\alpha,\uparrow}\rangle c^{\dagger}_{\mathbf{i},\alpha,\uparrow}c_{\mathbf{i},\beta,\uparrow} - \langle c^{\dagger}_{\mathbf{i},\alpha,\uparrow}c_{\mathbf{i},\beta,\uparrow}\rangle\langle c^{\dagger}_{\mathbf{i},\beta,\uparrow}c_{\mathbf{i},\alpha,\uparrow}\rangle) \\
&\quad +(\langle c^{\dagger}_{\mathbf{i},\alpha,\uparrow}c_{\mathbf{i},\beta,\downarrow}\rangle c^{\dagger}_{\mathbf{i},\beta,\downarrow}c_{\mathbf{i},\alpha,\uparrow} + \langle c^{\dagger}_{\mathbf{i},\beta,\downarrow}c_{\mathbf{i},\alpha,\uparrow}\rangle c^{\dagger}_{\mathbf{i},\alpha,\uparrow}c_{\mathbf{i},\beta,\downarrow} - \langle c^{\dagger}_{\mathbf{i},\alpha,\uparrow}c_{\mathbf{i},\beta,\downarrow}\rangle\langle c^{\dagger}_{\mathbf{i},\beta,\downarrow}c_{\mathbf{i},\alpha,\uparrow}\rangle) \\
&\quad +(\langle c^{\dagger}_{\mathbf{i},\alpha,\downarrow}c_{\mathbf{i},\beta,\uparrow}\rangle c^{\dagger}_{\mathbf{i},\beta,\uparrow}c_{\mathbf{i},\alpha,\downarrow} + \langle c^{\dagger}_{\mathbf{i},\beta,\uparrow}c_{\mathbf{i},\alpha,\downarrow}\rangle c^{\dagger}_{\mathbf{i},\alpha,\downarrow}c_{\mathbf{i},\beta,\uparrow} - \langle c^{\dagger}_{\mathbf{i},\alpha,\downarrow}c_{\mathbf{i},\beta,\uparrow}\rangle\langle c^{\dagger}_{\mathbf{i},\beta,\uparrow}c_{\mathbf{i},\alpha,\downarrow}\rangle) \\
&\quad +(\langle c^{\dagger}_{\mathbf{i},\alpha,\downarrow}c_{\mathbf{i},\beta,\downarrow}\rangle c^{\dagger}_{\mathbf{i},\beta,\downarrow}c_{\mathbf{i},\alpha,\downarrow} + \langle c^{\dagger}_{\mathbf{i},\beta,\downarrow}c_{\mathbf{i},\alpha,\downarrow}\rangle c^{\dagger}_{\mathbf{i},\alpha,\downarrow}c_{\mathbf{i},\beta,\downarrow} - \langle c^{\dagger}_{\mathbf{i},\alpha,\downarrow}c_{\mathbf{i},\beta,\downarrow}\rangle\langle c^{\dagger}_{\mathbf{i},\beta,\downarrow}c_{\mathbf{i},\alpha,\downarrow}\rangle)].
\end{aligned} \tag{2.7}
$$

The Hartree-Fock approximation of H_3 can be written as:

$$
\begin{aligned}
H_3 &= -2J \sum_{\mathbf{i},\alpha<\beta} \mathbf{S}_{\mathbf{i},\alpha} \cdot \mathbf{S}_{\mathbf{i},\beta} \qquad (2.8)\\
&= -\frac{J}{2} \sum_{\mathbf{i},\alpha<\beta} [(c^\dagger_{\mathbf{i},\alpha,\uparrow} c_{\mathbf{i},\alpha,\downarrow} + c^\dagger_{\mathbf{i},\alpha,\downarrow} c_{\mathbf{i},\alpha,\uparrow})(c^\dagger_{\mathbf{i},\beta,\uparrow} c_{\mathbf{i},\beta,\downarrow} + c^\dagger_{\mathbf{i},\beta,\downarrow} c_{\mathbf{i},\beta,\uparrow})\\
&\quad +(-i\, c^\dagger_{\mathbf{i},\alpha,\uparrow} c_{\mathbf{i},\alpha,\downarrow} + i\, c^\dagger_{\mathbf{i},\alpha,\downarrow} c_{\mathbf{i},\alpha,\uparrow})(-i\, c^\dagger_{\mathbf{i},\beta,\uparrow} c_{\mathbf{i},\beta,\downarrow} + i\, c^\dagger_{\mathbf{i},\beta,\downarrow} c_{\mathbf{i},\beta,\uparrow})\\
&\quad +(c^\dagger_{\mathbf{i},\alpha,\uparrow} c_{\mathbf{i},\alpha,\uparrow} - c^\dagger_{\mathbf{i},\alpha,\downarrow} c_{\mathbf{i},\alpha,\downarrow})(c^\dagger_{\mathbf{i},\beta,\uparrow} c_{\mathbf{i},\beta,\uparrow} - c^\dagger_{\mathbf{i},\beta,\downarrow} c_{\mathbf{i},\beta,\downarrow})]\\
&= -\frac{J}{2} \sum_{\mathbf{i},\alpha<\beta} [2(c^\dagger_{\mathbf{i},\alpha,\uparrow} c_{\mathbf{i},\alpha,\downarrow} c^\dagger_{\mathbf{i},\beta,\downarrow} c_{\mathbf{i},\beta,\uparrow} + c^\dagger_{\mathbf{i},\alpha,\downarrow} c_{\mathbf{i},\alpha,\uparrow} c^\dagger_{\mathbf{i},\beta,\uparrow} c_{\mathbf{i},\beta,\downarrow})\\
&\quad +c^\dagger_{\mathbf{i},\alpha,\uparrow} c_{\mathbf{i},\alpha,\uparrow} c^\dagger_{\mathbf{i},\beta,\uparrow} c_{\mathbf{i},\beta,\uparrow} - c^\dagger_{\mathbf{i},\alpha,\downarrow} c_{\mathbf{i},\alpha,\downarrow} c^\dagger_{\mathbf{i},\beta,\uparrow} c_{\mathbf{i},\beta,\uparrow}\\
&\quad -c^\dagger_{\mathbf{i},\alpha,\uparrow} c_{\mathbf{i},\alpha,\uparrow} c^\dagger_{\mathbf{i},\beta,\downarrow} c_{\mathbf{i},\beta,\downarrow} + c^\dagger_{\mathbf{i},\alpha,\downarrow} c_{\mathbf{i},\alpha,\downarrow} c^\dagger_{\mathbf{i},\beta,\downarrow} c_{\mathbf{i},\beta,\downarrow}]\\
&\approx -\frac{J}{2} \sum_{\mathbf{i},\alpha<\beta} [2(\langle c^\dagger_{\mathbf{i},\alpha,\uparrow} c_{\mathbf{i},\alpha,\downarrow}\rangle c^\dagger_{\mathbf{i},\beta,\downarrow} c_{\mathbf{i},\beta,\uparrow} + \langle c^\dagger_{\mathbf{i},\beta,\downarrow} c_{\mathbf{i},\beta,\uparrow}\rangle c^\dagger_{\mathbf{i},\alpha,\uparrow} c_{\mathbf{i},\alpha,\downarrow} - \langle c^\dagger_{\mathbf{i},\alpha,\uparrow} c_{\mathbf{i},\alpha,\downarrow}\rangle \langle c^\dagger_{\mathbf{i},\beta,\downarrow} c_{\mathbf{i},\beta,\uparrow}\rangle)\\
&\quad +2(\langle c^\dagger_{\mathbf{i},\alpha,\downarrow} c_{\mathbf{i},\alpha,\uparrow}\rangle c^\dagger_{\mathbf{i},\beta,\uparrow} c_{\mathbf{i},\beta,\downarrow} + \langle c^\dagger_{\mathbf{i},\beta,\uparrow} c_{\mathbf{i},\beta,\downarrow}\rangle c^\dagger_{\mathbf{i},\alpha,\downarrow} c_{\mathbf{i},\alpha,\uparrow} - \langle c^\dagger_{\mathbf{i},\alpha,\downarrow} c_{\mathbf{i},\alpha,\uparrow}\rangle \langle c^\dagger_{\mathbf{i},\beta,\uparrow} c_{\mathbf{i},\beta,\downarrow}\rangle)\\
&\quad +(\langle c^\dagger_{\mathbf{i},\alpha,\uparrow} c_{\mathbf{i},\alpha,\uparrow}\rangle c^\dagger_{\mathbf{i},\beta,\uparrow} c_{\mathbf{i},\beta,\uparrow} + \langle c^\dagger_{\mathbf{i},\beta,\uparrow} c_{\mathbf{i},\beta,\uparrow}\rangle c^\dagger_{\mathbf{i},\alpha,\uparrow} c_{\mathbf{i},\alpha,\uparrow} - \langle c^\dagger_{\mathbf{i},\alpha,\uparrow} c_{\mathbf{i},\alpha,\uparrow}\rangle \langle c^\dagger_{\mathbf{i},\beta,\uparrow} c_{\mathbf{i},\beta,\uparrow}\rangle)\\
&\quad -(\langle c^\dagger_{\mathbf{i},\alpha,\downarrow} c_{\mathbf{i},\alpha,\downarrow}\rangle c^\dagger_{\mathbf{i},\beta,\uparrow} c_{\mathbf{i},\beta,\uparrow} + \langle c^\dagger_{\mathbf{i},\beta,\uparrow} c_{\mathbf{i},\beta,\uparrow}\rangle c^\dagger_{\mathbf{i},\alpha,\downarrow} c_{\mathbf{i},\alpha,\downarrow} - \langle c^\dagger_{\mathbf{i},\alpha,\downarrow} c_{\mathbf{i},\alpha,\downarrow}\rangle \langle c^\dagger_{\mathbf{i},\beta,\uparrow} c_{\mathbf{i},\beta,\uparrow}\rangle)\\
&\quad -(\langle c^\dagger_{\mathbf{i},\alpha,\uparrow} c_{\mathbf{i},\alpha,\uparrow}\rangle c^\dagger_{\mathbf{i},\beta,\downarrow} c_{\mathbf{i},\beta,\downarrow} + \langle c^\dagger_{\mathbf{i},\beta,\downarrow} c_{\mathbf{i},\beta,\downarrow}\rangle c^\dagger_{\mathbf{i},\alpha,\uparrow} c_{\mathbf{i},\alpha,\uparrow} - \langle c^\dagger_{\mathbf{i},\alpha,\uparrow} c_{\mathbf{i},\alpha,\uparrow}\rangle \langle c^\dagger_{\mathbf{i},\beta,\downarrow} c_{\mathbf{i},\beta,\downarrow}\rangle)\\
&\quad +(\langle c^\dagger_{\mathbf{i},\alpha,\downarrow} c_{\mathbf{i},\alpha,\downarrow}\rangle c^\dagger_{\mathbf{i},\beta,\downarrow} c_{\mathbf{i},\beta,\downarrow} + \langle c^\dagger_{\mathbf{i},\beta,\downarrow} c_{\mathbf{i},\beta,\downarrow}\rangle c^\dagger_{\mathbf{i},\alpha,\downarrow} c_{\mathbf{i},\alpha,\downarrow} - \langle c^\dagger_{\mathbf{i},\alpha,\downarrow} c_{\mathbf{i},\alpha,\downarrow}\rangle \langle c^\dagger_{\mathbf{i},\beta,\downarrow} c_{\mathbf{i},\beta,\downarrow}\rangle)]\\
&\quad +\frac{J}{2} \sum_{\mathbf{i},\alpha<\beta} [2(\langle c^\dagger_{\mathbf{i},\alpha,\uparrow} c_{\mathbf{i},\beta,\uparrow}\rangle c^\dagger_{\mathbf{i},\beta,\downarrow} c_{\mathbf{i},\alpha,\downarrow} + \langle c^\dagger_{\mathbf{i},\beta,\downarrow} c_{\mathbf{i},\alpha,\downarrow}\rangle c^\dagger_{\mathbf{i},\alpha,\uparrow} c_{\mathbf{i},\beta,\uparrow} - \langle c^\dagger_{\mathbf{i},\alpha,\uparrow} c_{\mathbf{i},\beta,\uparrow}\rangle \langle c^\dagger_{\mathbf{i},\beta,\downarrow} c_{\mathbf{i},\alpha,\downarrow}\rangle)\\
&\quad +2(\langle c^\dagger_{\mathbf{i},\alpha,\downarrow} c_{\mathbf{i},\beta,\downarrow}\rangle c^\dagger_{\mathbf{i},\beta,\uparrow} c_{\mathbf{i},\alpha,\uparrow} + \langle c^\dagger_{\mathbf{i},\beta,\uparrow} c_{\mathbf{i},\alpha,\uparrow}\rangle c^\dagger_{\mathbf{i},\alpha,\downarrow} c_{\mathbf{i},\beta,\downarrow} - \langle c^\dagger_{\mathbf{i},\alpha,\downarrow} c_{\mathbf{i},\beta,\downarrow}\rangle \langle c^\dagger_{\mathbf{i},\beta,\uparrow} c_{\mathbf{i},\alpha,\uparrow}\rangle)\\
&\quad +(\langle c^\dagger_{\mathbf{i},\alpha,\uparrow} c_{\mathbf{i},\beta,\uparrow}\rangle c^\dagger_{\mathbf{i},\beta,\uparrow} c_{\mathbf{i},\alpha,\uparrow} + \langle c^\dagger_{\mathbf{i},\beta,\uparrow} c_{\mathbf{i},\alpha,\uparrow}\rangle c^\dagger_{\mathbf{i},\alpha,\uparrow} c_{\mathbf{i},\beta,\uparrow} - \langle c^\dagger_{\mathbf{i},\alpha,\uparrow} c_{\mathbf{i},\beta,\uparrow}\rangle \langle c^\dagger_{\mathbf{i},\beta,\uparrow} c_{\mathbf{i},\alpha,\uparrow}\rangle)\\
&\quad -(\langle c^\dagger_{\mathbf{i},\alpha,\downarrow} c_{\mathbf{i},\beta,\uparrow}\rangle c^\dagger_{\mathbf{i},\beta,\uparrow} c_{\mathbf{i},\alpha,\downarrow} + \langle c^\dagger_{\mathbf{i},\beta,\uparrow} c_{\mathbf{i},\alpha,\downarrow}\rangle c^\dagger_{\mathbf{i},\alpha,\downarrow} c_{\mathbf{i},\beta,\uparrow} - \langle c^\dagger_{\mathbf{i},\alpha,\downarrow} c_{\mathbf{i},\beta,\uparrow}\rangle \langle c^\dagger_{\mathbf{i},\beta,\uparrow} c_{\mathbf{i},\alpha,\downarrow}\rangle)\\
&\quad -(\langle c^\dagger_{\mathbf{i},\alpha,\uparrow} c_{\mathbf{i},\beta,\downarrow}\rangle c^\dagger_{\mathbf{i},\beta,\downarrow} c_{\mathbf{i},\alpha,\uparrow} + \langle c^\dagger_{\mathbf{i},\beta,\downarrow} c_{\mathbf{i},\alpha,\uparrow}\rangle c^\dagger_{\mathbf{i},\alpha,\uparrow} c_{\mathbf{i},\beta,\downarrow} - \langle c^\dagger_{\mathbf{i},\alpha,\uparrow} c_{\mathbf{i},\beta,\downarrow}\rangle \langle c^\dagger_{\mathbf{i},\beta,\downarrow} c_{\mathbf{i},\alpha,\uparrow}\rangle)\\
&\quad +(\langle c^\dagger_{\mathbf{i},\alpha,\downarrow} c_{\mathbf{i},\beta,\downarrow}\rangle c^\dagger_{\mathbf{i},\beta,\downarrow} c_{\mathbf{i},\alpha,\downarrow} + \langle c^\dagger_{\mathbf{i},\beta,\downarrow} c_{\mathbf{i},\alpha,\downarrow}\rangle c^\dagger_{\mathbf{i},\alpha,\downarrow} c_{\mathbf{i},\beta,\downarrow} - \langle c^\dagger_{\mathbf{i},\alpha,\downarrow} c_{\mathbf{i},\beta,\downarrow}\rangle \langle c^\dagger_{\mathbf{i},\beta,\downarrow} c_{\mathbf{i},\alpha,\downarrow}\rangle).
\end{aligned}
$$

While the forth term H_4 can be written as:

$$
\begin{aligned}
H_4 &= J\sum_{\mathbf{i},\alpha<\beta}(c^{\dagger}_{\mathbf{i},\alpha,\uparrow}c^{\dagger}_{\mathbf{i},\alpha,\downarrow}c_{\mathbf{i},\beta,\downarrow}c_{\mathbf{i},\beta,\uparrow}+h.c.), \qquad (2.9)\\
&\approx J\sum_{\mathbf{i},\alpha<\beta}[-(\langle c^{\dagger}_{\mathbf{i},\alpha,\uparrow}c_{\mathbf{i},\beta,\downarrow}\rangle c^{\dagger}_{\mathbf{i},\alpha,\downarrow}c_{\mathbf{i},\beta,\uparrow}+\langle c^{\dagger}_{\mathbf{i},\alpha,\downarrow}c_{\mathbf{i},\beta,\uparrow}\rangle c^{\dagger}_{\mathbf{i},\alpha,\uparrow}c_{\mathbf{i},\beta,\downarrow}-\langle c^{\dagger}_{\mathbf{i},\alpha,\uparrow}c_{\mathbf{i},\beta,\downarrow}\rangle\langle c^{\dagger}_{\mathbf{i},\alpha,\downarrow}c_{\mathbf{i},\beta,\uparrow}\rangle)\\
&\quad -(\langle c^{\dagger}_{\mathbf{i},\beta,\uparrow}c_{\mathbf{i},\alpha,\downarrow}\rangle c^{\dagger}_{\mathbf{i},\beta,\downarrow}c_{\mathbf{i},\alpha,\uparrow}+\langle c^{\dagger}_{\mathbf{i},\beta,\downarrow}c_{\mathbf{i},\alpha,\uparrow}\rangle c^{\dagger}_{\mathbf{i},\beta,\uparrow}c_{\mathbf{i},\alpha,\downarrow}-\langle c^{\dagger}_{\mathbf{i},\beta,\uparrow}c_{\mathbf{i},\alpha,\downarrow}\rangle\langle c^{\dagger}_{\mathbf{i},\beta,\downarrow}c_{\mathbf{i},\alpha,\uparrow}\rangle)]\\
&\quad +J\sum_{\mathbf{i},\alpha<\beta}[(\langle c^{\dagger}_{\mathbf{i},\alpha,\uparrow}c_{\mathbf{i},\beta,\uparrow}\rangle c^{\dagger}_{\mathbf{i},\alpha,\downarrow}c_{\mathbf{i},\beta,\downarrow}+\langle c^{\dagger}_{\mathbf{i},\alpha,\downarrow}c_{\mathbf{i},\beta,\downarrow}\rangle c^{\dagger}_{\mathbf{i},\alpha,\uparrow}c_{\mathbf{i},\beta,\uparrow}-\langle c^{\dagger}_{\mathbf{i},\alpha,\uparrow}c_{\mathbf{i},\beta,\uparrow}\rangle\langle c^{\dagger}_{\mathbf{i},\alpha,\downarrow}c_{\mathbf{i},\beta,\downarrow}\rangle)\\
&\quad +(\langle c^{\dagger}_{\mathbf{i},\beta,\downarrow}c_{\mathbf{i},\alpha,\downarrow}\rangle c^{\dagger}_{\mathbf{i},\beta,\uparrow}c_{\mathbf{i},\alpha,\uparrow}+\langle c^{\dagger}_{\mathbf{i},\beta,\uparrow}c_{\mathbf{i},\alpha,\uparrow}\rangle c^{\dagger}_{\mathbf{i},\beta,\downarrow}c_{\mathbf{i},\alpha,\downarrow}-\langle c^{\dagger}_{\mathbf{i},\beta,\downarrow}c_{\mathbf{i},\alpha,\downarrow}\rangle\langle c^{\dagger}_{\mathbf{i},\beta,\uparrow}c_{\mathbf{i},\alpha,\uparrow}\rangle)].
\end{aligned}
$$

In this HF Hamiltonian, the various expectation values (such as $\langle c^{\dagger}_{\mathbf{i},\alpha,\uparrow}c_{\mathbf{i},\alpha,\downarrow}\rangle$) are considered as HF parameters and can be determined self-consistently by minimizing the HF energy with respect to the various expectation values numerically. The details of how to minimize the HF energy self-consistently will be discussed in the last subsection of this chapter.

2.2.2 Hartree-Fock Approximation in Momentum Space

In order to apply the HF Hamiltonian in momentum space, a reasonable Ansatz [Nomura and Yamada (2000)] is needed, proposed as :

$$
\langle c^{\dagger}_{\mathbf{i},\alpha,\sigma}c_{\mathbf{i}',\alpha',\sigma'}\rangle = (n_\alpha+\frac{\sigma}{2}m_\alpha e^{i\,\mathbf{Q}\cdot\mathbf{i}})\delta_{\mathbf{i}\mathbf{i}'}\delta_{\alpha\alpha'}\delta_{\sigma\sigma'}, \qquad (2.10)
$$

where $\mathbf{Q}=(\pi,0)$ represents the ordering wave vector of the magnetic order for the parent compounds. n_α and m_α are mean-field parameters (to be determined self-consistently) describing the charge density and magnetization of the orbital α, respectively. Only $\langle n_{\mathbf{i},\alpha,\sigma}\rangle$ survives as:

$$\langle n_{\mathbf{i},\alpha,\uparrow}\rangle = (n_\alpha + \frac{1}{2}m_\alpha e^{i\,\mathbf{Q}\cdot\mathbf{i}}), \tag{2.11}$$

$$\langle n_{\mathbf{i},\alpha,\downarrow}\rangle = (n_\alpha - \frac{1}{2}m_\alpha e^{i\,\mathbf{Q}\cdot\mathbf{i}}). \tag{2.12}$$

It is reasonable to assume that all the other mean values are zero, such as $\langle c^\dagger_{\mathbf{i},\alpha,\uparrow}c_{\mathbf{i},\alpha,\downarrow}\rangle = \langle c^\dagger_{\mathbf{i},\alpha,\downarrow}c_{\mathbf{i},\alpha,\uparrow}\rangle = 0$, because the possibility of one particle hopping between different orbitals or with different spins is very tiny compared to that between the same orbital with the same spin. Based on the Ansatz proposed in Eq.(2.10), H_1, H_2, H_3 and H_4 can be rewritten as:

$$\begin{aligned} H_1 &= U\sum_{\mathbf{i},\alpha}[n_{\mathbf{i},\alpha,\uparrow}(n_\alpha - \frac{1}{2}m_\alpha e^{i\,\mathbf{Q}\cdot\mathbf{i}}) + n_{\mathbf{i},\alpha,\downarrow}(n_\alpha + \frac{1}{2}m_\alpha e^{i\,\mathbf{Q}\cdot\mathbf{i}}) \\ &\quad -(n_\alpha + \frac{1}{2}m_\alpha e^{i\,\mathbf{Q}\cdot\mathbf{i}})(n_\alpha - \frac{1}{2}m_\alpha e^{i\,\mathbf{Q}\cdot\mathbf{i}})] \qquad (2.13) \\ &= -UN\sum_\alpha(n_\alpha^2 - \frac{1}{4}m_\alpha^2) + U\sum_{\mathbf{i},\alpha}[n_\alpha(n_{\mathbf{i},\alpha,\uparrow} + n_{\mathbf{i},\alpha,\downarrow}) + \frac{1}{2}m_\alpha e^{i\,\mathbf{Q}\cdot\mathbf{i}}(n_{\mathbf{i},\alpha,\downarrow} - n_{\mathbf{i},\alpha,\uparrow})], \end{aligned}$$

$$\begin{aligned} H_2 &= (U' - \frac{J}{2})\sum_{\mathbf{i},\alpha<\beta}[(n_{\mathbf{i},\alpha,\uparrow} + n_{\mathbf{i},\alpha,\downarrow})(n_\beta + \frac{1}{2}m_\beta e^{i\,\mathbf{Q}\cdot\mathbf{i}} + n_\beta - \frac{1}{2}m_\beta e^{i\,\mathbf{Q}\cdot\mathbf{i}}) \qquad (2.14) \\ &\quad +(n_{\mathbf{i},\beta,\uparrow} + n_{\mathbf{i},\beta,\downarrow})(n_\alpha + \frac{1}{2}m_\alpha e^{i\,\mathbf{Q}\cdot\mathbf{i}} + n_\alpha - \frac{1}{2}m_\alpha e^{i\,\mathbf{Q}\cdot\mathbf{i}}) \\ &\quad -(n_\alpha + \frac{1}{2}m_\alpha e^{i\,\mathbf{Q}\cdot\mathbf{i}} + n_\alpha - \frac{1}{2}m_\alpha e^{i\,\mathbf{Q}\cdot\mathbf{i}})(n_\beta + \frac{1}{2}m_\beta e^{i\,\mathbf{Q}\cdot\mathbf{i}} + n_\beta - \frac{1}{2}m_\beta e^{i\,\mathbf{Q}\cdot\mathbf{i}})] \\ &= -4N(U' - \frac{J}{2})\sum_{\alpha<\beta}n_\alpha n_\beta + 2(U' - \frac{J}{2})\sum_{\mathbf{i},\alpha}[\sum_{\beta\neq\alpha}n_\beta(n_{\mathbf{i},\alpha,\uparrow} + n_{\mathbf{i},\alpha,\downarrow})] \\ &= -2N(U' - \frac{J}{2})\sum_{\alpha\neq\beta}n_\alpha n_\beta + 2(U' - \frac{J}{2})\sum_{\mathbf{i},\alpha\neq\beta}[n_\beta(n_{\mathbf{i},\alpha,\uparrow} + n_{\mathbf{i},\alpha,\downarrow})]. \end{aligned}$$

$$
\begin{aligned}
H_3 &= -\frac{J}{2}\sum_{\mathbf{i},\alpha<\beta}[n_{\mathbf{i},\beta,\uparrow}(n_\alpha+\frac{1}{2}m_\alpha e^{i\,\mathbf{Q}\cdot\mathbf{i}})+n_{\mathbf{i},\alpha,\uparrow}(n_\beta+\frac{1}{2}m_\beta e^{i\,\mathbf{Q}\cdot\mathbf{i}}) \\
&\quad -(n_\alpha+\frac{1}{2}m_\alpha e^{i\,\mathbf{Q}\cdot\mathbf{i}})(n_\beta+\frac{1}{2}m_\beta e^{i\,\mathbf{Q}\cdot\mathbf{i}})-n_{\mathbf{i},\beta,\uparrow}(n_\alpha-\frac{1}{2}m_\alpha e^{i\,\mathbf{Q}\cdot\mathbf{i}}) \\
&\quad -n_{\mathbf{i},\alpha,\downarrow}(n_\beta+\frac{1}{2}m_\beta e^{i\,\mathbf{Q}\cdot\mathbf{i}})+(n_\alpha-\frac{1}{2}m_\alpha e^{i\,\mathbf{Q}\cdot\mathbf{i}})(n_\beta+\frac{1}{2}m_\beta e^{i\,\mathbf{Q}\cdot\mathbf{i}}) \\
&\quad -n_{\mathbf{i},\beta,\downarrow}(n_\alpha+\frac{1}{2}m_\alpha e^{i\,\mathbf{Q}\cdot\mathbf{i}})-n_{\mathbf{i},\alpha,\uparrow}(n_\beta-\frac{1}{2}m_\beta e^{i\,\mathbf{Q}\cdot\mathbf{i}}) \\
&\quad +(n_\alpha+\frac{1}{2}m_\alpha e^{i\,\mathbf{Q}\cdot\mathbf{i}})(n_\beta-\frac{1}{2}m_\beta e^{i\,\mathbf{Q}\cdot\mathbf{i}})+n_{\mathbf{i},\beta,\downarrow}(n_\alpha-\frac{1}{2}m_\alpha e^{i\,\mathbf{Q}\cdot\mathbf{i}}) \\
&\quad +n_{\mathbf{i},\alpha,\downarrow}(n_\beta-\frac{1}{2}m_\beta e^{i\,\mathbf{Q}\cdot\mathbf{i}})-(n_\alpha-\frac{1}{2}m_\alpha e^{i\,\mathbf{Q}\cdot\mathbf{i}})(n_\beta-\frac{1}{2}m_\beta e^{i\,\mathbf{Q}\cdot\mathbf{i}})] \\
&= -\frac{J}{2}\sum_{\mathbf{i},\alpha<\beta}[-m_\alpha m_\beta+m_\alpha e^{i\,\mathbf{Q}\cdot\mathbf{i}}(n_{\mathbf{i},\beta,\uparrow}-n_{\mathbf{i},\beta,\downarrow})+m_\beta e^{i\,\mathbf{Q}\cdot\mathbf{i}}(n_{\mathbf{i},\alpha,\uparrow}-n_{\mathbf{i},\alpha,\downarrow})] \\
&= \frac{JN}{2}\sum_{\alpha<\beta}m_\alpha m_\beta-\frac{J}{2}\sum_{\mathbf{i},\alpha\neq\beta}m_\alpha e^{i\,\mathbf{Q}\cdot\mathbf{i}}(n_{\mathbf{i},\beta,\uparrow}-n_{\mathbf{i},\beta,\downarrow}).
\end{aligned}
\tag{2.15}
$$

$$
H_4 = 0.
$$

The last term H_4 becomes zero after applying the Ansatz proposed in Eq.(2.10).

In summary, the Coulombic interaction has a compact form as:

$$
\begin{aligned}
H_{\text{int}} &= -UN\sum_\alpha(n_\alpha^2-\frac{1}{4}m_\alpha^2)+U\sum_{\mathbf{i},\alpha}[n_\alpha(n_{\mathbf{i},\alpha,\uparrow}+n_{\mathbf{i},\alpha,\downarrow})+\frac{1}{2}m_\alpha e^{i\,\mathbf{Q}\cdot\mathbf{i}}(n_{\mathbf{i},\alpha,\downarrow}-n_{\mathbf{i},\alpha,\uparrow})] \\
&\quad -2N(U'-\frac{J}{2})\sum_{\alpha\neq\beta}n_\alpha n_\beta+2(U'-\frac{J}{2})\sum_{\mathbf{i},\alpha\neq\beta}[n_\beta(n_{\mathbf{i},\alpha,\uparrow}+n_{\mathbf{i},\alpha,\downarrow})] \\
&\quad +\frac{JN}{2}\sum_{\alpha<\beta}m_\alpha m_\beta-\frac{J}{2}\sum_{\mathbf{i},\alpha\neq\beta}m_\alpha e^{i\,\mathbf{Q}\cdot\mathbf{i}}(n_{\mathbf{i},\beta,\uparrow}-n_{\mathbf{i},\beta,\downarrow})
\end{aligned}
\tag{2.16}
$$

In order to get the Hamiltonian in momentum space, the discrete Fourier transformation is introduced here:

$$
c_{\mathbf{i},\alpha,\sigma}=\frac{1}{\sqrt{N}}\sum_{\mathbf{k}}e^{i\,\mathbf{k}\cdot\mathbf{i}}c_{\mathbf{k},\alpha,\sigma}. \tag{2.17}
$$

Therefore, the tight-binding Hamiltonian can be transformed into momentum space as:

$$H_{\mathrm{TB}} = \sum_{\mathbf{k},\sigma} \sum_{\alpha,\beta} \left(\xi_{\alpha\beta}(\mathbf{k}) + \epsilon_\alpha \delta_{\alpha\beta}\right) c^\dagger_{\mathbf{k},\alpha,\sigma} c_{\mathbf{k},\beta,\sigma}, \tag{2.18}$$

where $\xi_{\alpha\beta}(\mathbf{k})$ represents the hopping amplitude and ϵ_α represents the on-site energy.

The interation Hamiltonian in momentum space can be obtained by applying this Fourier transformation as:

$$\begin{aligned}
H_1 &= -UN\sum_\alpha (n_\alpha^2 - \frac{1}{4}m_\alpha^2) + U\sum_{\mathbf{i},\alpha}[n_\alpha(n_{\mathbf{i},\alpha,\uparrow} + n_{\mathbf{i},\alpha,\downarrow}) + \frac{1}{2}m_\alpha e^{i\,\mathbf{Q}\cdot\mathbf{i}}(n_{\mathbf{i},\alpha,\downarrow} - n_{\mathbf{i},\alpha,\uparrow})] \\
&= -UN\sum_\alpha (n_\alpha^2 - \frac{1}{4}m_\alpha^2) \\
&\quad + \frac{U}{N}\sum_{\mathbf{i},\alpha}[n_\alpha(\sum_{\mathbf{k}} e^{-i\,\mathbf{k}\cdot\mathbf{i}} c^\dagger_{\mathbf{k},\alpha,\uparrow} \sum_{\mathbf{k}'} e^{i\,\mathbf{k}'\cdot\mathbf{i}} c_{\mathbf{k}',\alpha,\uparrow} + \sum_{\mathbf{k}} e^{-i\,\mathbf{k}\cdot\mathbf{i}} c^\dagger_{\mathbf{k},\alpha,\downarrow} \sum_{\mathbf{k}'} e^{i\,\mathbf{k}'\cdot\mathbf{i}} c_{\mathbf{k}',\alpha,\downarrow}) \\
&\quad + \frac{1}{2}m_\alpha e^{i\,\mathbf{Q}\cdot\mathbf{i}}(\sum_{\mathbf{k}} e^{-i\,\mathbf{k}\cdot\mathbf{i}} c^\dagger_{\mathbf{k},\alpha,\downarrow} \sum_{\mathbf{k}'} e^{i\,\mathbf{k}'\cdot\mathbf{i}} c_{\mathbf{k}',\alpha,\downarrow} - \sum_{\mathbf{k}} e^{-i\,\mathbf{k}\cdot\mathbf{i}} c^\dagger_{\mathbf{k},\alpha,\uparrow} \sum_{\mathbf{k}'} e^{i\,\mathbf{k}'\cdot\mathbf{i}} c_{\mathbf{k}',\alpha,\uparrow})] \\
&= -UN\sum_\alpha (n_\alpha^2 - \frac{1}{4}m_\alpha^2) \\
&\quad + \frac{U}{N}\sum_{\mathbf{i},\alpha}[n_\alpha(\sum_{\mathbf{k},\mathbf{k}'} e^{-i\,(\mathbf{k}-\mathbf{k}')\cdot\mathbf{i}} c^\dagger_{\mathbf{k},\alpha,\uparrow} c_{\mathbf{k}',\alpha,\uparrow} + \sum_{\mathbf{k},\mathbf{k}'} e^{-i\,(\mathbf{k}-\mathbf{k}')\cdot\mathbf{i}} c^\dagger_{\mathbf{k},\alpha,\downarrow} c_{\mathbf{k}',\alpha,\downarrow}) \\
&\quad + \frac{1}{2}m_\alpha(\sum_{\mathbf{k},\mathbf{k}'} e^{-i\,(\mathbf{k}-\mathbf{k}'-\mathbf{Q})\cdot\mathbf{i}} c^\dagger_{\mathbf{k},\alpha,\downarrow} c_{\mathbf{k}',\alpha,\downarrow} - \sum_{\mathbf{k},\mathbf{k}'} e^{-i\,(\mathbf{k}-\mathbf{k}'-\mathbf{Q})\cdot\mathbf{i}} c^\dagger_{\mathbf{k},\alpha,\uparrow} c_{\mathbf{k}',\alpha,\uparrow})] \\
&= -UN\sum_\alpha (n_\alpha^2 - \frac{1}{4}m_\alpha^2) + U\sum_\alpha\sum_{\mathbf{k},\mathbf{k}'}[n_\alpha(\delta_{\mathbf{k},\mathbf{k}'} c^\dagger_{\mathbf{k},\alpha,\uparrow} c_{\mathbf{k}',\alpha,\uparrow} + \delta_{\mathbf{k},\mathbf{k}'} c^\dagger_{\mathbf{k},\alpha,\downarrow} c_{\mathbf{k}',\alpha,\downarrow}) \\
&\quad + \frac{1}{2}m_\alpha(\delta_{\mathbf{k},\mathbf{k}'-\mathbf{Q}} c^\dagger_{\mathbf{k},\alpha,\downarrow} c_{\mathbf{k}',\alpha,\downarrow} - \delta_{\mathbf{k},\mathbf{k}'-\mathbf{Q}} c^\dagger_{\mathbf{k},\alpha,\uparrow} c_{\mathbf{k}',\alpha,\uparrow})] \\
&= -UN\sum_\alpha (n_\alpha^2 - \frac{1}{4}m_\alpha^2) + U\sum_{\mathbf{k},\alpha} n_\alpha(c^\dagger_{\mathbf{k},\alpha,\uparrow} c_{\mathbf{k},\alpha,\uparrow} + c^\dagger_{\mathbf{k},\alpha,\downarrow} c_{\mathbf{k},\alpha,\downarrow}) \\
&\quad - U\sum_{\mathbf{k},\alpha}\frac{1}{2}m_\alpha(c^\dagger_{\mathbf{k}+\mathbf{Q},\alpha,\uparrow} c_{\mathbf{k},\alpha,\uparrow} - c^\dagger_{\mathbf{k}+\mathbf{Q},\alpha,\downarrow} c_{\mathbf{k},\alpha,\downarrow}),
\end{aligned} \tag{2.19}$$

$$
\begin{aligned}
H_2 &= -2N(U'-\frac{J}{2})\sum_{\alpha\neq\beta} n_\alpha n_\beta + 2(U'-\frac{J}{2})\sum_{\mathbf{i},\alpha\neq\beta}[n_\beta(n_{\mathbf{i},\alpha,\uparrow}+n_{\mathbf{i},\alpha,\downarrow})] \qquad (2.20)\\
&= -2N(U'-\frac{J}{2})\sum_{\alpha\neq\beta} n_\alpha n_\beta + \frac{2}{N}(U'-\frac{J}{2})\sum_{\mathbf{i},\alpha\neq\beta}[n_\beta(\sum_{\mathbf{k}} e^{-i\,\mathbf{k}\cdot\mathbf{i}} c^\dagger_{\mathbf{k},\alpha,\uparrow}\sum_{\mathbf{k}'} e^{i\,\mathbf{k}'\cdot\mathbf{i}} c_{\mathbf{k}',\alpha,\uparrow}\\
&\quad + \sum_{\mathbf{k}} e^{-i\,\mathbf{k}\cdot\mathbf{i}} c^\dagger_{\mathbf{k},\alpha,\downarrow}\sum_{\mathbf{k}'} e^{i\,\mathbf{k}'\cdot\mathbf{i}} c_{\mathbf{k}',\alpha,\downarrow})]\\
&= -2N(U'-\frac{J}{2})\sum_{\alpha\neq\beta} n_\alpha n_\beta + \frac{2}{N}(U'-\frac{J}{2})\sum_{\mathbf{i},\alpha\neq\beta}[n_\beta(\sum_{\mathbf{k},\mathbf{k}'} e^{-i\,(\mathbf{k}-\mathbf{k}')\cdot\mathbf{i}} c^\dagger_{\mathbf{k},\alpha,\uparrow} c_{\mathbf{k}',\alpha,\uparrow}\\
&\quad + \sum_{\mathbf{k},\mathbf{k}'} e^{-i\,(\mathbf{k}-\mathbf{k}')\cdot\mathbf{i}} c^\dagger_{\mathbf{k},\alpha,\downarrow} c_{\mathbf{k}',\alpha,\downarrow})]\\
&= -2N(U'-\frac{J}{2})\sum_{\alpha\neq\beta} n_\alpha n_\beta\\
&\quad +2(U'-\frac{J}{2})\sum_{\alpha\neq\beta}\sum_{\mathbf{k},\mathbf{k}'}[n_\beta(\delta(\mathbf{k}-\mathbf{k}')c^\dagger_{\mathbf{k},\alpha,\uparrow} c_{\mathbf{k}',\alpha,\uparrow} + \delta(\mathbf{k}-\mathbf{k}')c^\dagger_{\mathbf{k},\alpha,\downarrow} c_{\mathbf{k}',\alpha,\downarrow})]\\
&= -2N(U'-\frac{J}{2})\sum_{\alpha\neq\beta} n_\alpha n_\beta + 2(U'-\frac{J}{2})\sum_{\mathbf{k},\beta\neq\alpha} n_\beta(c^\dagger_{\mathbf{k},\alpha,\uparrow} c_{\mathbf{k},\alpha,\uparrow} + c^\dagger_{\mathbf{k},\alpha,\downarrow} c_{\mathbf{k},\alpha,\downarrow}),
\end{aligned}
$$

$$
\begin{aligned}
H_3 &= \frac{JN}{2}\sum_{\alpha<\beta} m_\alpha m_\beta - \frac{J}{2}\sum_{\mathbf{i},\alpha\neq\beta} m_\alpha e^{i\,\mathbf{Q}\cdot\mathbf{i}}(n_{\mathbf{i},\beta,\uparrow} - n_{\mathbf{i},\beta,\downarrow}) \qquad (2.21)\\
&= \frac{JN}{2}\sum_{\alpha<\beta} m_\alpha m_\beta - \frac{J}{2N}\sum_{\mathbf{i},\alpha\neq\beta} m_\alpha e^{i\,\mathbf{Q}\cdot\mathbf{i}}(\sum_{\mathbf{k}} e^{-i\,\mathbf{k}\cdot\mathbf{i}} c^\dagger_{\mathbf{k},\beta,\uparrow}\sum_{\mathbf{k}'} e^{i\,\mathbf{k}'\cdot\mathbf{i}} c_{\mathbf{k}',\beta,\uparrow}\\
&\quad - \sum_{\mathbf{k}} e^{-i\,\mathbf{k}\cdot\mathbf{i}} c^\dagger_{\mathbf{k},\beta,\downarrow}\sum_{\mathbf{k}'} e^{i\,\mathbf{k}'\cdot\mathbf{i}} c_{\mathbf{k}',\beta,\downarrow})\\
&= \frac{JN}{2}\sum_{\alpha<\beta} m_\alpha m_\beta - \frac{J}{2N}\sum_{\mathbf{i},\alpha\neq\beta} m_\alpha(\sum_{\mathbf{k},\mathbf{k}'} e^{-i\,(\mathbf{k}-\mathbf{k}'-\mathbf{Q})\cdot\mathbf{i}} c^\dagger_{\mathbf{k},\beta,\uparrow} c_{\mathbf{k}',\beta,\uparrow}\\
&\quad - \sum_{\mathbf{k},\mathbf{k}'} e^{-i\,(\mathbf{k}-\mathbf{k}'-\mathbf{Q})\cdot\mathbf{i}} c^\dagger_{\mathbf{k},\beta,\downarrow} c_{\mathbf{k}',\beta,\downarrow})\\
&= \frac{JN}{2}\sum_{\alpha<\beta} m_\alpha m_\beta - \frac{J}{2}\sum_{\alpha\neq\beta}\sum_{\mathbf{k},\mathbf{k}'} m_\alpha(\delta(\mathbf{k}-\mathbf{k}'-\mathbf{Q})c^\dagger_{\mathbf{k},\beta,\uparrow} c_{\mathbf{k}',\beta,\uparrow}\\
&\quad -\delta(\mathbf{k}-\mathbf{k}'-\mathbf{Q})c^\dagger_{\mathbf{k},\beta,\downarrow} c_{\mathbf{k}',\beta,\downarrow})\\
&= \frac{JN}{2}\sum_{\alpha<\beta} m_\alpha m_\beta - \frac{J}{2}\sum_{\mathbf{k},\beta\neq\alpha} m_\beta(c^\dagger_{\mathbf{k}+\mathbf{Q},\alpha,\uparrow} c_{\mathbf{k},\alpha,\uparrow} - c^\dagger_{\mathbf{k}+\mathbf{Q},\alpha,\downarrow} c_{\mathbf{k},\alpha,\downarrow}).
\end{aligned}
$$

Therefore, the total Hamiltonian in momentum space is given by:

$$H_{\rm HF} = H_{\rm TB} + C + \sum_{\mathbf{k},\alpha,\sigma} \epsilon_\alpha c^\dagger_{\mathbf{k},\alpha,\sigma} c_{\mathbf{k},\alpha,\sigma} + \sum_{\mathbf{k},\alpha,\sigma} \eta_{\alpha,\sigma} (c^\dagger_{\mathbf{k},\alpha,\sigma} c_{\mathbf{k}+\mathbf{Q},\alpha,\sigma} + c^\dagger_{\mathbf{k}+\mathbf{Q},\alpha,\sigma} c_{\mathbf{k},\alpha,\sigma}), \tag{2.22}$$

where $\mathbf{k}$ runs over the extended first Brillouin zone, $H_{\rm TB}$ is the hopping term in Eq. (2.18), the constant C is

$$C = -NU \sum_\alpha \left(n_\alpha^2 - \frac{1}{4} m_\alpha^2 \right) - N(2U' - J) \sum_{\alpha \neq \beta} n_\alpha n_\beta + \frac{NJ}{2} \sum_{\alpha < \beta} m_\alpha m_\beta, \tag{2.23}$$

where N is the number of sites, and the following definitions were introduced:

$$\epsilon_\alpha = U n_\alpha + (2U' - J) \sum_{\beta \neq \alpha} n_\beta, \tag{2.24}$$

$$\eta_{\alpha,\sigma} = -\frac{\sigma}{2} \left(U m_\alpha + J \sum_{\beta \neq \alpha} m_\beta \right). \tag{2.25}$$

The parameters n_α and m_α can be obtained self-consistently by minimizing the energy via an iterative process. During the iterations $\sum_\alpha n_\alpha = n$ was enforced at each step, such that the total charge density is a constant.

2.2.3 Self-consistent Solving Method

In the Hartree-Fock approximation, the Hamiltonian can be solved numerically by minimization of the total energy self-consistently. The key in this process is to find a set of "correct" values for the HF expectation $\langle c^\dagger_{\mathbf{i},\alpha,\sigma} c_{\mathbf{j},\beta,\sigma'} \rangle$, which corresponds to the ground state with the minimal energy globally. The optimal expectation values can be obtained iteratively by the following steps: (1) Choose the initial values for $\langle c^\dagger_{\mathbf{i},\alpha,\sigma} c_{\mathbf{j},\beta,\sigma'} \rangle$ to start with. Theoretically, the initial values can be chosen randomly, however, using an educated guess will make convergence quicker. (2) Build the Hamiltonian in a matrix form with the new expectations. Then the matrix can

be diagonalized, producing all the eigenvalues and eigenvectors. (3) With all the information about the ground state and chemical potential, the new expectations $\langle c^{\dagger}_{\mathbf{i},\alpha,\sigma} c_{\mathbf{j},\beta,\sigma'} \rangle$ can be calculated from the eigenvalues and eigenvectors in *STEP* (2). (4) Compare the old and new expectations to test whether they are converged or not. If not, then go to *STEP* (2) recursively. If they are converged, this means the "correct" $\langle c^{\dagger}_{\mathbf{i},\alpha,\sigma} c_{\mathbf{j},\beta,\sigma'} \rangle$ for this system is found. And therefore some of the physical quantities, such as the one-particle spectral function ($A(\mathbf{k},\omega)$), the density of states (DOS) and others can be calculated by using this HF ground state.

Chapter 3

Neutron and ARPES constraints on the couplings of the multiorbital Hubbard model for the iron pnictides

3.1 Introduction

According to the angle-resolved photoemission experiments (ARPES) [Yang et al. (2009); Shimojima et al. (2010)] and *ab-initio* calculations [Cao et al. (2008)] for iron-based materials, all five d-orbitals of Fe dominate the bands near the Fermi energy, while the As $4p$ orbitals contribute more to the bands below the Fermi energy. Therefore, a theoretical study of pnictides cannot rely on just one orbital, as in the case of the cuprates, but it needs a multiorbital approach [Cao et al. (2008)]. Having to consider multiple orbitals severely restricts the available tools to carry out unbiased computer-based investigations of Hubbard multiorbital models. As a consequence, several studies have been restricted to mean-field approximations. Fortunately, this

is not a drastic limitation for the case of the undoped systems, since similar mean-field approximations for the cuprates are known to capture qualitatively the essence of the magnetic states [Schrieffer et al. (1989)]. In fact, mean-field-based efforts for the pnictides have already reported the presence of a state that is simultaneously metallic and magnetic [Yu et al. (2009)]. However, the study of the intermediate coupling regime, where the magnetic-metallic state was found, establishes a considerable challenge to theory since an intermediate region of couplings is often more difficult to analyze than either extreme of large or small U [Dai and Dagotto (2012)]. In addition, a multiorbital Hubbard approach needs at least two couplings: the on-site intra-orbital Hubbard repulsion U and the on-site Hund coupling J. A third parameter, the on-site inter-orbital repulsion U', is then defined by the well-known relation $U = U' + 2J$ arising from symmetries in orbital space [Oleś (1983)]. Having two couplings increases further the complexity of the analysis and the comparison between different approaches since there is at present no universally accepted range of U and J that is considered realistic by the community of experts. In fact, it would be quite desirable to restrict the values of the U and J couplings to a much narrower range, where qualitative agreement with experiments is observed.

In this chapter, our goal is to use experimental neutron scattering and photoemission data for the undoped pnictide parent compounds, supplemented by their well-known metallic properties, to establish lower and upper bounds on the couplings U and J of multiorbital Hubbard models. By focusing on a more restricted set of couplings, our results will guide future theoretical efforts into a realistic regime for the pnictides. Our calculations are based on the previously used and tested mean-field approximation [Yu et al. (2009)], allowing us to calculate a variety of observables that are then compared against experimental results to establish the proper ranges for U and J. To carry out this theory-experiment comparison the focus here is on the results of two powerful experimental techniques. One of them is neutron scattering and the other is Angle Resolved Photoemission (ARPES).

Table 3.1: Parameters for the tight-binding portion of the three-orbital model used here. The overall energy unit is electron volts.

t_1	t_2	t_3	t_4	t_5	t_6	t_7	t_8	Δ_{xy}
0.02	0.06	0.03	-0.01	0.2	0.3	-0.2	$-t_7/2$	0.4

3.2 The model Hamiltonians

In this chapter, the three-orbital Hubbard model introduced in Ref. [Daghofer et al. (2010b)] will be used first. This model is purely based on the d electrons of Fe and it considers only the three orbitals d_{xz}, d_{yz}, and d_{xy}, widely believed to be the most relevant orbitals at the Fermi surface for the pnictides. The actual values for the hopping amplitudes are in Table 3.1. The Coulombic interacting portion of the three-orbital Hamiltonian is standard multi-orbital Hubbard interaction, given in Chapter. 1

In addition, two five-orbital models (also based only on the d electrons of Fe) have also been used. By supplementing the three-orbital model by more complicated five orbital versions, our main goal is to verify the self-consistency of our approach. In other words, if the many models, with similar Fermi surfaces by construction, would give quite different ranges of couplings for the compatibility with neutron and ARPES results, then this would raise concerns about the entire calculation. It turns out that, as shown below, the J/U and U ranges that are found to be physically reasonable are similar in all cases, demonstrating that our approach is self-consistent. With regards to the specific five-orbital models used here, the tight-binding parameters of one of them are in the Appendix A, while another set of hoppings is from Ref. [Graser et al. (2009)]. At $U = 0$, all these models provide a Fermi surface (see below) that compares well with experiments and band structure calculations for the 122 compounds. The

Coulombic interactions for five-orbitals are the obvious generalization of the terms used for three-orbitals.

3.3 Results for the Three-Orbital Model

Our discussion of results starts with the three-orbital model. Some aspects of this discussion have been briefly mentioned in other publications, thus references to those previous efforts are provided where appropriate.

3.3.1 Comparison with neutron scattering experiments

Figure 3.1 contains the mean-field order parameter (m) at wavevector $(\pi, 0)$ vs. U. The plotted values for m arise from the numerical solution of the mean-field equations discussed in the previous section. For small values of J/U, such as 0.00 and 0.05, in Fig. 3.1 m discontinuously jumps from zero to a robust value at a critical U. While such a discontinuity is observed in all models discussed in this paper, its origin is not universal. It is caused by a metal-insulator transition in a four-band model, see Sec. II.C.4 of Ref. [Yu et al. (2009)]. In the three-orbital model, the discontinuity only coincides with the opening of a gap for smaller $J/U \lesssim 0.15$, and is rather marked by the sudden onset of strong orbital order, with a close competition between substantial alternating and nearly perfect ferro-orbital order [Daghofer et al. (2010b)]. For larger $0.15 \lesssim J/U \lesssim 0.22$, states with both types of orbital order can remain metallic for a small range of U just above the onset of strong orbital order, but the FS is qualitatively very different from ARPES results, e.g. it does not feature any sign of hole pockets around the Γ point [Daghofer et al. (2010b)]. At or rapidly after the critical U, the density of states develops a gap (not shown), signaling insulating behavior, in contradiction with the experimentally observed (bad) metallic character of the undoped pnictides. Moreover, as a consequence of the discontinuity, the order parameter m in the range of small J/U never reaches the realistic values for pnictides

reported in neutron scattering experiments, i.e. [0.25,1.0] μ_B for $(\pi, 0)$ magnetic order. Thus, these results for small J/U start illustrating one of the main messages of this chapter, namely that within the mean-field approximation used in our effort the request of qualitative agreement with the experimental properties of the undoped pnictides imposes severe constraints on the values of U and J/U for the multi-orbital Hubbard models. In particular, it is clear that $J/U = 0.00$ and 0.05 do not seem physically appropriate to describe the pnictides.

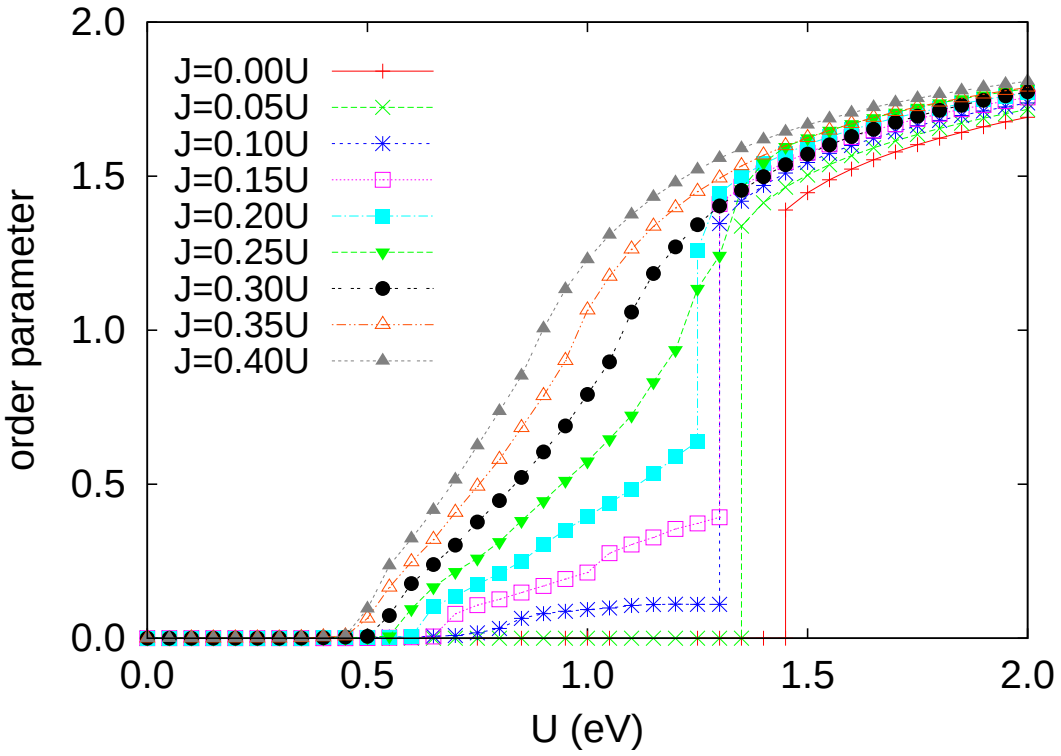

Figure 3.1: Mean-field order parameter at wavevector $(\pi, 0)$ vs. U (in eV units) for the three-orbital model discussed in the text, and parametric with the values of J/U indicated.

As J/U increases further, m now develops (becomes nonzero) at an earlier critical value of U, allowing for a proper description of materials with weak magnetic order parameters such as the "1111" family. Note that for $J/U = 0.10$, 0.15, and 0.20 , a discontinuity is still present in m vs. U, so not all values of the order parameter m are possible, while for larger J/Us the m curves are no longer discontinuous. $J/U = 0.50$ is the largest ratio that should be considered to avoid a negative U' due to the relation $U = U' + 2J$. Thus, adding this information to the results for m and its comparison with neutron scattering, the proper range of J/U couplings naively becomes $\sim [0.10, 0.50]$, with U larger than the first critical value where m develops. However, if in addition it is considered that J should be smaller than U', then this reduces the range further to $[0.10, 0.33]$, since $J = U'$ at $J/U = 1/3$.

3.3.2 Comparison with ARPES experiments

As discussed in Sec. 3.1, another experimental source of information that can be used to reduce the allowed range of couplings in the Hubbard model is provided by the ARPES results for undoped pnictides. As previously mentioned, a common generic feature of several ARPES experiments at low temperatures in the SDW phase is the development of "extra" features (pockets) near the original Γ-point hole pockets of the noninteracting limit. To search for these features, within our mean-field approximation the one-particle spectral function $A(\mathbf{k}, \omega)$ has been calculated, and the Fermi surface results have been analyzed in a wide range of U and J/U, using a δ-function broadening 0.025 eV.

Shown in Fig. 3.2 are representative results of our ARPES calculations (see also Refs. [Daghofer et al. (2010b,a)]). The focus is on a range of J/U and U where mean-field ARPES contains a Γ-point hole pocket, as in the original $U = 0$ bandstructure (presumably corresponding to the high temperature non-magnetic regime as well), and in addition "satellite" pockets as in ARPES, in between the original hole and electron pockets along the k_x axis. The results have not been folded, but are

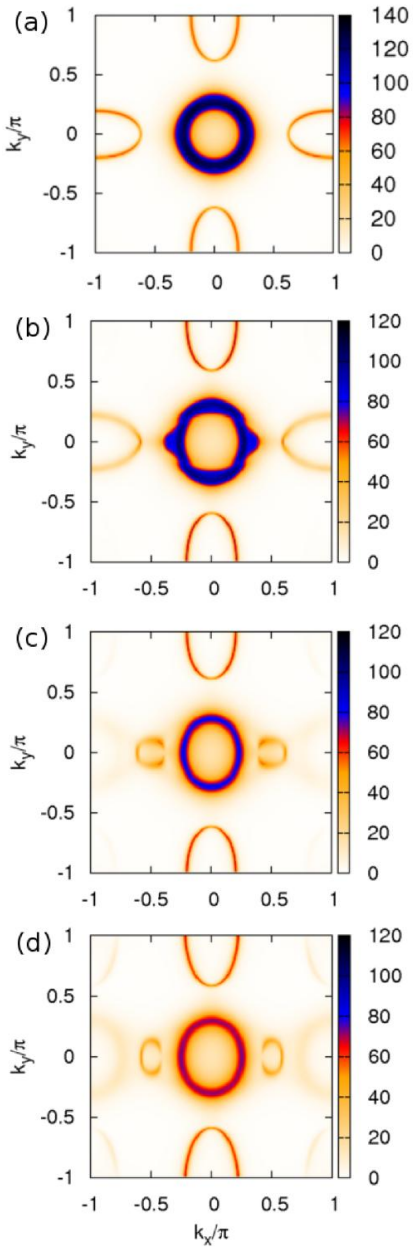

Figure 3.2: Unfolded mean-field Fermi surfaces for the three-orbital model corresponding to (m=order parameter) (a) $U = 0$, as reference (there are two hole pockets at Γ but they appear merged due to the broadening used for plotting); (b) $J/U = 0.33$, $U = 0.6$, $m = 0.2$; (c) $J/U = 0.20$, $U = 1.0$, $m = 0.4$; and (d) $J/U = 0.25$, $U = 1.05$, $m = 0.6$.

representative of a single-domain spin order wavevector, in this case $(\pi, 0)$, and with only one Fe per unit cell. Figure 3.2 shows representative cases where these satellites are clearly present (the satellite pockets tend to be electron-like for small U, switching to hole-like for slightly larger, but still realistic, values of U. For more details see Ref. [Daghofer et al. (2010b)]). The corresponding values of J/U and U are indicated in the figure caption. These physically acceptable Fermi surfaces from the ARPES perspective are found in the same approximate range of couplings as those selected from the m/neutrons perspective, as discussed above. It has been suggested before that a reduced ordered magnetic moment goes together with realistic $A(\mathbf{k}, \omega)$ in numerical approaches like density-functional theory [Yi et al. (2009)] and the present mean-field scheme [Daghofer et al. (2010a)], and we see here that this is not accidental, but that the analysis of both neutrons and ARPES are mutually consistent over a larger parameter range, as well as for a variety of models, see Sec. 3.4. The four panels shown are qualitatively similar and further refinements in the so-called "physical region" (see Fig. 3.4) will need better tools for calculations and more accurate ARPES experiments.

In Fig. 3.3, some of the full spectral functions are shown, and compared with the U=0 case. The appearance of V-shaped features, that induce the presence of satellite pockets, is clear in these figures. These mean-field results for $A(\mathbf{k}, \omega)$ are qualitatively consistent with ARPES experiments for the pnictides that have reported similar V-shaped branches [Shimojima et al. (2010)].

The results of Fig. 3.2 are in qualitative agreement with experiments, as already remarked in Ref. [Daghofer et al. (2010a)]. Moreover, our comprehensive analysis of $A(\mathbf{k}, \omega)$ has shown that these features do not appear in other regions of the U-J/U phase diagram. For instance, before the critical U where m develops from zero there are no satellite pockets, since they arise from the nonzero magnetic order and nesting effects. In the other extreme of U couplings larger than those used in Fig. 3.2, the Hubbard model simply becomes insulating (as discussed before in Ref. [Yu et al. (2009)]), and there is no longer a Fermi surface.

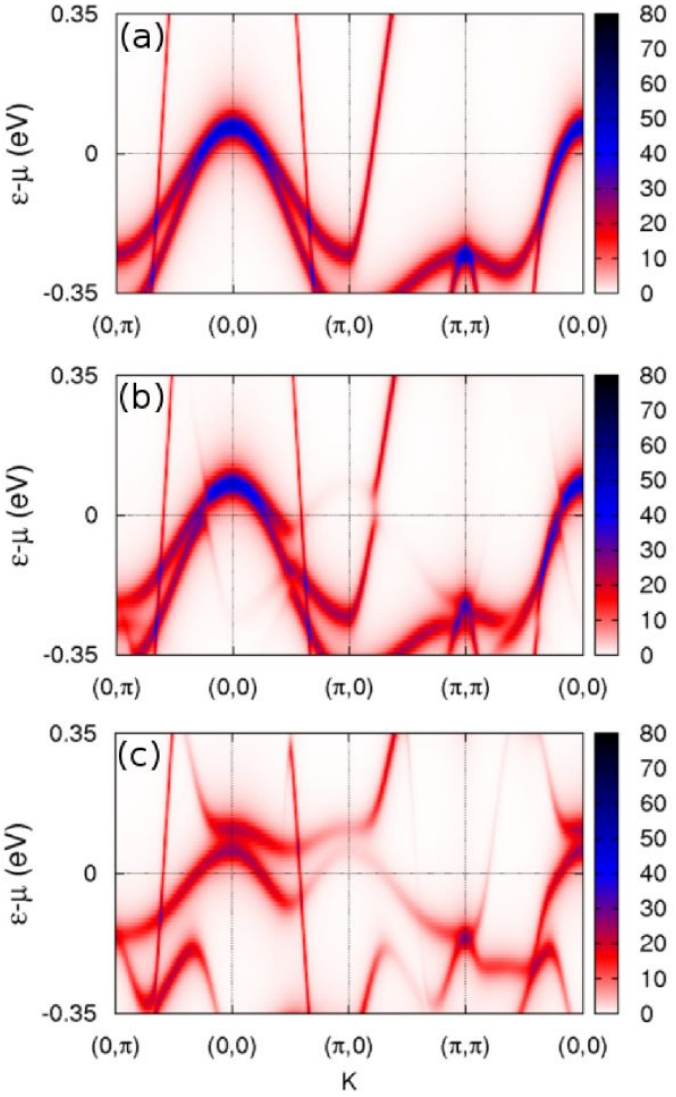

Figure 3.3: Unfolded band structure mean-field results for the three-orbital model and cases (a) $U = 0$, as reference; (b) $J/U = 0.33$, $U = 0.6$, $m = 0.2$; (c) $J/U = 0.25$, $U = 1.05$, $m = 0.6$. Panels (b) and (c) show a V-shaped pocket in between the $(0, 0)$ and $(\pi, 0)$ points. The scale used (arbitrary units) is on the right of the panels.

3.3.3 Summary phase diagram for three orbitals

The values of the order parameter m and their comparison with neutron scattering results, and the Fermi surfaces and their comparison with photoemission experiments, lead us to the mean-field phase diagram shown in Fig. 3.4, one of the main results of this chapter. In this figure, the range of U-J/U couplings compatible with neutron-ARPES experiments is labeled "physical region". This region is relatively small, providing substantial constraints on the parameters to be used in three-orbital Hubbard model investigations. If U is smaller than in the physical region, then the state is not magnetic; if U is larger, the state is insulating or it has a much distorted Fermi surface. If J/U is smaller than in the physical region, there is no room for the small and intermediate value order parameters found in neutron scattering; if J/U is larger, then U' becomes too small or negative and thus unphysical.

It is important to clarify that our mean-field approximation does not incorporate the effect of fluctuations. For this reason this type of approximations are somewhat "rigid" and it can be expected [Zhou and Wang (2010)], although actual calculations are very difficult, that the true "physical region" may be larger than shown in Fig. 3.4. Thus, readers should consider the location of our "physical regions" as the center of a potentially broader area where agreement with experiments can be found. But this does not invalidate our main point: intermediate U's and intermediate J/U's are needed for agreement with available neutrons, transport, and photoemission experiments.

A final remark is with regards to the actual value of U of order just 1 eV in the physical region: this cannot be the bare U but must already incorporate the influence of screening in a model where the long-range Coulomb interactions are included. It is for this reason that standard metals in general tend to have very small Us when studied via Hubbard-like models, while it is known that the bare atomic values for U are always of several eVs [Miyake et al. (2010); Ishida and Liebsch (2010)].

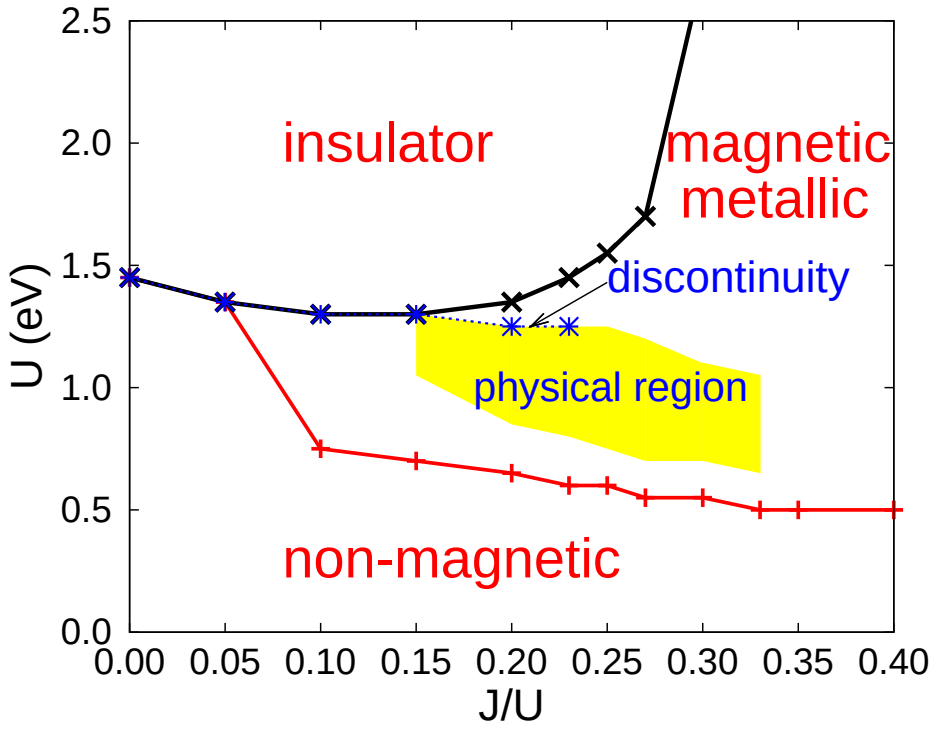

Figure 3.4: Phase diagram for the three-orbital model obtained with the mean-field approximation described in the text. The "physical region" in yellow is the regime of couplings found to be compatible with neutron and photoemission experiments. The "non-magnetic" region corresponds to a regime where the state has a zero order parameter. In the "insulator" region, there is no Fermi surface and the state is insulating. The "discontinuity" label corresponds to the discontinuous jump in the order parameter shown in Fig. 3.1. The entire "magnetic metallic" regime could in principle have been compatible with experiments, but only in the yellow highlighted region is that m is sufficiently small-intermediate in value and the Fermi surface has satellite pockets near the Γ-point hole pockets.

3.4 Results for Five-Orbital Models

In this section, results for two five-orbital models are presented, with a similar organization as for three orbitals. The hopping amplitudes and on-site energies of a novel "Model 1" are provided in the Appendix (using as criterion for their determination finding qualitative agreement with band calculations). The more accurate "Model 2" is the model introduced in Ref. [Graser et al. (2009)], where the reader can find the actual values of the parameters. These two models generate similar Fermi surfaces, but the values for the hopping amplitudes are rather different. Thus, they are useful to test whether our conclusions do or do not depend on small details. Indeed, an overall conclusion of our study is that the "physical region" is qualitatively similar for all the models analyzed in this manuscript. Both models studied in this section are at electronic density $n = 6.0$ in order to address the parent compounds. The δ-function broadening used here is 0.01 eV.

3.4.1 Summary phase diagram for the five orbitals Model 1

Similarly as for three orbitals, here a summary phase diagram is provided for the five-orbital Model 1 in Fig. 3.5. The labeling convention is the same as for three orbitals in Fig. 3.4. Using the information about neutron scattering and order parameters restricts U and J/U simply to be between the non-magnetic region and the discontinuity line. From these perspectives alone the "physical region" would be much larger than for the three orbitals case. However, considering the Fermi surface shape and its comparison with ARPES introduces more severe constraints, basically excluding the small J/U regime below 0.15. As a consequence, the final "physical region" ends up being similar to that obtained with the three-orbital model. As explained in Sec. 3.3.3, note also that fluctuations beyond our mean-field approximation are expected to render the "physical region" actually larger than displayed in Fig. 3.5.

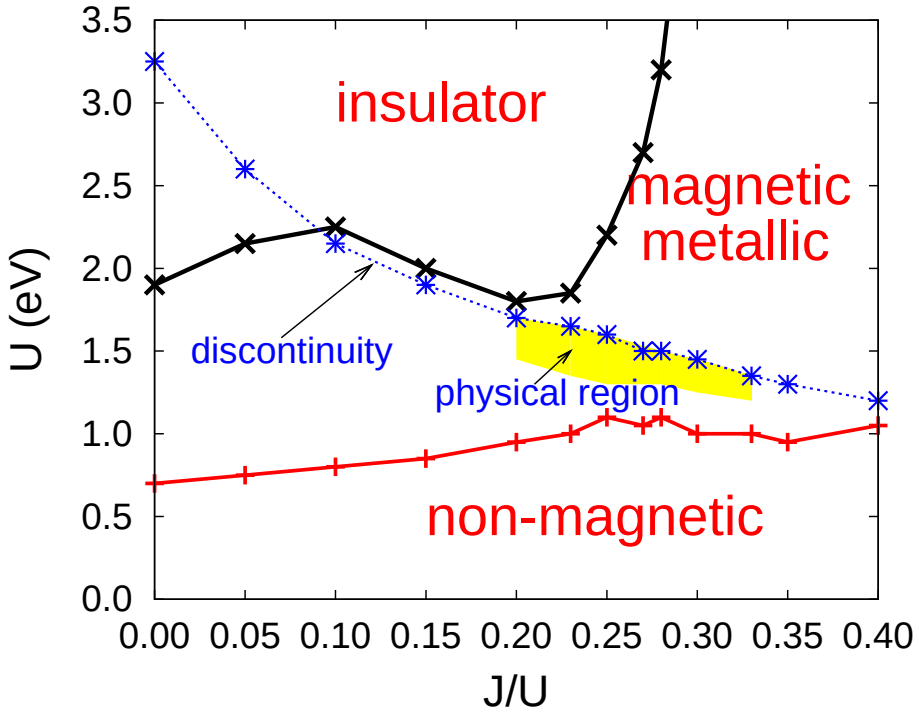

Figure 3.5: Phase diagram for the five-orbital Model 1 obtained with the mean-field approximation. As in Fig. 3.4 the "physical region" in yellow is the regime of couplings found to be compatible with neutron and photoemission experiments. The rest of the notation and details were already explained in Fig. 3.4.

3.4.2 Summary phase diagram for the five orbitals Model 2

As for the other models considered in this Chapter, in Fig. 3.6 a summary phase diagram is provided for the five-orbital Model 2. The labeling convention is the same as in Figs. 3.4 and 3.5, as well as the procedure to establish the so-called "physical region". The approximate location of this region with regards to U and J/U is similar to that reported in Figs. 3.4 and 3.5, showing again that our conclusions do not strongly depend on details. The physical region in Fig. 3.6 is narrow along the U axis direction because m changes rapidly with increasing U, at small m. But, as discussed in Sec. 3.3.3, fluctuations beyond mean-field approximations are expected to expand the size of the physical regions of the various models.

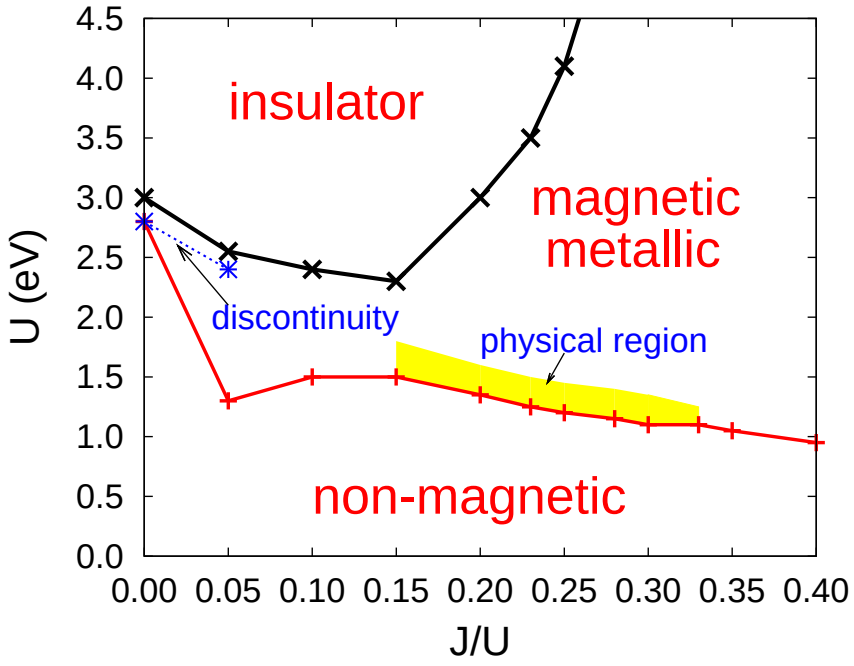

Figure 3.6: Phase diagram for the five-orbital Model 2 obtained with the mean-field approximation. As in Figs. 3.4 and 3.5, the "physical region" in yellow is the regime of couplings found to be compatible with neutron and photoemission experiments. The rest of the notation and details were already explained in Fig. 3.4.

Chapter 4

Charge stripes in the two-orbital Hubbard model for iron pnictides

4.1 Introduction

The nature of the undoped ground state of Hubbard models and the dominant pairing mechanisms upon doping has been addressed by using mean-field, random phase approximation, and computational techniques [Kuroki et al. (2008); Si and Abrahams (2008); Seo et al. (2008); Graser et al. (2009); Daghofer et al. (2008); Moreo et al. (2009b); Raghu et al. (2008); Yu et al. (2009)]. While the superconductivity and $(\pi, 0)$ magnetism have received most of the attention, recent experiments have revealed an even more complex behavior in pnictides. For example, inelastic neutron scattering (INS) experiments reported evidence for spin incommensurability (spin IC) in the superconducting state of the hole very overdoped pnictide KFe_2As_2 [Lee et al. (2011)]. This material does not have electron-pockets in its band structure due to the heavy doping (50%) and, as a consequence, nesting mechanisms cannot produce the spin IC, whose origin then remains puzzling. Neutron studies for $FeSe_{0.5}Te_{0.5}$ have also reported low-energy spin IC peaks near the spin resonance [Lee et al. (2010)]. Electron-doped pnictides such as $Ba(Fe,Co)_2As_2$ do not show spin IC at low energies

[Lester et al. (2010); Laplace et al. (2009)], but above 50 meV there is a splitting of the $(\pi, 0)$ peak.

In parallel to these developments, scanning tunneling microscopy (STM) experiments on underdoped $Ca(Fe_{0.97}Co_{0.03})_2As_2$ reported the existence of static unidirectional electronic nanostructures of dimension 8 a_{Fe-Fe} (with a_{Fe-Fe} the inter-iron distance) along the a-axis [Chuang et al. (2010)]. This electronic nematic order state is qualitatively similar to those widely discussed in other materials, such as in the high-temperature superconductors based on copper [Zaanen and Gunnarsson (1989); Poilblanc and Rice (1989); Emery et al. (1999)]. Note that the lines of spins that point in the same direction, namely the orientation of the $(\pi, 0)$ spin stripes, is actually along the b-axis, namely the nematic order and the spin-stripe order are perpendicular to one another.

The spin IC and nematic order reveal new similarities between the Cu- and Fe-based high temperature superconductors, more than expected considering the widely accepted perception that the former are in the strongly correlated regime of Hubbard U couplings while the latter are at weak or intermediate coupling. In the Cu-oxide context, both spin IC and several electronic anisotropies in transport have been rationalized in terms of charge *striped* states, either static or dynamic [Emery et al. (1999)]. Could it be that similar states are also of relevance in the pnictides?

With this motivation, in this chapter the possible existence of charge striped states in Hubbard models for the pnictides will be explored. Within the real-space Hartree-Fock approximation, it will be shown that the two-orbital Hubbard model indeed displays charge striped states upon doping. The charge, spin, and orbital properties of these states will be discussed. The properties of the striped states reported below are robust when the coupling U is above the critical value needed to open a gap in the undoped limit. Considering the complex nature of multiorbital systems, it is important to document the properties of these striped states even in gapped regimes that at first sight are unrelated to undoped pnictides that are known to be (bad) metals. However, the charge amplitude of the stripes (namely the difference between

the largest and smallest values of the charge at every site in the striped state) decreases with decreasing gap, and an interesting observation is that (weak) stripes are still found upon doping the intermediate coupling magnetic and *metallic* state of the undoped limit for particular hopping parameters. This result is conceptually different from the previous investigations of stripes in doped large-U Hubbard insulators.

4.2 Model and Method

In this chapter, the Hubbard model based on the d_{xz} and d_{yz} Fe orbitals will be investigated. The use of these two orbitals is reasonable since they provide the largest contribution to the pnictide's Fermi Surface [Boeri et al. (2008)]. Studies involving models with more orbitals are certainly important, but they will be addressed only in future investigations after introducing the present novel findings based on two orbitals. A variety of other results that have recently been gathered for the two-orbital model [Daghofer et al. (2008); Moreo et al. (2009b); Nicholson et al. (2011)] have already clearly shown that this model is in good agreement with experiments in several respects, including the existence of $(\pi, 0)$-$(0, \pi)$ magnetic order, a Fermi surface that by construction is similar to those found in photoemission, and pairing channels that include the A_{1g} state (of which the s$\pm$ pairing is a special case) as well as competitors with B_{1g} and B_{2g} symmetries. Note also that the use of five orbital models would demand a much larger computational effort than reported here, since the diagonalizations used in the iterative procedure to solve the HF equations scales as $(2N)^4$, with N the number of sites of the real-space cluster and 2 the number of orbitals. Thus, a similar calculation for 5 orbitals will require $(5/2)^4 \sim 39$ times more computer time. It is for these reasons that it is reasonable to report first the analysis of the case of two orbitals, identifying the main tendencies, and then in the near future increase the number of orbitals.

As hopping amplitudes in the tight-binding portion of the model, fits to band calculations [Raghu et al. (2008)] as well as Slater-Koster (SK) hoppings [Daghofer

et al. (2008); Moreo et al. (2009b)] will be used. The electronic interaction is given by the standard Hubbard term, which has an intraorbital repulsion U, a Hund coupling $J_{\rm H}$, an interorbital repulsion U' (fixed as U'=U-2$J_{\rm H}$ here), and a pair-hopping term with coupling J'=$J_{\rm H}$ [Oleś (1983)]. The real-space Hartree Fock (HF) approximation (detail can be found in Chapter 2) will be employed here as many-body technique.

4.3 Results

Let us start the description of our main results using the Slater-Koster hoppings introduced in Refs.[Daghofer et al. (2008); Moreo et al. (2009b)]. A wide range of electronic densities $\langle n \rangle$ were numerically explored by varying the chemical potential μ. In most cases, the results of the HF model energy minimization were sufficiently clear that they admit a simple discussion, and the emphasis below will be on those special cases, such as $\langle n \rangle \sim 2.3$. At these densities, several starting configurations for the unknown expectation values that appear in the HF model were chosen via a random number generator and it was observed that the iterative process leads to nearly identical solutions or, if this was not the case, to local minima solutions with a higher energy. When different types of solutions were found, of course only those with the lowest energy were kept and analyzed.

Following the energy minimization criterion, the charge patterns found in some other cases were slightly more complicated, with segments of stripes clearly formed at the local level but sometimes with these segments not properly merged together to form nearly perfectly spaced stripes. Since these states still have all the characteristics of stripe states, it may occur that for a particular set of couplings some stripe configurations do not fit properly in the cluster sizes used and geometrical frustration effects may lead to the partial breaking of the stripes. So while the focus below is on the most clear cases, the other states found are all "stripy" in nature, thus our results seem generic of a broad range of couplings and densities [Lorenzana et al. (2008)].

Fig.4.1(a) contains a typical HF state that has been observed repeatedly in our studies, even using several different starting configurations for the iterations. It is clear that the charge is not uniformly distributed but it forms vertical stripes, breaking spontaneously rotational invariance. Of course, the $\pi/2$-rotated state is also a degenerate solution (horizontal stripes) and the convergence to one or the other depends on the randomly chosen initial state for the iterative process. Note that these stripes are "weaker" than the usual Cu-oxides HF stripes in the sense that the charge difference Δn ($\sim$0.15 in Fig.4.1(a)) between the maximum $n_{\max}$ and minimum $n_{\min}$ local charges is not as large as in the cuprates where Δn is of order 1. This simply arises from the values of the coupling U that were investigated that are smaller for pnictides than cuprates, in units of the bandwidth. Also it is interesting to note that $n_{\min}$ in Fig.4.1(a) is 2.27. Thus, the regions in the striped state that have the less charge still deviate from the "undoped" limit, and they are electron doped as the rest of the striped state, while in the cuprates the regions between the hole stripes have densities very close to those of the undoped insulator. From this perspective, our striped states should be metallic, in agreement with the density-of-states (not shown) that has a nonzero weight at the chemical potential μ.

The expectation values of the spin at each site, defined as $\vec{s}_{\mathbf{i}}=\langle\sum_{\alpha,\sigma,\sigma'} c^{\dagger}_{\mathbf{i},\alpha,\sigma}\vec{\sigma}_{\sigma\sigma'}c_{\mathbf{i},\alpha,\sigma'}\rangle$, that correspond to the striped state shown in Fig.4.1(a) are given in Fig.4.1(b). The spin pattern is dominated by the $(0,\pi)$ configuration, with spins parallel along one axis and antiparallel along the other. However, at the locations of the maximum electronic densities in Fig.4.1(a), the $(0,\pi)$ spin order breaks locally and domain walls are formed [Mazin and Johannes (2009)], with the spins where the local charge is maximized presenting an orientation nearly perpendicular to the rest. In a HF minimization problem, where all the expectation values are entangled, it is difficult to establish if the spin state with walls drives the charge stripes or vice versa. But by analogy with the cuprates, it can be expected that the spin state $(0,\pi)$ tries to expel the extra charge since it is disruptive to such a state, and such excess charge is located at the walls where the spin does not maintain locally the $(0,\pi)$ order. Of

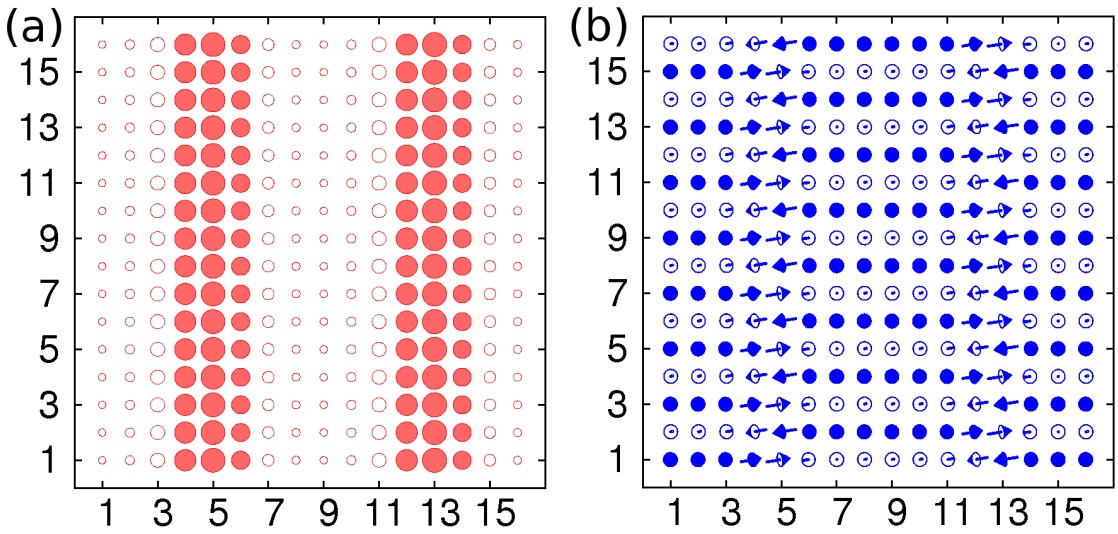

Figure 4.1: (a) Example of charge striped state found in the HF approximation to the two-orbital model, using the hoppings of Refs. [Daghofer et al. (2008); Moreo et al. (2009b)], $\langle n \rangle$=2.33, U=0.8, $J_{\rm H}/U$=0.25, and a 16×16 cluster. The size of the circles is linearly related to the charge, with the largest circles denoting $n_{\rm max}$=2.42 and the smallest $n_{\rm min}$=2.27. Here, and in the other figures, full (open) circles are used when the local density is larger (smaller) than the average. (b) Mean value of the spin in the state shown in (a). Note the presence of domain walls at the location of the charge stripes, inserted in a mainly $(0, \pi)$ background.

course, all these statements made for vertical stripes and spin $(0,\pi)$ order are the same for the rotated degenerate configuration with horizontal stripes and $(\pi,0)$ spin order.

The HF state Figs.4.1(a,b) has other interesting properties: *(i)* The orbital d_{yz} is more populated than d_{xz} in regions with the lowest local charge, i.e. where the spin order is locally $\sim(0,\pi)$, which should not be considered as indicative of long-range orbital order but instead it indicates an orbital weight "redistribution" induced by the spin order that breaks rotational invariance, as discussed elsewhere [Daghofer et al. (2010a)]. Where the local charge is the largest, on the other hand, both orbitals are populated approximately equally. *(ii)* The deviations from a perfect $(0,\pi)$ spin state induce a small shift away from $(0,\pi)$ in the spin structure factor peak position, towards (π,π). Then, the HF striped states can produce spin incommensurability, as found in some experiments. *(iii)* Note that the charge stripes and the spin stripes (i.e. the lines of parallel spins in the $(0,\pi)$ arrangement) are *perpendicular* to one another, as observed in the STM experiments where nematic order was reported [Chuang et al. (2010)].

Fig.4.2(a) contains another typical HF state with charge stripes that was found in our studies, at an electronic density $\langle n\rangle$ larger than in Fig.4.1(a), thus concomitantly inducing a reduction in the distance between stripes. It is interesting to observe that Δn is smaller to that in Fig.4.1(a), suggesting that there must be an "optimal" doping for vertical/horizontal stripe formation, as found in cuprate's investigations, since in the undoped case $\langle n\rangle$=2.0 there are no stripes and thus Δn=0. Also, note that our results even farther from $\langle n\rangle$=2.0 indicate a variety of complex patterns, with checkerboards, diagonal stripes, and other arrangements. However, since their associated spin orders are very different from the $(\pi,0)$ (or $(0,\pi)$) state prevailing in pnictides, and the doping is too large to be compared with available experimental results, those exotic states will not be described here. Presumably when the electronic density deviates substantially from the undoped case, then our results reach a regime

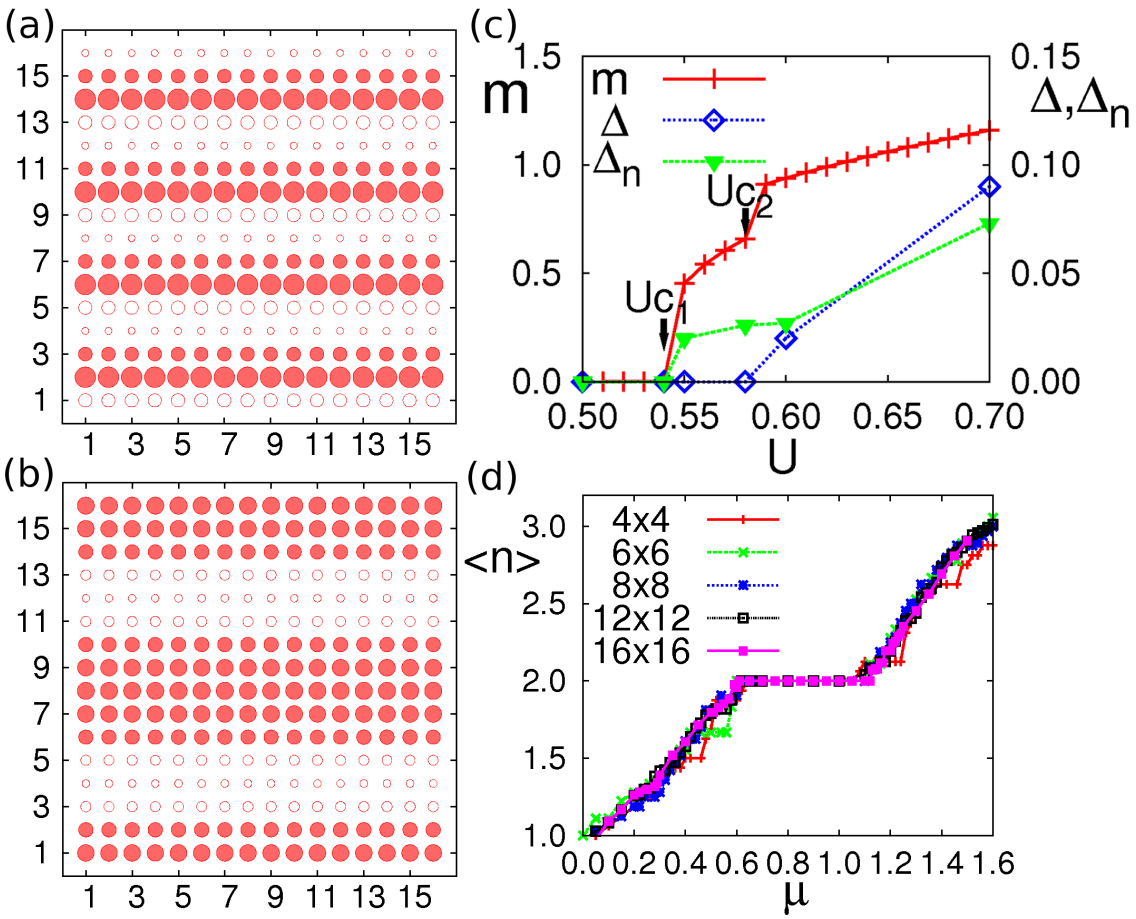

Figure 4.2: (a) HF charge striped state using the hopping amplitudes of Refs.[Daghofer et al. (2008); Moreo et al. (2009b)], at $\langle n\rangle$=2.45, U=0.8, and $J_{\rm H}/U$=0.25. The size of the circles is proportional to the charge, with $n_{\rm max}$=2.48 and $n_{\rm min}$=2.41. (b) Same as (a) but for $\langle n\rangle$=1.83, U=1.0, with $n_{\rm max}$=1.84 and $n_{\rm min}$=1.81. (c) $(\pi, 0)$ antiferromagnetic order parameter m, charge gap Δ (from $\langle n\rangle$ vs. μ), and Δn=$n_{\rm max}$-$n_{\rm min}$ at $\langle n\rangle\sim$2.3, as a function of U. (d) $\langle n\rangle$ vs. μ at U=1.0, $J_{\rm H}/U$=0.25, and various lattice sizes, suggesting that size effects are small in this quantity. Results at others U's appear equally well converged.

not yet found experimentally in these materials, or the two-orbital model breaks down.

Fig.4.2(b) contains results for the case of hole doping, and here the stripes are found to be weaker, with $\Delta n \sim 0.03$. At least for the hopping amplitudes of Refs.[Daghofer et al. (2008); Moreo et al. (2009b)], the stripe tendencies appear stronger for electron doping than for hole doping. Also, in the hole-doped case the lines of parallel spins tend to run parallel to the charge stripes, instead of perpendicular as in the electron-doped case. This parallel vs. perpendicular relative patterns of charge and spin may depend on details and may not be universal, thus they need to be investigated in more detail in the future.

Fig.4.2(c) displays Δn vs. U, at $\langle n \rangle \sim 2.3$, compared with results for the undoped limit, namely the $(\pi, 0)$ (or $(0, \pi)$) magnetic order parameter m and the charge gap Δ. While m rapidly grows with U at U_{c1}, Δ remains zero in a narrow region beyond U_{c1} and only after reaching a second critical value U_{c2} it slowly increases with increasing U. This intermediate region is both metallic and magnetic, and has been emphasized before as the regime of interest for pnictides [Yu et al. (2009); Luo et al. (2010)]. Δn follows Δ with decreasing U from strong coupling but it appears to survive, albeit with a small value, in the intermediate magnetic/metallic phase. If this result would survive the introduction of fluctuations beyond the HF approximation, the undoped metallic magnetic state would admit weak charge stripes upon doping, a conceptually novel result since previous stripe efforts have focused on their presence only when doping a Hubbard insulator. For those insulators the rationale for the presence of stripes was dominated by the fact that extra charges tend to disrupt the regular spin order of the undoped case. Thus, to reduce this "damage" to spin order, the extra charge is arranged forming stripes. Such a way to understand the stripes of the cuprates can be extended to pnictides even in the magnetic and metallic regime: the extra charge may need to be accumulated in patterns, as opposed to regularly distributed, to minimize the energy damage to the spin order. Note also that size

effects do not seem large here since some quantities are already converged on the 16×16 cluster (see Fig.4.2(d)).

The HF results obtained using another set of hopping amplitudes (Ref.[Raghu et al. (2008)]) are presented in Fig.4.3. In this case, the analysis was slightly more involved, since the convergence of the HF energy minimization was slower, with the iterative process for convergence sometimes ending in metastable states with charge inhomogeneous irregular patterns (but still displaying stripes locally). However, in many cases the convergence to a nearly perfect stripe pattern was clear. Panels Figs.4.3(a) and (c) display the charge order in the HF states at two different $\langle n \rangle$'s and two U's with a magnetic undoped state (the hopping unit t_1 of Ref.[Raghu et al. (2008)] is taken as 0.2 eV here, as in Ref.[Nicholson et al. (2011)]). In both cases, charge stripes can be identified, with Δn growing with U, as in Fig.4.2(c). At U=0.50 the charge gap is negligible, so these (weak) charge stripes appear in the metallic magnetic state. The associated spin patterns also present a striped arrangement, and the spin and charge stripes are perpendicular. There are some differences between the stripes of Figs.4.1 and 4.3, such as the stripe periodicity. These differences are to be expected since both sets of hopping parameters were constructed to produce similar undoped Fermi surfaces but their full band structures are different. However, it must be emphasized that with both sets of hoppings, charge stripes are found in several cases and, thus, their existence is a qualitative conclusion of our HF investigations.

4.3.1 Preliminary studies of the influence of Co doping on a striped state

The striped states found here could be of relevance to explain the static nematic state found via STM [Chuang et al. (2010)]. To test this hypothesis, a randomly-chosen set of lattice sites was selected to simulate the presence of Co-dopants via an on-site energy ϵ, and then the minimization of the HF model was again carried out in that background. A typical result is shown in Fig.4.4(a). It is observed that

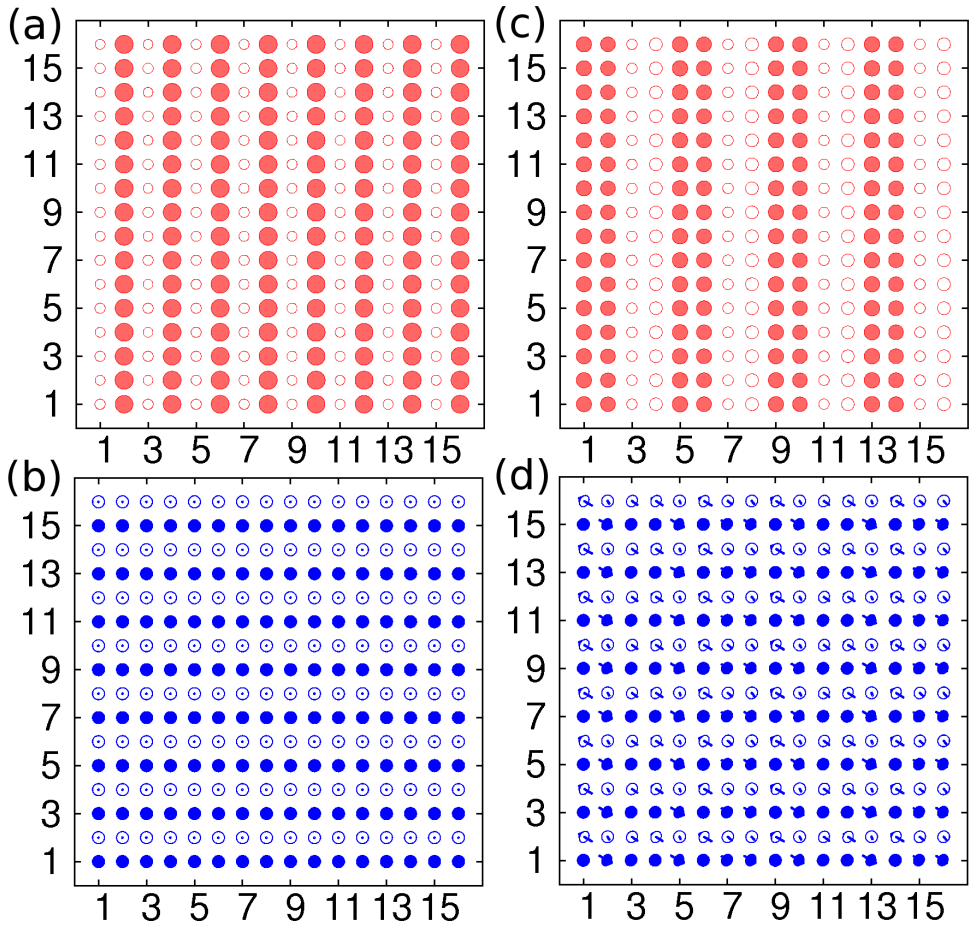

Figure 4.3: (a) Charge striped state solution of the HF two-orbital Hubbard model, using the hoppings of Ref.[Raghu et al. (2008)], $\langle n \rangle$=2.36, U=0.50, and $J_{\rm H}/U$=0.25. The size of the circles is proportional to the charge, with $n_{\rm max}$=2.365 and $n_{\rm min}$=2.361 (a very weak charge stripe). (b) Spin state associated with (a). (c) Same as (a) but for U=0.90, $\langle n \rangle$=2.14, $n_{\rm max}$=2.141, and $n_{\rm min}$=2.139 (d) Spin state associated with (c).

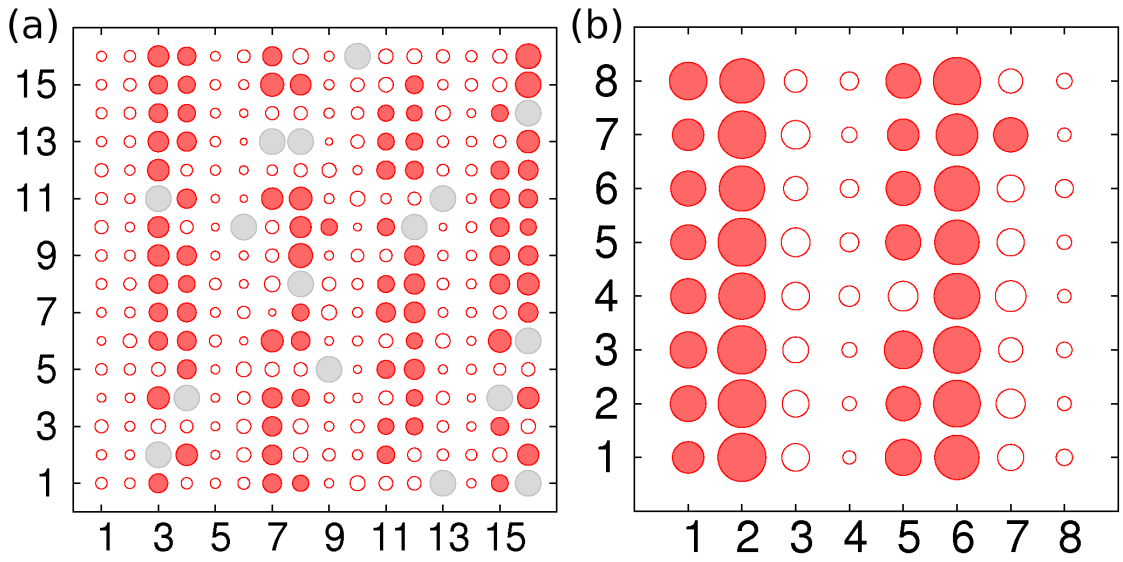

Figure 4.4: (a) Ground state of the HF Hamiltonian at $\langle n \rangle$=2.56, U=1.0, and $J_{\rm H}/U$=0.25, using the SK hoppings [Daghofer et al. (2008); Moreo et al. (2009b)] In the 16 sites shown in grey, there is an on-site energy ϵ=-0.85, that simulates the presence of quenched disorder, such as caused by Co doping. (b) Monte Carlo results (equilibrated snapshot) obtained using the two-orbital spin-fermion model of Ref.[Yin et al. (2010)] with SK hoppings [Daghofer et al. (2008); Moreo et al. (2009b)], $\langle n \rangle$=2.55, K=-1, $J_{\rm NN}$=$J_{\rm NNN}$=0.05, magnitude of the classical spins S=1, temperature 0.005 eV, and 45,000 steps. K is the Hund coupling between itinerant and localized spins. $J_{\rm NN}$ ($J_{\rm NNN}$) is the Heisenberg coupling between NN (NNN) localized spins, where NN stands for nearest neighbors and NNN for next nearest neighbors. The small deviation from a perfect stripe is caused by temperature.

this quenched disorder effectively cuts the long stripes into shorter segments, and the overall state qualitatively resembles those found with STM. Of course, only a tuning of couplings and electronic densities may render this agreement quantitative (for instance producing features of size 8 lattice spacings, as in experiments) and that effort is postponed for future work. Here, simply note that the charge and spin stripes found in our study tend to be perpendicular to one another, in nice agreement with the STM investigations.

4.3.2 Results for the spin fermion model

Striped states were also studied via the two-orbital spin-fermion model recently proposed [Yin et al. (2010)]. Using Monte Carlo techniques [Dagotto et al. (2001)], metastabilities limited the present effort to 8×8 clusters. In cases where good convergence was achieved, stripes were also found (Fig.4.4(b)). Thus, via the use of two rather different models and techniques the presence of charge non-uniformed states was confirmed.

Chapter 5

Study of the magnetic state of $K_{0.8}Fe_{1.6}Se_2$

5.1 Introduction

The discovery of superconductivity (SC) with T_c∼30 K in the heavily electron-doped 122 iron-chalcogenides $K_{0.8}Fe_{2-x}Se_2$ and (Tl,K)$Fe_{2-x}Se_2$ compounds [Guo et al. (2010)] provided another way to investigate the iron-based superconductors. Recent neutron scattering results for $K_{0.8}Fe_{1.6}Se_2$ [Bao et al. (2011)], with the Fe-vacancies arranged in a $\sqrt{5}\times\sqrt{5}$ pattern, revealed an unexpected magnetic and insulating state involving 2×2 Fe plaquettes that have their four Fe spins ferromagnetically ordered, and with these plaquettes coupled to each other antiferromagnetically [Ricci et al. (2011)]. The ordered magnetic moment is 3.31 μ_B/Fe, which is the largest among all Fe pnictide and chalcogenide superconductors, and the magnetic transition occurs at a high temperature T_N≈559 K. Angle-resolved photoemission (ARPES) experiments have revealed a Fermi surface (FS) with only electron-like pockets at Brillouin zone (BZ) corners, showing that the nesting between hole and electron pockets [Wang et al. (2011a,b)] is not sufficient to explain the superconducting phase in these compounds. Moreover, several other experiments have shown the possibility of phase separation,

which can explain some puzzling properties of these compounds. All these results certainly have challenged prevailing ideas for the origin of SC in these materials that were originally based on a nested FS picture and a metallic parent state [Dai and Dagotto (2012)].

In this chapter, a more fundamental five-orbital Hubbard model, without lattice distortions, is investigated. Our main result is that increasing the Hubbard coupling U and the Hund coupling J, a robust region of stability of the AF1 state is found. Our effort allows to display the regions of dominance of the many competing states in terms of U and J/U, facilitating a discussion on possible phase transitions among these states by varying experimental parameters. A sketch of the AF1 state and its two main competitors, the C and AF4 states, is in Fig. 7.1. Our results agree qualitatively in several respects with the phenomenological studies of Refs.[Yu et al., 2011; Yin et al., 2012] particularly if a combination of results of these investigations is made. Finally, also note that a recent study [Lv et al. (2011)] of the three-orbital Hubbard model [Daghofer et al. (2010b)] using mean-field techniques [Luo et al. (2010)] has also reported the existence of an AF1 state but with orbital order (OO). The relation with our results will also be discussed below.

5.2 Models and Methods

In this chapter, the standard five-orbital Hubbard model will be used, with the hopping amplitudes introduced by Graser et al. (2009). By construction, this model has a FS that is in close agreement with band structure calculations and angle-resolved photoemission results for the pnictides without vacancies. The presence of the realistic AF1 state in our results, as shown below, suggests that the same set of hopping amplitudes can be used in a system with Fe vacancies. The electronic density will be n=6.0, i.e. 6 electrons per Fe, for all the five-orbital model results presented below. The couplings are the on-site Hubbard repulsion U at the same orbital and the on-site Hund coupling J. The on-site inter-orbital repulsion U' satisfies U'=U-2J.

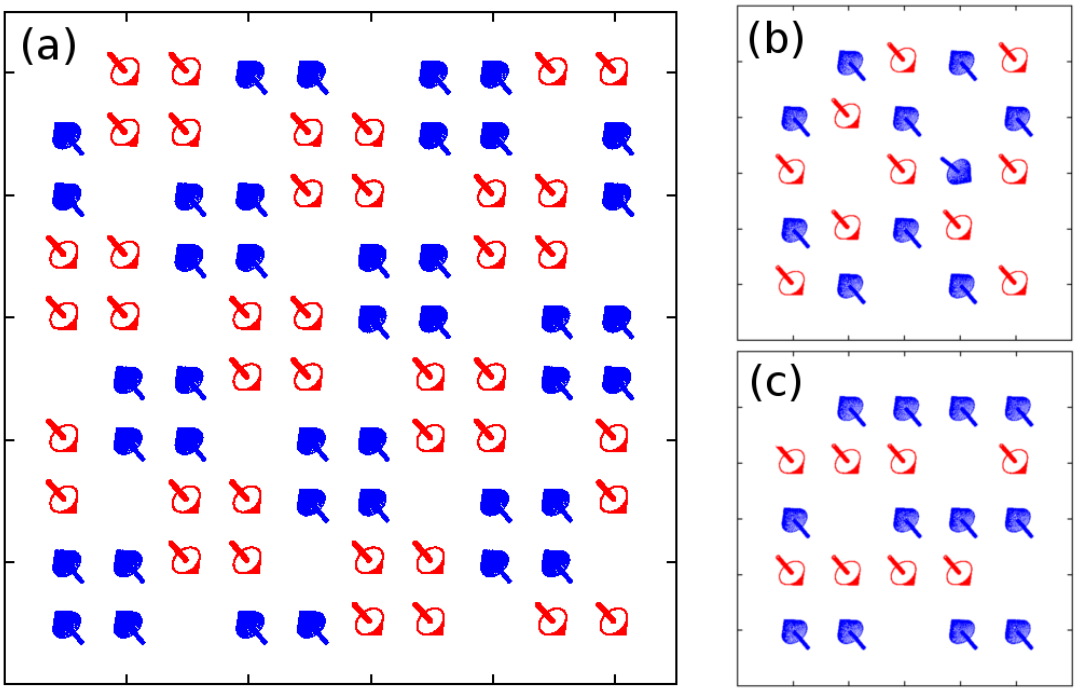

Figure 5.1: (a) Sketch of the AF1 state found to be stable in a region of the U-J/U phase diagram (see Fig. 5.2) in our HF approximation to the five-orbital Hubbard model, in agreement with neutron diffraction [Bao et al. (2011)]. (b) A competing state dubbed AF4 (stable at smaller J/U's in Fig. 5.2). (c) The C competing state. For (b) and (c), a subset of the 10×10 cluster used is shown.

The computational method that is employed to extract information from this five-orbital model relies on the study of a 10×10 cluster, as sketched in Fig. 7.1(a), using periodic boundary conditions. In this cluster, several vacancies and 2×2 building blocks fit comfortably inside, giving us confidence that the main local tendencies to magnetic order are not dramatically affected by size effects.

With regards to the actual many-body technique used to study the 10×10 cluster, here the real-space Hartree-Fock (HF) approximation was employed. This HF real-space approach was preferred over a momentum-space procedure in order to allow for the system to select spontaneously the state that minimizes the HF energy, at least for the finite cluster here employed. In practice, the many fermionic expectation values that appear in the HF formalism must be found iteratively by energy minimization. At the beginning of the iterative process, both random initial conditions as well as initial ordered states as shown in Fig. 7.1 were employed. After each of the computer runs using different initial conditions have reached convergence, at a fixed U and J/U, a mere comparison of energies allowed us to find the ground state for those particular couplings. In our setup, typical running times for one set of couplings U-J/U required approximately 20 hours of CPU time to reach convergence [Johnson (1988)] Dozens of computer cluster nodes have been used to complete our analysis in a parallel manner.

5.3 Results

The main results arising from the computational minimization process are summarized in the phase diagram shown in Fig. 5.2. Since the hopping parameters of Ref.[Graser et al., 2009] are already in eV units, our Hubbard coupling U is also displayed in the same units. The notation for the many competing phases used here is taken from Refs.[Cao and Dai, 2011a,b; Yu et al., 2011; Yin et al., 2012] to facilitate comparisons. The main result of the present work is that our phase diagram displays a robust region where the magnetic order unveiled by neutron diffraction [Bao et al. (2011)], see Fig. 7.1(a), is found to be stable. The ratio J/U needed for the

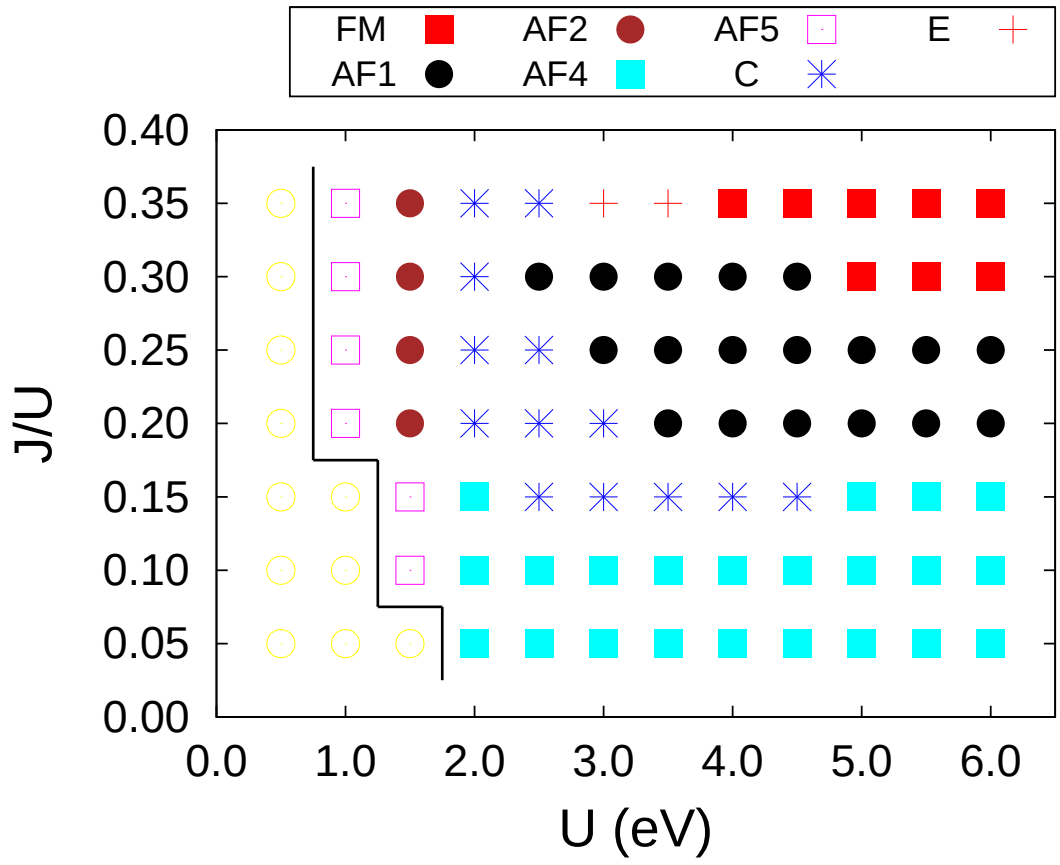

Figure 5.2: Phase diagram of the five-orbital Hubbard model with $\sqrt{5}\times\sqrt{5}$ Fe vacancies studied via the real-space HF approximation to a 10×10 cluster, employing the procedure for convergence described in the text. With increasing U, clear tendencies toward magnetic states are developed. The realistic AF1 state found in neutron scattering experiments [Bao et al. (2011)] appears here above J/U=0.15 and for U larger than 2.5 eV. The notation for the most important states is explained in Fig. 7.1 and for the rest in Refs.[Cao and Dai, 2011a,b; Yu et al., 2011; Yin et al., 2012]. The region with low-intensity yellow circles at small U is non-magnetic.

AF1 phase to be the ground state is in good agreement with previous estimations for the same model, although obtained in the absence of vacancies, based on the comparison of Hubbard model results against neutron and photoemission data [Luo et al. (2010)]. The ratio J/U is surprisingly similar between the pnictides and the chalcogenides. With regards to the actual value of U in eV's, the range unveiled in previous investigations that focused on the "1111" and "122" families of pnictides was approximately 1.5 eV (see Fig. 13 of Ref.[Luo et al., 2010)]. The increase to 2.5 eV in the present investigation is not surprising in view of the more insulating characteristics of materials such as $K_{0.8}Fe_{1.6}Se_2$, and suggests that merely adding vacancies to the intermediate U state of the pnictides (without vacancies) is not sufficient to stabilize the AF1 state but an increase in U is also needed. Finally, with regards to OO, none is observed in the AF1 state in the range of U shown in Fig. 5.2, i.e. for $U \leq 6$ eV. In this range, the electronic density of all the orbitals (d_{xz} and d_{yz} in particular) is independent of the site location in the cluster analyzed. However, upon further increasing U to 8 eV and beyond, the *same* OO pattern found in the three-orbital model [Lv et al. (2011)] appears in our calculations (not shown explicitly), with the populations of the d_{xz} and d_{yz} orbitals now being different at all sites. It seems that with five orbitals the AF1 state manifests itself both with and without OO, depending on U, while for three orbitals the intermediate phase with AF1 magnetic order and without OO is not present [Lv et al. (2011)].

Together with the realistic AF1 phase, Fig. 5.2 reveals several other states, and two of them are prominent. If keeping the ratio J/U constant but reducing U, the previously described C-type state (Fig. 7.1(c)) was found to be stable. This is reasonable since without Fe vacancies this state is the dominant spin order in the intermediate range of couplings, where the ground state is both metallic and magnetic [Luo et al. (2010)]. In $K_{0.8}Fe_{1.6}Se_2$, as the bandwidth is increased by, e.g., increasing the pressure, a transition from the AF1 to the C-state could be experimentally observed. In these regards, our conclusions agree with Ref.[Yin et al., 2012] that the C-state is the main competitor of the AF1 state. However, note that other states

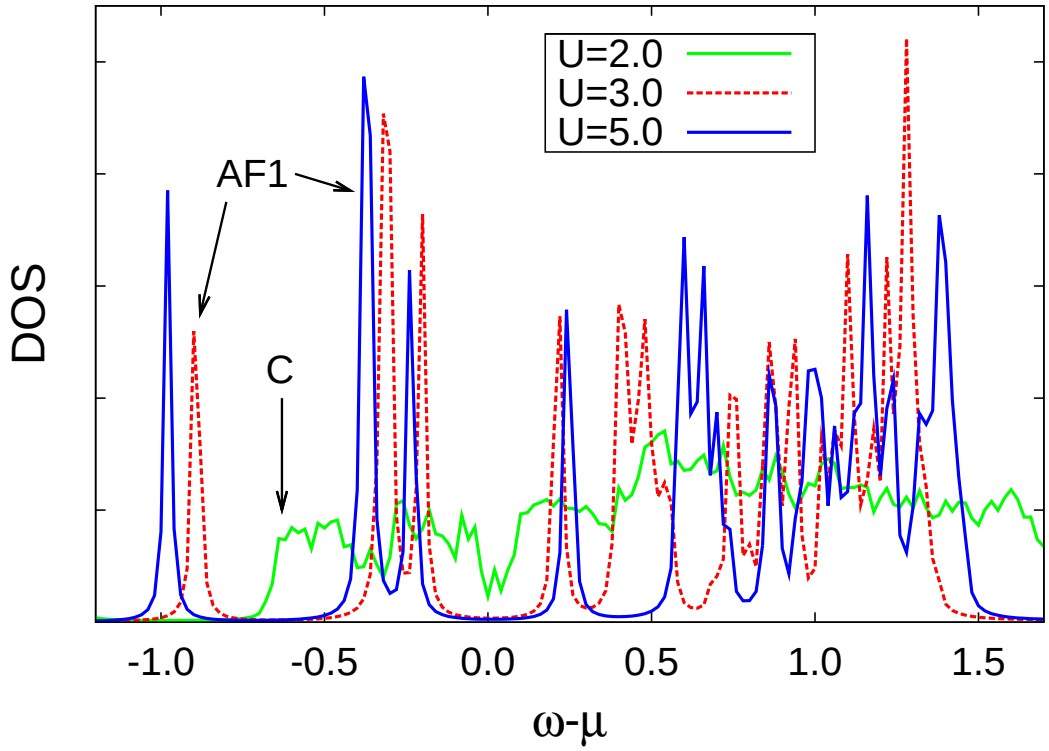

Figure 5.3: Density of states of the AF1 and C phases sketched in Figs. 7.1(a,c), at the U's indicated, J/U=0.25, and using a 10×10 cluster. The gap at the chemical potential suggests that the AF1 state (U=3 and 5) is an insulator, although with a mild U dependence in the value of this gap. On the other hand, the C state appears to have only a pseudogap at the Fermi level.

reported in Ref.[Yu et al., 2011] are also present in our phase diagram. For instance, the AF4 state (Fig. 5.2(b)) is stable in a large region of parameter space at small values of J/U. Thus, overall our results support a combination of the main conclusions of Refs.[Yu et al., 2011; Yin et al., 2012].

The density-of-state (DOS) for the AF1 phase is shown in Fig. 5.3 for representative couplings. The presence of a gap at the chemical potential indicates an insulating state, in agreement with experiments [Bao et al. (2011)]. This is not surprising considering that the transport of charge from each 2×2 building block to a NN block may be suppressed due to the effective antiferromagnetic coupling between blocks, at least at large U and J. In other words, using a tilted square lattice made out of 2×2 superspin blocks, the state is actually a staggered antiferromagnet that is known to have low conductance. On the other hand, it is interesting to observe that the AF1 gap is only weakly dependent on U, suggesting that not only the increase in U is responsible for the insulating behavior but there must be other geometrical reasons that may contribute to the gap through quantum interference. This is reminiscent of results reported years ago for the insulating CE phase of half-doped manganites, state that is stabilized in the phase diagram even in the absence of electron-phonon coupling due to the peculiar geometry of the zigzag chains involved in the CE state and the multi-orbital nature of the problem, that induces a band insulating behavior [Hotta et al. (2000)]. Thus, in agreement with recent independent observations [Yin et al. (2012)], our results suggest that the insulator stabilized in the presence of Fe vacancies may have a dual Mott and band-insulating character. Note also that the competing C-state only has a pseudogap (Fig. 5.3), and thus it may be a bad metal.

With regards to the strength of the FM tendencies in each of the 2×2 building blocks of the AF1 state, examples of the values of the magnetic moment m (in Bohr magnetons, assuming g=2, and at J/U=0.25) are m=3.87 (U=3.0), m=3.93 (U=4.0), and m=3.95 (U=5.0), in good agreement with neutron diffraction results m=3.3 [Bao et al. (2011)]. Thus, the Fe spins in the AF1 superblocks are near the saturation

value 4.0 μ_B at n=6.0. Note that the competing C-phase also has a surprisingly large moment m=3.5 at U=2.0 and J/U=0.25.

Chapter 6

Magnetic states of the two-leg-ladder alkali metal iron selenides AFe_2Se_3

6.1 Introduction

A recent fascinating new discovery in the iron-based superconductors [Johnston (2010); Dai and Dagotto (2012); Dagotto (2013)] is the report of superconductivity in the intercalated iron selenides $K_{0.8}Fe_{2-x}Se_2$ and (Tl,K)$Fe_{2-x}Se_2$ [Guo et al. (2010)]. Further investigation of iron chalcogenides could be made if the iron spins are arranged differently than in the nearly square lattice geometry of the FeSe layers. Recently, considerable interest was generated by the studies [Svitlyk et al. (2013); Caron et al. (2011); Lei et al. (2011); Saparov et al. (2011); Caron et al. (2012); Nambu et al. (2012)] of $BaFe_2Se_3$ (the "123" compound) since this material contains chains made of $[Fe_2Se_3]^{2-}$ building blocks separated by Ba. These effective two-leg iron ladders in $BaFe_2Se_3$ are cut-outs of the layers of edge-sharing $FeSe_4$ tetrahedra normally found in layered chalcogenides. A recent remarkable development that increases the relevance of the iron-based ladders is the following. The preparation of a single

layer of alkali-doped FeSe with the geometry of weakly coupled two-leg ladders was recently reported in Ref. [Wei Li (2012a)], where it was also argued that this ladder system is superconducting based on the presence of a gap in the local density of states. These results suggest that Fe-based ladders provide a simple playground where even superconductivity can be explored, increasing the similarities with the Cu-oxide ladders that are also superconducting [Dagotto (1999)].

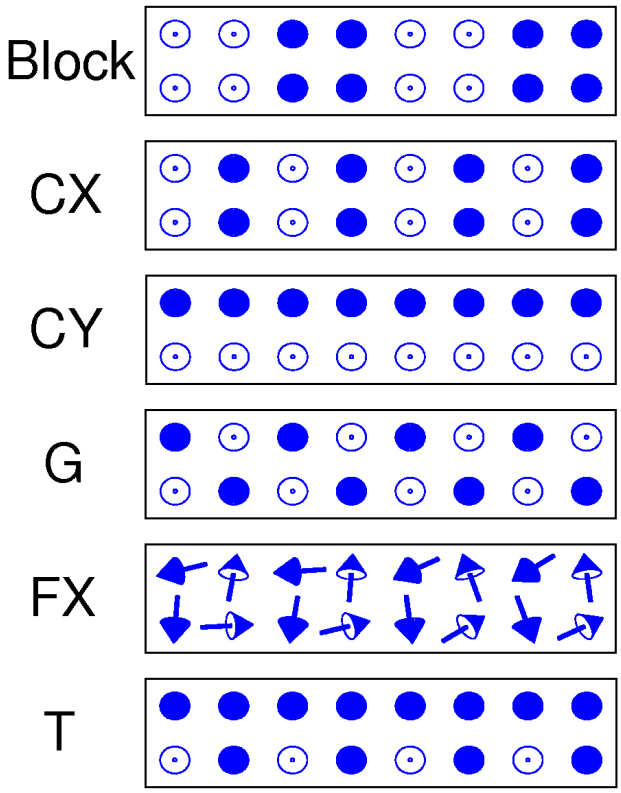

Figure 6.1: Magnetic states observed in the phase diagrams of the multiorbital Hubbard models used in this study, employing the geometry of a two-leg ladder.

In this chapter, results for multiorbital Hubbard models are reported. The lattice distortions [Caron et al. (2011); Lei et al. (2011)] are partially taken into account via the hopping amplitudes, as described below. However, part of our results presented in the following sections show that even without lattice distortions the 2×2 block-AFM state is stable in regions of the phase diagrams that are constructed by varying the on-site Hubbard repulsion U, the Hund coupling $J_{\rm H}$, and the electronic density n [Wei Li

(2012b)]. In other words, our most important result is that several models, studied with several approximations, systematically contain the block-AFM state as a robust phase in the phase diagram. Moreover, the other recently observed [Caron et al. (2012)] CX-state is also found in the resulting phase diagrams. Several competing states that could be stabilized in related compounds or under pressure or via chemical doping are also discussed.

The present study is carried out mainly using the real-space Hartree-Fock approximation for the five-orbital Hubbard model, employing both a set of hopping amplitudes that are deduced from first principles techniques applied to the selenide 123 ladders, as explained below, and also an "old" set of hopping that was previously employed in layered pnictides [Graser et al. (2009)]. The purpose of using two sets of hoppings is to gauge how sensitive the results are with regards to modifications in those hopping amplitudes. In addition, our results for pnictide hoppings can be considered predictions in case two-leg ladder pnictides are synthesized in the future.

6.2 Five-orbital Hubbard model, Hartree-Fock approximation, and Hopping amplitudes

The five-orbital Hubbard model and Hartree-Fock approximation used in this chapter have all been extensively discussed in Chapter 2. In this section, the focus will be on the derivation of the hopping amplitudes (refereed to as the selenide hoppings in the rest of this chapter) needed for the five-orbital Hubbard model, from first-principles techniques, as explained below. The selenides hopping amplitudes for the 123 ladders were obtained via a first-principles density functional theory calculation of the non-magnetic normal state. The calculation was conducted using the WIEN2K implementation of the full potential linearized augmented plane wave method in the local density approximation [Schwarz et al. (2002)]. The k-point mesh was taken to be $7\times15\times19$. The lattice constants were taken from Ref.[Caron et al. (2011)].

Table 6 in Appendix B shows the hopping parameters calculated by representing the resulting self-consistent Kohn-Sham Hamiltonian with low-energy ([-2.5, 2] eV) symmetry-respecting Wannier functions [Ku et al. (2002)] with strong Fe-d symmetry. Since the influence of the As-p orbitals are integrated into the tail of the Wannier functions, the parameters correspond to an effective iron-only model with five orbitals per iron. The staggered location of the selenium atoms, above and below the plane defined by the Fe atoms, is taken into account in the calculation. For a similar discussion in the context of the three orbital model, see Ref.[Daghofer et al. (2010b)]. Table 6 in Appendix B contains the hoppings that are needed for the full description of the system, based on the iron locations in Fig.6.2. Note that each 5×5 matrix in Table 6 should be considered as the hopping matrix to move from one iron to another as indicated. For a given Fe-Fe bond, the full matrix that includes both the back and forth processes for the hopping is of size 10×10 and it consist of a 5×5 matrix of this table in a non-diagonal block, the transpose in the other nondiagonal 5×5 block, and the on-site matrix (top of this table) in both diagonal blocks. Other hoppings are all identical to one of those shown in Table 6. For instance, the hopping matrix from Fe2 to Fe7 is the same as the hopping matrix from Fe1 to Fe8 in Table I, the hopping matrix from Fe1 to Fe7 is the same as the hopping matrix from Fe2 to Fe8, etc.

For completeness, results using the hoppings corresponding to layered pnictides [Graser et al. (2009)] will also be used, and the results compared with one another. While the data gathered with the realistic selenide hoppings are our most important set of results, contrary to naive expectations it will be shown that a reasonable agreement is observed between these two "a priori" quite different sets of hopping amplitudes, at least at a qualitative level. The electronic density of main interest is, in principle, $n \sim 6.0$ (i.e. 6 electrons/Fe), thus our efforts are centered at this density, but some results varying n are shown as well (or verbally described). As explained in previous chapters, the on-site intraorbital Hubbard repulsion is U, the Hund coupling is $J_{\rm H}$, and the interorbital repulsion U' is assumed to satisfy U'=U-2$J_{\rm H}$. Ladders of

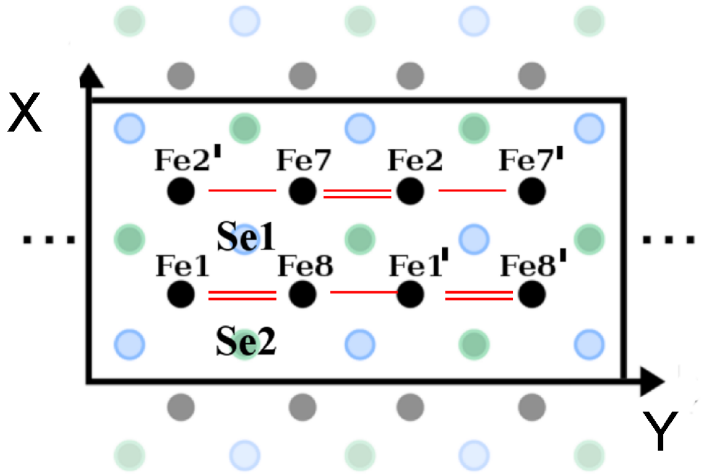

Figure 6.2: Label convention of the iron sites used in Table I, adapted from Fig. 1(b) of Ref.[Caron et al. (2011)]. The single and double lines along the y axis denote two different lattice spacings, with specific numbers taken from Ref.[Caron et al. (2011)]. The two selenium sites denote locations above and below the plane defined by the iron ladder.

sizes $2\times L$ (L=4, 8, 16, 32) were studied, and size effects were found to be mild. Periodic (open) boundary conditions are used along the chain (rung) direction.

6.3 Results for the five-orbital Hubbard model

6.3.1 Phase diagrams and the block-AFM phase

The main results of this chapter are shown in Fig. 6.3, where the phase diagrams varying U/W and $J_{\rm H}/U$ are presented using both the realistic selenides hoppings for the 123 ladders as well as the pnictides hoppings for comparison. The bandwidth W of the five-orbital Hubbard model is ∼2.8 eV for the selenides hoppings, while for the pnictides hoppings it is ∼4.8 eV [Graser et al. (2009)]. In all cases, Figs. 6.3(a-c) show the remarkable result that the block-AFM phase found in neutron experiments for the 123 ladders [Caron et al. (2011); Nambu et al. (2012)] becomes stable in a robust region of the phase diagram. This is interesting since the 2×2 blocks in ladders are not as clearly geometrically defined as in the $\sqrt{5}\times\sqrt{5}$ iron-vacancies arrangements, where each of the plaquettes of the tilted square lattice of those iron vacancies already contains a 2×2 block inside. In our two-leg ladders, on the other hand, the ferromagnetic (FM) blocks do emerge spontaneously in the calculations described here and in experiments as well. As explained before, the present results were confirmed using unbiased random starting configurations for the HF expectation values and an iterative procedure for convergence. By this procedure, the stability of the block-AFM state was indeed tested at several points of the phase diagram. Moreover, it is interesting that the region of stability includes the realistic ratio $J_{\rm H}/U = 0.25$, found before to correspond to the "physical region" where a good agreement theory-experiment was observed for the pnictides [Luo et al. (2010); Yu et al. (2009)].

With regards to the actual value of U/W, note that the block-AFM phase is stabilized starting at $U/W \sim 0.5-0.6$ for the selenides hoppings [Figs. 6.3(a,b)] and

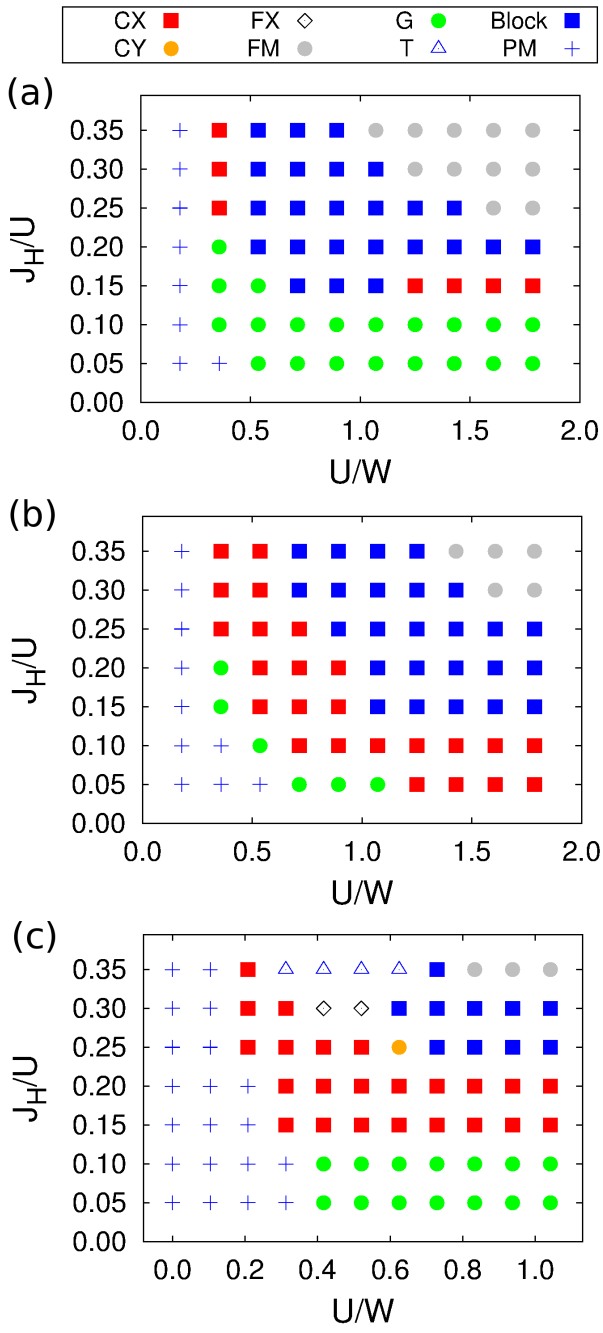

Figure 6.3: Phase diagram of the five-orbital Hubbard model in the real-space HF approximation. The label convention for the phases is in the upper inset and also in Fig. 6.1. PM denotes a paramagnetic state. (a) Results for a 2×16 cluster, using the selenides hopping amplitudes for the 123 ladders, and at electronic density $n = 6.0$. (b) Same as (a) but for electronic density $n = 5.75$. (c) Results for a 2×32 cluster, using the pnictides hopping amplitudes, and working at electronic density $n = 6.0$.

at $U/W \sim 0.6$ for the pnictide hoppings [Fig. 6.3(c)]. This is similar to the value $\sim$0.52 reported for $K_{0.8}Fe_{1.6}Se_2$ in Ref.[Luo et al. (2011)] using similar techniques. The critical U/W's quoted above are slightly larger than the $U/W \sim 0.31$ needed for the pnictides in the planar geometry of the "1111" and "122" materials to form the C-type AFM state [Luo et al. (2010); Yu et al. (2009)], but note that in our present results magnetic order in the CX channel (the analog of the C-type AFM phase) is reached at $U/W \sim 0.3$ in good agreement with those previous investigations. Considering that it is the block-AFM state that is found experimentally for the 123-ladder selenides, this suggest that these selenides are more strongly correlated than pnictides and their ratios of U/W are roughly $0.5/0.3 = 1.66$. Note also that the actual values of U/W are still smaller than 1, the ratio often considered as the boundary of the strong coupling limit, implying that the selenide ladders are still "intermediate" coupling compounds [Dai and Dagotto (2012)]. However, the HF approximation favors ordered states, and including quantum fluctuations the U/W needed to stabilize the block-AFM phase may exceed 1. On the other hand, note also that results in real ladders may be influenced by the presence of a robust electron-lattice coupling (mentioned in Refs.[Caron et al. (2011); Lei et al. (2011)]) that may render stable the block-AFM phase even at values of U/W not as large as needed for its stabilization when based entirely on an electronic mechanism. In spite of these caveats, it is clear that even with lattice distortions incorporated the presence of sizable electronic correlations appears to be important to stabilize the block-AFM state.

In the block-AFM phase found in our study the magnetic moment per Fe is large and close to saturation. More specifically, it is $\sim$4.0 μ_B for the selenides hoppings and $\sim$3.9 μ_B for the pnictides hoppings, with small variations caused by the selection of specific values of U. The difference with the experimental result [Caron et al. (2011)] $\sim$2.8 μ_B may be caused by the absence of fluctuations in the HF approximation [Zhang et al. (2012)], or by the neglect of lattice distortions in our effort, as already discussed. But at least qualitatively the large value of the magnetic moment, as

compared with the relatively small moments reported in some layered pnictides, is here properly reproduced.

In this chapter, square 8×8 clusters have also been studied to address the coupling between ladders in the direction perpendicular to the legs. In practice, a weak interladder coupling was introduced by multiplying by a small factor α=0.1 all the hoppings connecting sites belonging to different individual 2×8 ladders (thus the 8×8 cluster has four of these two-leg ladders). Other values of (small) α were used and the results were all similar. The main result (not shown) is that the phase diagrams using the 8×8 clusters are virtually identical to those found for the individual two-leg ladders, for both sets of hoppings, with the only interesting detail that the weak coupling between the ladders establishes an effective antiferromagnetic coupling between them, as found experimentally [Caron et al. (2011)].

6.3.2 The CX phase and other competing states

It is important to remark that in all Figs.6.3 (a-c) there are several other magnetic states in addition to the block-AFM state. In particular, the "CX" phase found experimentally in hole-doped ladders [Caron et al. (2012)] also occupies a robust region of the phase diagram, and it is located next to the block-AFM phase for both the selenides 123-ladder hoppings as well as the pnictide hoppings, at the electronic densities investigated in Fig.6.3. Its region of stability includes areas with smaller or similar values for U/W than those where the block-AFM state is stable. Our investigations varying n reveal that this phase is stable in a broad region of parameter space, including the $n = 5.5$ electronic density corresponding to KFe_2Se_3 [Caron et al. (2012)] indicating once again a good agreement between calculations and experiments. In fact, Fig.6.3 (b) shows that the CX state is more stable at electronic density n=5.75 than at n=6.0, compatible with experiments. The CX state can be considered closely related to the C-AFM state of layered pnictides with the wavevector (π,0), thus its stability particularly close to the PM state should not be too surprising.

Varying U/W and $J_{\rm H}/U$, phases that have not been observed experimentally for the two-leg ladders become stable. For instance, when the Hund coupling is small compared with U, a G-type antiferromagnetic state is found, with staggered magnetic order. In the other extreme of magnetic order, ferromagnetism is observed in a small region of parameter space for a sufficiently large U and Hund couplings, for both sets of hoppings. The qualitative tendency from "G" to "CX" to "block-AFM" to "FM" with increasing $J_{\rm H}/U$ at robust U/W goes together with the tendency to FM order in the vicinity of each iron atom: for the G-state the three NN links are AFM, for the CX-state two are AFM and one is FM, for the block-AFM state two are FM and one AFM, and of course for the full FM state all NN links are FM.

Small "islands" of other states are also present in the phase diagram corresponding to the pnictides hoppings, including the CY-state which is another relative of the C-AFM state of the pnictides, as well as the Flux and T states (see Fig.6.1 for the spin arrangement corresponding to these states). But it is clear that the block-AFM, CX, G, FM, and PM states dominate the phase diagrams.

6.3.3 Density of States

The density of states (DOS) of the block-AFM state for both the cases of the "selenides" 123-ladder hoppings and the "pnictides" hoppings are shown in Fig.6.4 for representative couplings. The presence of a gap at the chemical potential for the block-AFM state and for both hoppings indicates an insulating state, in agreement with experiments. While the values of the gap for the block-AFM state ($\Delta\sim$0.40 eV and $\Delta\sim$0.45 eV for the selenides and pnictides hoppings, respectively) are larger than reported experimentally [Nambu et al. (2012); Lei et al. (2011)], the qualitative trends are correct. Further improvement with experiments can be achieved by better fine tuning U/W and $J_{\rm H}/U$, by adding effects arising from the three dimensionality of the problem, incorporating other lattice distortions, etc.

Another detail that merits a comment is that the CX phase, being closer in the phase diagrams to the PM state than the block-AFM state is, has a metallic or weakly insulating character that depends on specific details such as the value of U/W. At a fixed J_{H}/U such as 0.25, the metal-insulator transition seems to occur within the CX phase.

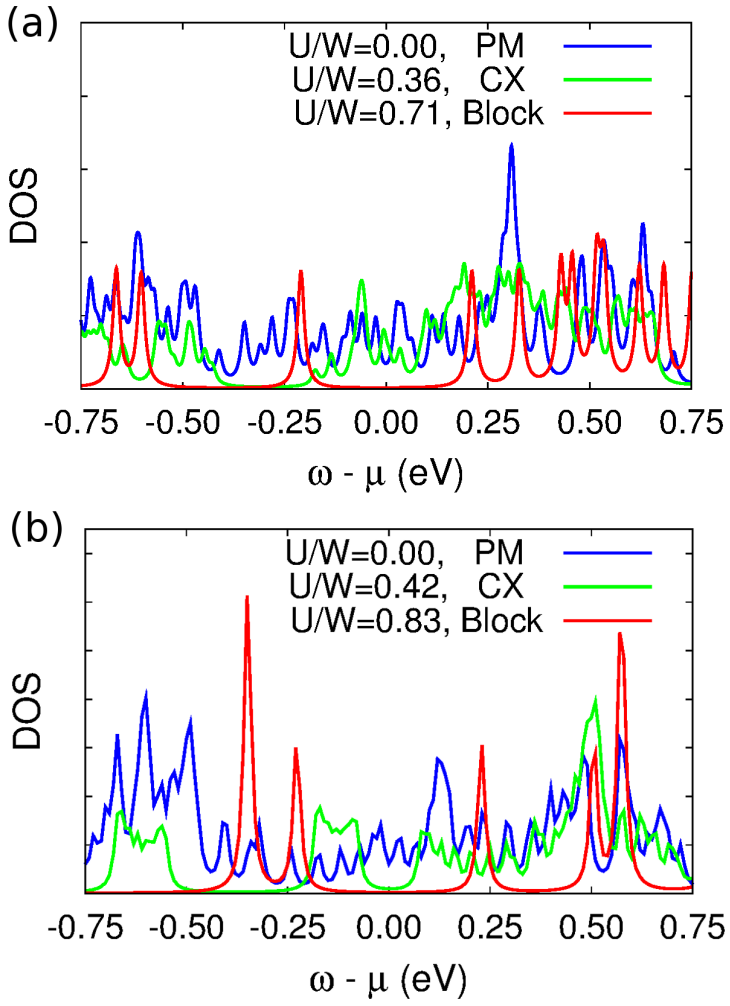

Figure 6.4: Density of states of the five-orbital Hubbard model (in the HF approximation), at $J_{\rm H}/U = 0.25$, and the values of U/W indicated. The type of phase state corresponding to each value of U/W is also indicated. (a) corresponds to the selenides hoppings for the 123-ladder compound and electronic density $n = 6.0$. The bandwidth W in this case is $\sim$2.8 eV. (b) corresponds to the pnictides hoppings, for comparison. The electronic density is $n = 6.0$, and the bandwidth W is $\sim$4.8 eV. In both cases, the small oscillations at $U/W = 0$ and in the CX phase are caused by size effects in the long direction of the 2×16 or 2×32 clusters used and the intrinsic small size in the rung direction.

Chapter 7

Magnetic Phase Diagram of a Five-Orbital Hubbard Model in the Real-Space Hartree Fock Approximation Varying the Electronic Density

7.1 Introduction

Early theoretical studies of iron-based high T_c superconductors suggested a relatively simple picture of the magnetic and superconducting properties as arising from weak-coupling Fermi surface nesting effects. However, recent experimental and theoretical studies have unveiled a variety of compounds and chemical compositions that display a more complex physics where intermediate-range electronic repulsion effects cannot be neglected [Dai and Dagotto (2012)]. In particular, there are materials with no Fermi surface nesting that nevertheless become superconducting, and there are compounds with a very large magnetic moment in the ground state that do not fit into the weak

coupling picture [Dagotto (2013)]. Moreover, at room temperature clear indications of local magnetic moments exist [Gretarsson et al. (2011); Bondino et al. (2008)], incompatible with weak coupling scenarios where the formation of moments and the long-range order develop simultaneously upon cooling. For these reasons, a more serious consideration of the effects of the Hubbard on-site repulsion U and on-site Hund coupling J is needed. While this task is in principle difficult due to the scarcity of unbiased many-body techniques that can handle a multiorbital Hubbard model, the use of mean-field approximations can at least unveil qualitative tendencies in phase diagrams and the characteristics of the dominant states.

The interesting recent studies, which replace entirely Fe by another $3d$ transition element such as Mn or Co, motivate the present model Hamiltonian investigations, where the electronic density per transition metal atom n is allowed to vary over a wide range, centered at the n=6 value corresponding to pnictides and selenides where the ground state is a C-type antiferromagnet. In previous efforts, the G-type AFM state at n=5 was already reported [Calderón et al. (2012); Bascones et al. (2012)]. Other investigations assign a crucial role to the n=5 G-type AFM state to understand the physics of the n=6 limit [Misawa et al. (2012)]. In some studies the superconducting state of pnictides is visualized as emerging from the n=5 G-type insulator [Luca de' Medici (2012)] as opposed to being induced from the C-type antiferromagnetic metal of n=6. All these previous efforts provide additional motivation for our studies in this section. Thus, drastically altering the electronic concentration far away from n=6 may lead to interesting perspectives to understand the pnictide and selenide superconductors.

7.2 Model and Method

In this chapter, a five-orbital Hubbard model, which is exclusively based on electrons that are located in the Fe $3d$ orbitals, will be used, with emphasis on the magnetic states that are obtained by varying couplings and the electronic density

n. Superconducting tendencies will not be investigated here. With regards to the tight-binding parameters, the set of hoppings used in the present effort is taken from Ref. [Graser et al. (2009)], which provides a Fermi surface that compares well with experiments and band structure calculations for the pnictides. The overall conclusions of our study are sufficiently generic that they are likely to be valid even if other set of hoppings are used, although certainly the details and actual critical couplings will change from set to set. The approximate bandwidth W of the tight-binding hopping term is 4.7 eV, and the ratio U/W should be used to judge whether the phases of interest are or not, e.g., in the strong coupling regime where $U/W \sim 1$. A ratio $U/W \sim 0.5$ is more typical for the location of the experimentally relevant phases based on previous Hartree Fock investigations [Dai and Dagotto (2012); Luo et al. (2010)], signaling an intermediate coupling regime. However, note that the quantum fluctuations not considered in mean-field studies will tend to increase the critical values of U/W.

To study the ground state properties of the multiorbital Hubbard model, the real-space Hartree Fock (HF) approximation will be applied to the Coulombic interaction, which is discussed in Chapter 2. All the numerical results are obtained using a real-space 8×8 square lattice with periodic boundary conditions.

7.3 Main Results

7.3.1 Phase Diagram

The effort described in this chapter was computationally intense, since there were two parameters to change (U and n; J/U was fixed to 0.25, a value considered realistic from Chapter 3) and the real-space HF process is typically characterized by a slow convergence in the iterative process. The main result of this study is summarized in the HF phase diagram of the five-orbital Hubbard model, varying the on-site coupling

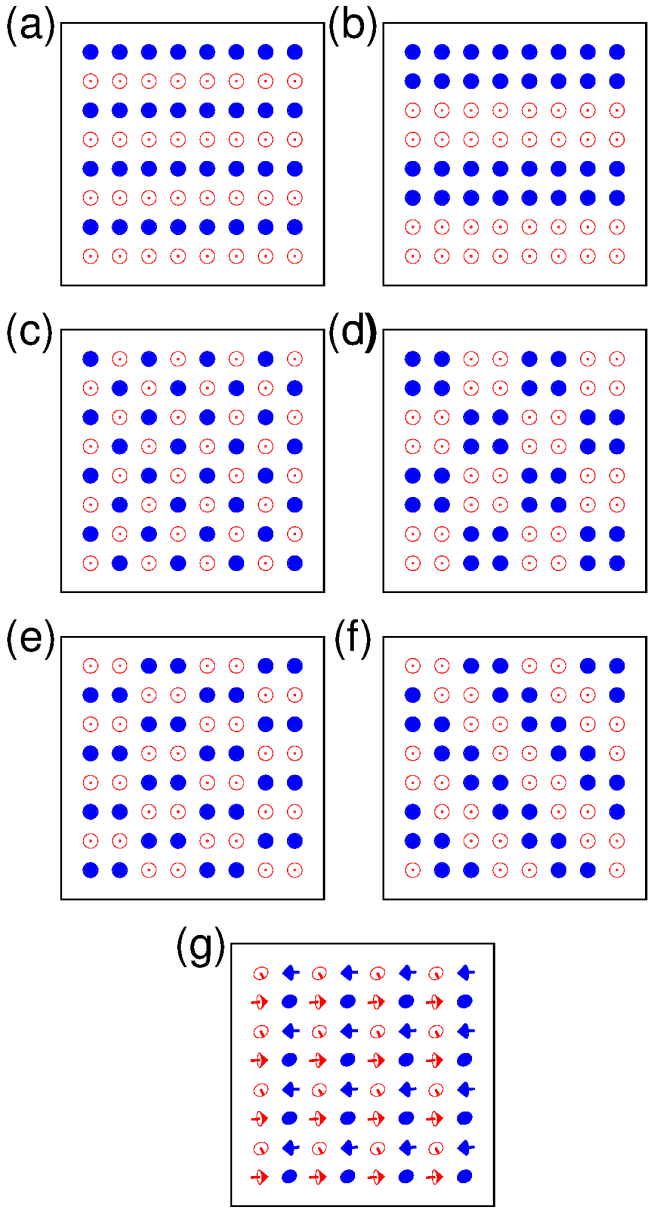

Figure 7.1: Magnetic states observed in the phase diagram of the five-orbital Hubbard model used in this study, treated in the HF approximation. These magnetic states are named as: (a) C, (b) DC, (c) G, (d) Block, (e) GC, (f) E, and (g) Flux.

U and electron density n, shown in Fig.7.2. In Fig.7.1 the reader can find the set of relevant states that appeared in this phase diagram.

Let us now describe in detail the results. Starting at $n = 5$, i.e. 5 electrons for the five $3d$ transition metal orbitals, the state has a strong tendency to form a G-type AFM state. This is to be expected given the electronic population, and this result is in excellent agreement with experiments for $BaMn_2As_2$ [Singh et al. (2009)] and with previous theoretical efforts [Calderón et al. (2012); Misawa et al. (2012); Luca de' Medici (2012)]. The robustness of the G-AFM state suggests that using other hoppings amplitudes, such as those more quantitatively adequate to describe $BaMn_2As_2$, will likely lead to similar conclusions.

The G-AFM state has individual spins that are antiferromagnetically coupled to their four neighbors. As n increases, growing tendencies toward developing more ferromagnetic links are observed. In fact, the novel "GC" state (see Fig.7.1) is stabilized next when increasing n away from 5, and this state has three AFM links and one FM link. This state can be considered as a combination of the G-AFM and C-AFM states, thus the notation GC. Its dominant wave vector is $(\pi/2,\pi)$, and the state breaks rotational invariance between the two axes x and y, as the C-AFM states does, but also has a staggered ordered as the G-AFM state does, although involving 2×1 blocks. Thus, with hindsight it is not surprising to find this GC state stabilized in between the G and C states. A somewhat surprising result is that the area of stability of the GC state also includes a region of weak U coupling at $n = 6$ where it is widely believed that the C-type AFM state should dominate. This C-AFM state indeed is stable increasing U but not at very weak coupling. Considering that recent Monte Carlo computational studies including lattice distortions and using three orbitals in the context of a spin-fermion model do favor the C-AFM state [Liang et al. (2012, 2013)], then probably the absence of lattice degrees of freedom in the present effort may lead to a spurious larger region of stability of the GC state that includes portions of the $n = 6$ axis. Thus, readers should be warned that the region of true stability of the GC-AFM state may be smaller than the HF approximation

suggests, particularly after lattice effects and quantum fluctuations are incorporated. In general, only qualitative trends are expected to be robust in the present study but not detailed quantitative aspects. The prediction arising from this effort is that it would not be surprising to find the GC state stabilized in materials where the relevant electronic density is approximately n=5.5.

As already mentioned, centered at $n = 6$ and for intermediate and large U the C-AFM state is stabilized, in agreement with many experiments and several other theoretical studies [Johnston (2010); Dai and Dagotto (2012); Dagotto (2013)]. Since this state has been widely discussed before in many contexts, there is no need to repeat those discussions and the focus here now shifts to values of n larger than 6. In this regime, several exotic states are stabilized in the HF approximation. One of these novel states is the "Flux" state, shown in Fig.7.1(g). Note that this state is not collinear. A similar state has been discussed before in the context of two-orbital Hubbard models [Lorenzana et al. (2008)], and in small regions of the phase diagram of a five-orbital Hubbard model defined on two-leg ladders [Luo et al. (2013)] To our knowledge this Flux state has not appeared in previous studies when using two-dimensional geometries and five-orbital models, and it has not been observed experimentally yet.

Another exotic and novel state stabilized at n larger than 6 is the double-C, "DC", state shown in Fig.7.1(b). The notation double C is in reference to the doubled period in one direction with respect to the well-known C-state. This DC state has a spin structure factor peaked at $(0,\pi/2)$ or $(\pi/2,0)$ depending on the lattice instabilities that may appear in a real system. This DC state is representative of the previously-mentioned growing ferromagnetic tendencies with increasing n since each spin has three (one) ferromagnetically (antiferromagnetically) aligned neighbors. It is conceivable that with further increasing n and/or U and J, a fully ferromagnetic state can be stabilized, as already observed in previous HF approximation studies in other chapters, such as Chapter 5 and Chapter 6. Note also that from our results near n=7 (Fig.7.2) there are no indications that the C-type AFM state can become

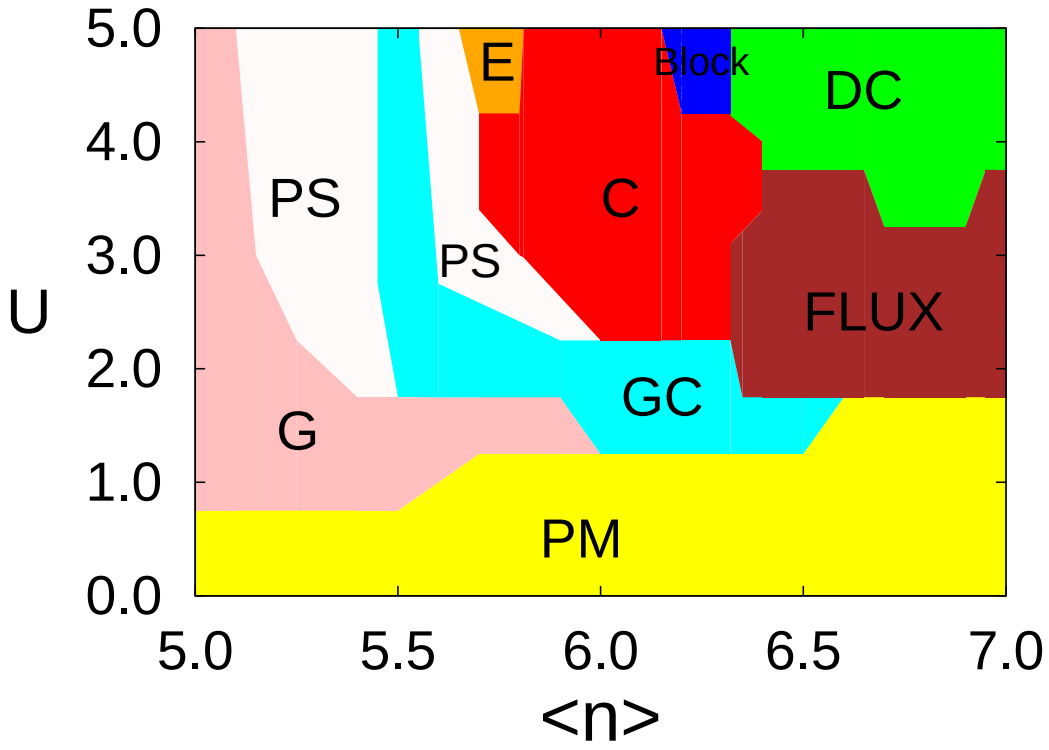

Figure 7.2: Phase diagram of the five-orbital Hubbard model varying the on-site same-orbital repulsion U and the electronic density n (number of electrons per transition metal site). The Hund coupling was fixed to $J/U = 0.25$. The notation for the many states was explained in Fig.7.1. Light pink areas correspond to "Phase Separation" (PS) regions where the energy vs. n curves have a negative curvature (as described later in this chapter). In practice, at least a vestige of magnetic order is typically found in the numerical process even for very small values of U. However, previous experience indicates that this is likely a "Paramagnetic" (PM) state since it is smoothly connected to the $U = 0$ limit. Thus, in practice the PM state is defined as the state where the order parameter m, of any kind, is smaller than a cutoff chosen as 4% of the saturated value for the same state at other densities or couplings. Since the order parameters often raise steeply at the critical U that separates the PM from magnetic states, then selecting other cutoffs give similar results. Note also that the bandwidth W of the hopping term is 4.7 eV.

stable at such large electronic densities, at least at the level of ground states. Thus, the recent inelastic neutron scattering results [Jayasekara et al. (2013)] for $SrCo_2As_2$ reporting C-type fluctuations remain paradoxical, and deserve further studies.

In addition to the dominant G, GC, C, Flux, and DC states, there are two small regions where two exotic states, the E and Block states, are stabilized. These states need a robust U to become stable (i.e. $U/W \sim 1$ is needed for their stability) and they have been mentioned in other contexts before. For instance, the Block-AFM state is made of 2×2 FM blocks that are coupled antiferromagnetically. This state was proposed to be the ground state of KFe_2Se_2 in previous theoretical investigations [Li et al. (2012)]. A similar "Block" structure has been unveiled experimentally and theoretically in materials with iron vacancies [Dagotto (2013); Luo et al. (2011)] and also in selenides with two-leg ladder geometries [Luo et al. (2013)]. These Block states have individual spins with two antiferromagnetic links and two ferromagnetic links, thus their location next to the C-AFM state is reasonable since they share this same property. This line of reasoning is mainly of relevance for discussions involving localized spins, as they occur at robust U. It is gratifying that the Block-AFM appears spontaneously in our calculations without the need of introducing lattice distortions.

The other exotic state stabilized in a small region at robust U/W is the "E" state shown in Fig.7.1(f). This state has a peak in the spin structure factor located at $(\pi/2,\pi/2)$, which is compatible with experimental neutron scattering results for FeTe [Li et al. (2009)]. Historically, the E phase was reported initially in investigations of manganites [Hotta et al. (2003)]. The existence of the E phase is also compatible with more recent theoretical studies that used the spin-fermion model, involving a mixture of localized and itinerant degrees of freedom with two active orbitals [Yin et al. (2010)]. The E state was also reported by another group in previous investigations of a five-orbital Hubbard model, using momentum-space mean-field and Heisenberg techniques, and a different set of hopping amplitudes [Calderón et al. (2012)], where the E-state is actually called the DS-state. Here, the historical notation that started with the manganites is used and the state is called E. Note also that

recent investigations suggest ferro-orbital order and a bond-order wave in $Fe_{1.09}Te$ in the regime of the E-phase [Fobes et al. (2013)], implying that the region where the E-state is here reported to be stable should deserve further more detailed studies.

In summary, the four states G, C, E, and Block have been observed before in different materials of the family of iron-based superconductors and in other theoretical studies, while the possible stability of the three states GC, Flux, and DC are original predictions of the present study. Note that the mean-field approximation used here tends to exaggerate the presence of magnetic order. While the predictions are expected to be reasonable at special density fractions such as n=5, 5.5, 6, ..., the phase diagram unveiled here at intermediate values of n is at best indicative of qualitative tendencies that may exist, perhaps, only in the form of short-range correlations. Also note that superconducting states have not been proposed in this mean-field study, so the focus is only on magnetic order (and its concomitant orbital order, as described below).

7.3.2 Magnetic Order Parameters

In Table 7.1, characteristic magnetic moments of the seven phases found in Fig.7.2 are provided at representative couplings and densities. The values shown tend to indicate a robust magnetic moment. However, in the phases that are in contact with the weak coupling PM state in the phase diagram (i.e. the G, GC, and Flux states), there is a region of rapid change in the value of the magnetic moment when magnetism develops, as shown in Fig.7.3 and 7.4. Thus, values of the magnetic moments weaker than those in Table 7.1 are also possible for some of the phases.

In Fig.7.3, the order parameter at $n = 6$ is explicitly shown, varying U. While the C-AFM state that is stabilized at intermediate and large U is to be expected, the presence of the GC-AFM state in the weak coupling regime is a surprise, as already discussed. In view of the many approximations involved in arriving to this state, it would be premature to claim that the GC-state should be stable in portions of

Table 7.1: Magnetic moments of the seven competing states at selected couplings and densities. The details are as follows: C-state (U=3.0, n=6.0); Flux-state (U=3.0, n=6.5); G-state (U=3.0, n=5.0); GC-state (U=3.0, n=5.5); E-state (U=5.0, n=5.75); Block-state (U=5.0, n=6.25); DC-state (U=5.0, n=6.75). The phases with $*$ indicates that the magnetic moment is not the same at each site. Typically, there are four sites that repeat themselves in most of the cases, but sometimes the periodicity involves two sites or eight sites. The numbers used for these states in the present table are their average values.

	xz	yz	x^2-y^2	xy	z^2	total
C	0.9235	0.5426	0.5678	0.9499	0.7451	3.7289
Flux*	0.6094	0.6735	0.4812	0.8372	0.5693	3.1692
G	0.9475	0.9475	0.9242	0.9609	0.9682	4.7481
GC	0.9362	0.7853	0.7027	0.9540	0.8625	4.2407
E*	0.8589	0.8602	0.6063	0.9843	0.8702	4.1799
Block	0.8296	0.8296	0.6559	0.9573	0.3944	3.6667
DC	0.7632	0.6043	0.5470	0.9102	0.3611	3.1858

the phase diagram corresponding to the Fe-based compounds, but its presence in the phase diagram can be considered as indicative of a competition between many magnetic states. In practice, other degrees of freedom, such as the lattice, are probably crucial in deciding which state is the most stable in an actual compound.

Similar results were obtained at other electronic densities, as shown in Fig.7.4. At $n = 5$, the G-AFM state is clearly dominant, with an order parameter (in units of the Bohr magneton) that tends to the maximum value 5 as U grows. At the other electronic densities shown, there is always phase competition between two or three states, and this phase competition may preclude the order parameters from reaching their maximum value, at least in the range studied. The transitions between different magnetic states are of first order but the jumps in the order parameters tend to be rather small and in some cases the curves look almost continuous.

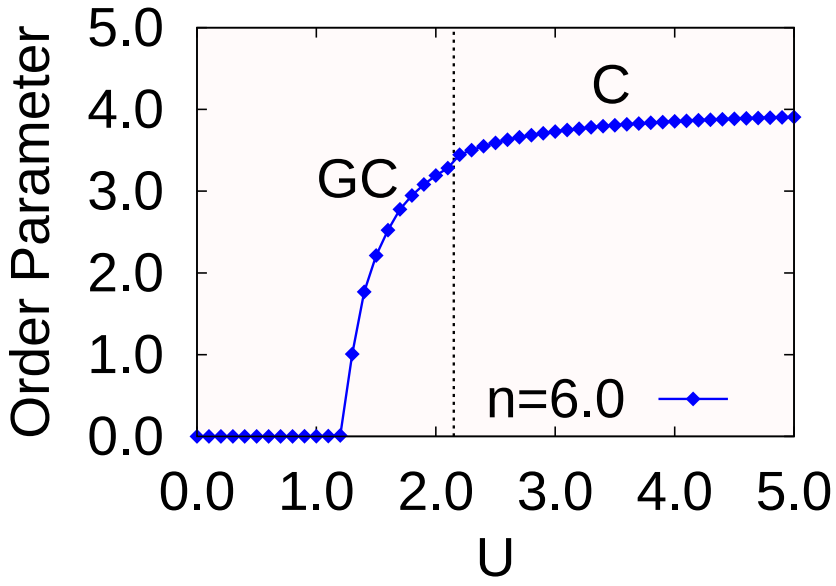

Figure 7.3: Hartree Fock order parameters (Bohr magneton units) vs. U at density $n = 6.0$ and $J/U = 0.25$. The magnetic states GC and C have been presented in Fig.7.1. The bandwidth W is 4.7 eV.

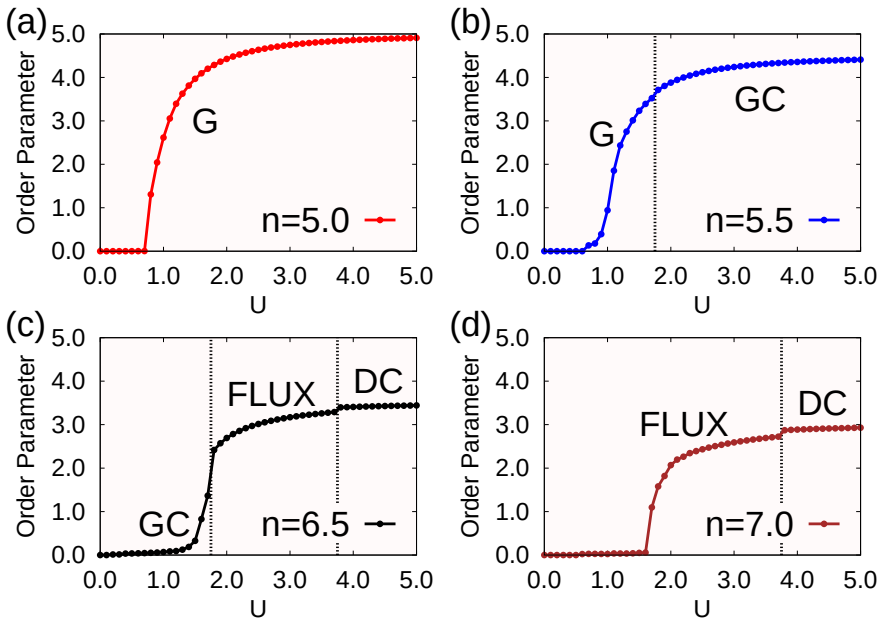

Figure 7.4: Hartree Fock order parameters (Bohr magneton units) vs. U at $J/U = 0.25$ and several electronic densities: (a) $n = 5.0$; (b) $n = 5.5$; (c) $n = 6.5$; (d) $n = 7.0$. All the states indicated are shown explicitly in Fig.7.1.

7.3.3 Orbital Composition

The orbital compositions of the seven states unveiled in the phase diagram of Fig.7.2 are given in Table 7.2. From the perspective of these occupations, the G-AFM state has clear indications of being an insulator since all the five orbitals are approximately equally populated with one electron per orbital. On the other hand, most of the orbitals of the other six states have a population substantially different from one, potentially giving rise to a metallic state (perhaps with coexisting itinerant and localized degrees of freedom). However, the Block-AFM state should be insulating due to the peculiar spin geometry of the state that renders difficult for electrons to transition from block to block while keeping the same spin orientation.

Table 7.2: Orbital compositions of the seven competing states at selected couplings and densities. The details are as follows: C-state (U=3.0, n=6.0); Flux-state (U=3.0, n=6.5); G-state (U=3.0, n=5.0); GC-state (U=3.0, n=5.5); E-state (U=5.0, n=5.75); Block-state (U=5.0, n=6.25); DC-state (U=5.0, n=6.75). Similarly as in Table 7.1, the phases with $*$ indicates that the orbital population is not the same at each site. Typically, there are four sites that repeat themselves in most of the cases, but sometimes the periodicity involves two sites or eight sites. The numbers used for these states in the present table are their average values.

	xz	yz	x^2-y^2	xy	z^2	total
C	1.0048	1.3911	1.3659	1.0099	1.2281	6.0
Flux*	1.3083	1.2435	1.4462	1.1108	1.3912	6.5
G	0.9998	0.9998	1.0029	0.9965	1.0009	5.0
GC	1.0017	1.1606	1.2269	1.0025	1.1083	5.5
E*	1.1249	1.1236	1.3758	1.0046	1.1212	5.75
Block	1.1509	1.1509	1.3244	1.0297	1.5940	6.25
DC	1.2183	1.3796	1.4397	1.0807	1.6317	6.75

7.4 Density of States

To investigate the metallic vs. insulating characteristics of the states presented in the phase diagram, the density of states has been analyzed. The results are shown in Fig.7.5. The situation for the G-AFM state is clear: the state is an insulator with a robust gap. The Block-AFM state involving spin blocks is also insulating, as discussed above. This can be understood since in the Block-state there are no paths from one extreme to the other of the crystal with spins displaying the same spin orientation.

The C-AFM state is metallic, in agreement with previous calculations [Luo et al. (2010)], and the DC state is also metallic. This is reasonable since C and DC only differ in the periodicity along the y direction (strictly speaking, for the 8×8 cluster there is a tiny gap in the DOS for the DC-state but this is likely caused by finite-size effects). The E-phase also displays a small gap, but it is difficult to say whether it will become insulating or metallic in the bulk limit. Finally, the Flux state appears to be clearly metallic, while the GC-AFM state is insulating. The latter has this property because it is formed by isolated 2×1 spin blocks, qualitative similar to the characteristics that led to the insulating nature of the Block-AFM state made of isolated 2×2 spin blocks.

7.5 Phase Separation

The phase diagram shown in Fig.7.2 contain regions of phase separation (PS). The conclusion that there are unstable regions with these characteristics in the phase diagram was based on the study of the curvature of the $E(n)$ vs. n curves, where $E(n)$ is the ground state energy at the electronic density n. Phase separation in multiorbital systems occurs in other contexts, such as in double exchange models for manganites [Yunoki et al. (1998a,b); Dagotto et al. (2001, 2003)], thus it is not unexpected to find the same phenomenon in the five-orbital Hubbard model as well. In order to visualize the presence of regions with negative curvature in the $E(n)$ vs.

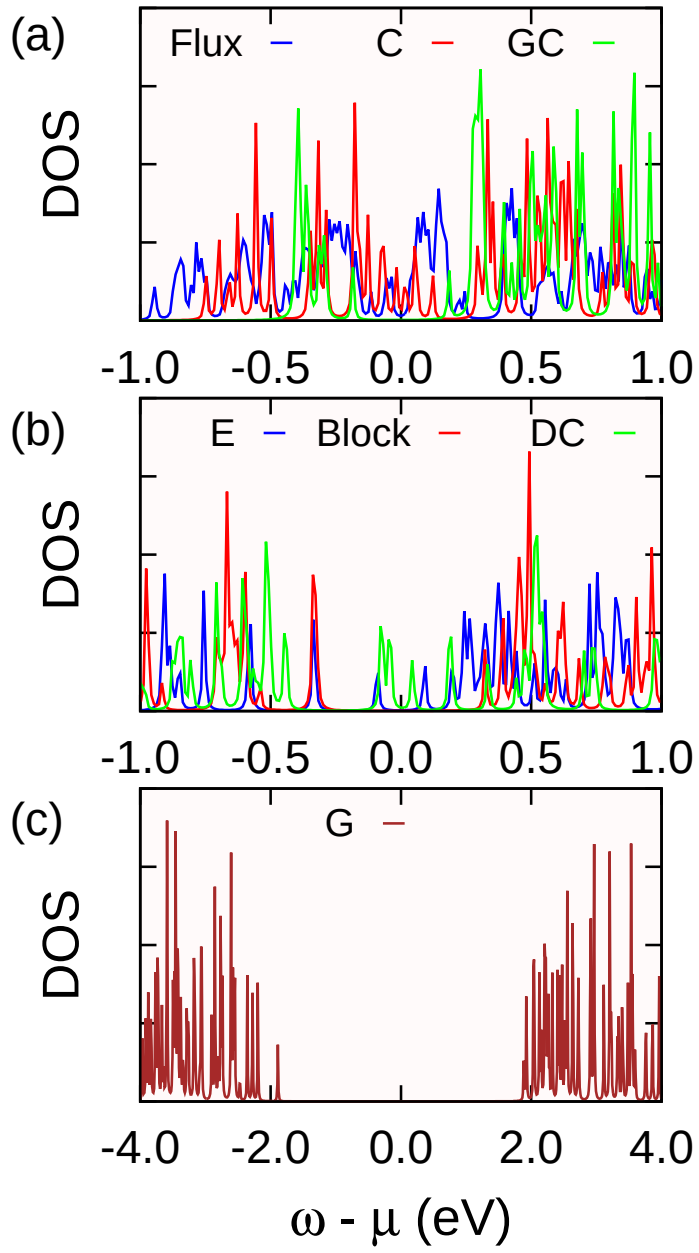

Figure 7.5: Density of States (DOS) at representative values of couplings and densities, corresponding to the seven magnetic states that appear in the phase diagram of Fig. 2. (a) Flux-state (U=3.0, n=6.5); C-state (U=3.0, n=6.0); GC-state (U=3.0, n=5.5); (b) E-state (U=5.0, n=5.75); Block-state (U=5.0, n=6.25); DC-state (U=5.0, n=6.75); (c) G-state (U=3.0, n=5.0).

n curves it is better to introduce $\Delta E(n) = E(n) - E_0(n)$, where $E_0(n)$ is a straight line that joins the energies at the boundary densities of the PS region. Therefore, $\Delta E(n)$ should be positive if $E(n)$ vs. n has a negative curvature. Some representative results are shown in Fig.7.6, where indeed it is clear that PS exist in the regimes of parameter space corresponding to those curves.

The two regions in which the PS state separates are in principle macroscopic in size. However, previous experience with Mn-oxides [Dagotto et al. (2001)] suggest that once other interactions are included, particularly the long-range portion of the Coulomb repulsion between electrons, the PS regions become unstable. This macroscopic separation is replaced instead by complex states that are mixtures, at the nanometer length scale, of the two phases at the boundaries of the PS portions of the phase diagram. In this regime, nonlinear responses to external fields could be expected [Dagotto et al. (2001)].

Note that phase separation was also observed in previous studies of multiorbital Hubbard models, employing related momentum-space mean-field and Heisenberg mean-field techniques, and a different set of hopping amplitudes [Calderón et al. (2012)]. In particular, the PS regions of Ref. [Calderón et al. (2012)] also involve the G and C states as in our results, although in our case the GC state (not included in the study of Ref. [Calderón et al. (2012)]) also plays an important role. Although the agreement is not quantitative, the similarities of both studies suggest that PS must be considered when phase diagrams of multiorbital Hubbard models are constructed. As mentioned before, the presence of PS was also reported in recent related calculations that employed a mean-field approximation to a model with weakly coupled electrons having an electron- and a hole-band with imperfect nesting [Rakhmanov et al. (2013); A.O. Sboychakov and Nori (2013)]. The qualitative agreement with these previous results suggest once again that the PS tendency may be generic and should be considered into future studies, and even in the interpretation of some experiments.

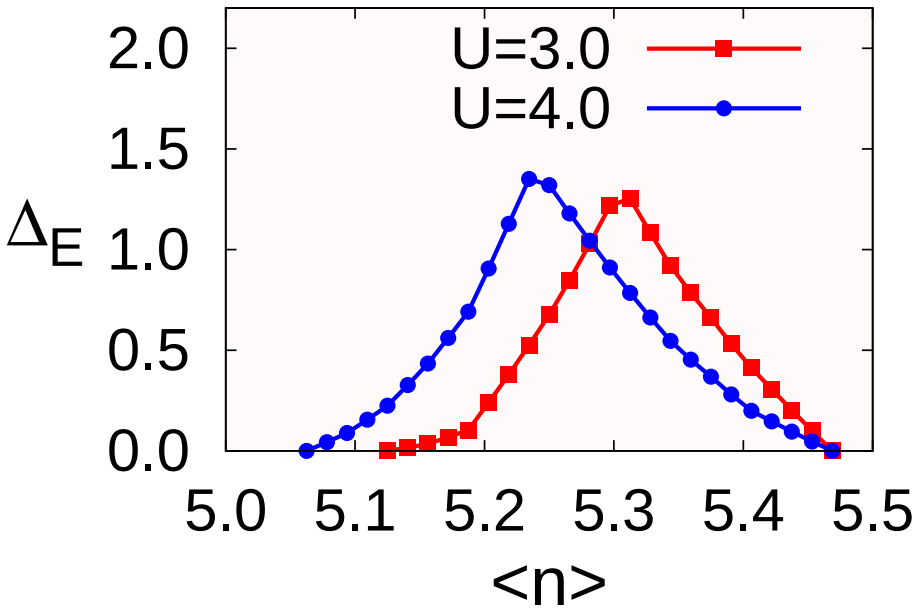

Figure 7.6: Plots of $\Delta E(n)$ vs n showing the existence of negative curvature, namely phase separation. The results were obtained for $U = 4.0$ and $U = 3.0$, $J/U = 0.25$, and in the range of densities indicated. Here $\Delta E(n) = E(n) - E_0(n)$, where $E(n)$ is the actual ground state energy at electronic density n and $E_0(n)$ is a straight line that joins the energies of the two densities at the boundaries of the PS regions.

Chapter 8

Conclusions

This dissertation investigates properties of iron-based superconductors, using multiorbital Hubbard models and the Hartree-Fock approximation, as summarised below.

In Chapter 3, the undoped limit of the multiorbital Hubbard model for pnictides has been studied using a standard mean-field approximation in momentum space. Within this approximation, the magnitude of the order parameter associated with the $(\pi, 0)$ magnetic order was studied varying U and J/U. In addition, the one-particle spectral function $A(\mathbf{k}, \omega)$ was also analyzed. Comparing results against neutron scattering and ARPES experiments, allow us to define regions in parameter space, dubbed "physical regions", where the model Hamiltonian predictions are in qualitative agreement with the above mentioned experiments. These regions are relatively small in size since the ground state in this regime must be simultaneously metallic, magnetic with order parameters in the range found by neutrons, and with Fermi surfaces containing satellite pockets induced by the magnetic state near the Γ-point hole pockets of the original band structure. Although fluctuations beyond the Hartree-Fock approximation are expected to enhance the physical regions, this study still provides important constraints on the couplings to be used for theoretical studies of multiorbital Hubbard models for pnictides.

In Chapter 4, the numerical solution of the two-orbital Hubbard model in the HF approximation away from half-filling has been here discussed. Charge stripes appear at several electronic densities and in a broad range of couplings. The associated spin and orbital properties of the HF states have been discussed as well. However, the relevance of these states to the real pnictides is a matter that still requires further work. On one hand, the charge stripes found here appear to have an associated spin incomensurability. Since neutron scattering results have actually unveiled a similar spin incommensurability in cases where nesting can be excluded, then it is important to search for alternative explanations such as those presented here. In addition, the stripes discussed in this effort can also provide a qualitative rationalization of the nematic order found in STM experiments [Chuang et al. (2010)]. On the other hand, the HF striped states are the more stable at couplings U where the undoped state is an insulator, albeit with a small gap. However, for the hopping sets investigated here, novel (weak) stripes were observed in the magnetic/metallic region, thus avoiding this conceptual problem. But this interesting observation must be confirmed with more refined calculations and using models with more orbitals. In addition, it may occur that the surface of pnictides presents an effective U larger than in the bulk, due to the reduction of the carrier's bandwidth, complicating the analysis. Another issue to consider is that the use of models with more than two orbitals may lead to an effective electronic population in the d_{xz}-d_{yz} sector that is larger than 2.0, and charge stripes, magnetism, and metallicity may coexist in a single state at couplings U larger than those estimated to be realistic from the $\langle n \rangle$=2.0 two-orbital model analysis. All these scenarios are speculative right now, and only further work can clarify the relevance of the striped states presented here to the physics of the pnictides.

Chapter 5 presents real-space Hartree-Fock approximation results for the five-orbital Hubbard model for the case of a $\sqrt{5} \times \sqrt{5}$ arrangement of Fe vacancies. The phase diagram obtained by varying U and J/U contains the magnetic state found in neutron diffraction experiments [Bao et al. (2011)]. This state arises at intermediate couplings U and J/U, and in the phase diagram it is not in contact

with the paramagnetic metallic state of the weak coupling limit. Thus, Fermi surface nesting cannot explain the stability of the AF1 magnetic state in the presence of Fe vacancies [Yin et al. (2012)]. The density of states shows that the AF1 state is an insulator, but since the gap does not present a strong dependence on U its origin may reside in a combination of Hubbard and band-insulator features. In agreement with recent spin [Yu et al. (2011)] and spin-fermion [Yin et al. (2012)] model calculations, several other magnetic phases were found here, suggesting that transitions among these competing states, or among AF1 with and without OO [Lv et al. (2011)], could be observed experimentally particularly by modifications in the carrier's bandwidth.

In Chapter 6, the U/W-J phase diagram of the two-leg ladder compounds $BaFe_2Se_3$ and KFe_2Se_3 was studied using the five-orbital Hubbard model and the real-space Hartree-Fock approximation. The richness of the reported phase diagrams demonstrates that iron based superconductors are more complex than early investigations based on Fermi Surface nesting ideas anticipated [Dai and Dagotto (2012)]. More specifically, in this chapter it has been argued that the experimentally observed CX and 2×2 block-AFM states are indeed the ground state of purely electronic Hubbard models in robust regions of parameter space when varying U/W, J, and the electronic density n, at least within the HF approximation. Our results presented in this chapter suggest that to understand the stability of the 2×2 block states, theoretical studies of electronic models using the geometry of two-leg ladders (much simpler than a full two-dimensional layer) may be sufficient, although for a quantitative description quantum fluctuations and the effect of lattice distortions may be needed. Several other magnetic phases are also predicted to become stable in the vicinity of the CX and block-AFM states in the phase diagram. The experimental search for these states via chemical substitution or pressure would be important to improve the interplay between theory and experiments for the Fe-based superconductors. Since these magnetic arrangements are close in energy, glassy behavior caused by a multiplicity of energy minima is also possible [Saparov et al. (2011)]. Finally, by comparing results using two sets of hopping amplitudes (one

realistic for the ladder selenides and obtained via first-principles calculations, and another borrowed from pnictides investigations), several similarities were unveiled particularly at intermediate and large Hubbard couplings.

Finally, in Chapter 7, the phase diagram of a five-orbital Hubbard model has been presented, working at a fixed Hund coupling $J/U = 0.25$, varying the Hubbard repulsion U and the electronic density n in the range from 5 to 7, and employing the real-space Hartree Fock approximation as the many-body technique. Qualitative trends appear reasonable and moreover they are in good agreement with other independent theoretical investigations, although the results cannot be considered quantitatively accurate, due to the intrinsic deficiencies of mean-field approximations. Three main tendencies have been identified: *(i)* There are multiple magnetic states competing for space in the phase diagram. This is indicative of a complex landscape of free energies. The results are compatible with several states already unveiled experimentally for different compounds [Johnston (2010); Dagotto (2013)], and with other recent mean-field studies as well [Calderón et al. (2012); Bascones et al. (2012)], but there are phases in the present theoretical phase diagram that are novel and worth searching for experimentally. *(ii)* The general tendency in the evolution of the magnetic states with increasing n is to evolve from the G-AFM state at n=5 to states with more ferromagnetic links as n=7 is approached, particularly at robust J/U. *(iii)* There are regions in the phase diagram that present the phenomenon of phase separation. This phenomenon was widely discussed before in manganites [Yunoki et al. (1998a,b); Dagotto et al. (2001, 2003)], but it is only recently that this effect has been mentioned in the context of the iron-based superconductors and their consequences are still unclear. Moreover, the results in this chapter are compatible with theoretical results by other groups that also reported phase separation tendencies [Calderón et al. (2012); Rakhmanov et al. (2013); A.O. Sboychakov and Nori (2013)].

Bibliography

A.O. Sboychakov, A.V. Rozhkov, K. K. A. R. and Nori, F. (2013). Electronic phase separation in iron pnictides. *arXiv:1304.2175*. 90, 95

Bao, W., Huang, Q.-Z., Chen, G.-F., Green, M. A., Wang, D.-M., He, J.-B., and Qiu, Y.-M. (2011). A novel large moment antiferromagnetic order in $K_{0.8}Fe_{1.6}Se_2$ superconductor. *Chinese Physics Letters*, 28(8):086104. xiii, xvi, xvii, 7, 8, 10, 54, 56, 57, 58, 61, 93

Bascones, E., Calderón, M. J., and Valenzuela, B. (2010). Low magnetization and anisotropy in the antiferromagnetic state of undoped iron pnictides. *Phys. Rev. Lett.*, 104:227201. 14

Bascones, E., Valenzuela, B., and Calderón, M. J. (2012). Orbital differentiation and the role of orbital ordering in the magnetic state of Fe superconductors. *Phys. Rev. B*, 86:174508. 76, 95

Boeri, L., Dolgov, O. V., and Golubov, A. A. (2008). Is $LaFeAsO_{1-x}F_x$ an electron-phonon superconductor? *Phys. Rev. Lett.*, 101:026403. 43

Bondino, F., Magnano, E., Malvestuto, M., Parmigiani, F., McGuire, M. A., Sefat, A. S., Sales, B. C., Jin, R., Mandrus, D., Plummer, E. W., Singh, D. J., and Mannella, N. (2008). Evidence for strong itinerant spin fluctuations in the normal state of $CeFeAsO_{0.89}F_{0.11}$ iron-oxypnictide superconductors. *Phys. Rev. Lett.*, 101:267001. 76

Cai, P., Ye, C., Ruan, W., Zhou, X., Wang, A., Zhang, M., Chen, X., and Wang, Y. (2012). Imaging the coexistence of a superconducting phase and a charge-density modulation in the $K_{0.73}Fe_{1.67}Se_2$ superconductor using a scanning tunneling microscope. *Phys. Rev. B*, 85:094512. 9

Calderón, M. J., León, G., Valenzuela, B., and Bascones, E. (2012). Magnetic interactions in iron superconductors studied with a five-orbital model within the Hartree-Fock and Heisenberg approximations. *Phys. Rev. B*, 86:104514. 76, 79, 82, 90, 95

Caldern, M. J., Valenzuela, B., and Bascones, E. (2009). Effect of tetrahedral distortion on the electronic properties of iron pnictides. *New Journal of Physics*, 11(1):013051. 14

Cao, C. and Dai, J. (2011a). Block spin ground state and three-dimensionality of $(K,Tl)_yFe_{1.6}Se_2$. *Phys. Rev. Lett.*, 107:056401. xvii, 10, 57, 58

Cao, C. and Dai, J. (2011b). Electronic structure and Mott localization of iron-deficient $TlFe_{1.5}Se_2$ with superstructures. *Phys. Rev. B*, 83:193104. xvii, 10, 57, 58

Cao, C., Hirschfeld, P. J., and Cheng, H.-P. (2008). Proximity of antiferromagnetism and superconductivity in $LaFeAsO_{1-x}F_x$: Effective hamiltonian from *ab initio* studies. *Phys. Rev. B*, 77:220506. 14, 26

Caron, J. M., Neilson, J. R., Miller, D. C., Arpino, K., Llobet, A., and McQueen, T. M. (2012). Orbital-selective magnetism in the spin-ladder iron selenides $Ba_{1-x}K_xFe_2Se_3$. *Phys. Rev. B*, 85:180405. xiii, 10, 11, 12, 63, 65, 71

Caron, J. M., Neilson, J. R., Miller, D. C., Llobet, A., and McQueen, T. M. (2011). Iron displacements and magnetoelastic coupling in the antiferromagnetic spin-ladder compound $BaFe_2Se_3$. *Phys. Rev. B*, 84:180409. xvii, 10, 12, 63, 64, 65, 67, 68, 70, 71

Chen, F., Xu, M., Ge, Q. Q., Zhang, Y., Ye, Z. R., Yang, L. X., Jiang, J., Xie, B. P., Che, R. C., Zhang, M., Wang, A. F., Chen, X. H., Shen, D. W., Hu, J. P., and Feng, D. L. (2011). Electronic identification of the parental phases and mesoscopic phase separation of $K_xFe_{2-y}Se_2$ superconductors. *Phys. Rev. X*, 1:021020. 7

Chen, W.-Q., Yang, K.-Y., Zhou, Y., and Zhang, F.-C. (2009). Strong coupling theory for superconducting iron pnictides. *Phys. Rev. Lett.*, 102:047006. 14

Chu, J.-H., Analytis, J. G., Kucharczyk, C., and Fisher, I. R. (2009). Determination of the phase diagram of the electron-doped superconductor $Ba(Fe_{1-x}Co_x)_2As_2$. *Phys. Rev. B*, 79:014506. 3

Chuang, T., Allan, M., Lee, J., Xie, Y., Ni, N., Bud'ko, S. L., Boebinger, G. S., Canfield, P. C., and Davis, J. (2010). Nematic electronic structure in the "parent" state of the iron-based superconductor $Ca(Fe_{1-x}Co_x)_2As_2$. *Science*, 327(5962):181. 42, 47, 50, 93

Daghofer, M., Luo, Q.-L., Yu, R., Yao, D. X., Moreo, A., and Dagotto, E. (2010a). Orbital-weight redistribution triggered by spin order in the pnictides. *Phys. Rev. B*, 81:180514. 14, 31, 33, 47

Daghofer, M., Moreo, A., Riera, J. A., Arrigoni, E., Scalapino, D. J., and Dagotto, E. (2008). Model for the magnetic order and pairing channels in Fe pnictide superconductors. *Phys. Rev. Lett.*, 101:237004. xv, xvi, 14, 41, 43, 44, 46, 48, 49, 52

Daghofer, M., Nicholson, A., Moreo, A., and Dagotto, E. (2010b). Three orbital model for the iron-based superconductors. *Phys. Rev. B*, 81:014511. 14, 28, 29, 31, 33, 55, 66

Dagotto, E. (1999). Experiments on ladders reveal a complex interplay between a spin-gapped normal state and superconductivity. *Reports on Progress in Physics*, 62(11):1525. 10, 64

Dagotto, E. (2013). Colloquium : The unexpected properties of alkali metal iron selenide superconductors. *Rev. Mod. Phys.*, 85:849–867. 1, 9, 63, 76, 80, 82, 95

Dagotto, E., Burgy, J., and Moreo, A. (2003). Nanoscale phase separation in colossal magnetoresistance materials: lessons for the cuprates? *Solid State Communications*, 126(12):9 – 22. 88, 95

Dagotto, E., Hotta, T., and Moreo, A. (2001). Colossal magnetoresistant materials: the key role of phase separation. *Physics Reports*, 344(13):1 – 153. 15, 53, 88, 90, 95

Dagotto, E. and Rice, T. (1996). Surprises on the way from One- to Two-dimensional quantum magnets: The ladder materials. *Science*, 271:618–623. 10

Dagotto, E., Riera, J., and Scalapino, D. (1992). Superconductivity in ladders and coupled planes. *Phys. Rev. B*, 45:5744–5747. 10

Dai, Pengcheng, H. J. and Dagotto, E. (2012). Magnetism and its microscopic origin in iron-based high-temperature superconductors. *Nature Physics*, 8:709718. 7, 27, 55, 63, 70, 75, 77, 80, 94

Drew, A. J., Niedermayer, C., Baker, P. J., Pratt, F. L., Blundell, S. J., Lancaster, T., Liu, R. H., Wu, G., Chen, X. H., Watanabe, I., Malik, V. K., A.Dubroka, Rossle, M., Kim, K. W., Baines, C., and Bernhard, C. (2009). Coexistence of static magnetism and superconductivity in $SmFeAsO_{1-x}F_x$ as revealed by muon spin rotation. *Nature Materials*, 8:310–314. xii, 3, 5

Emery, V. J., Kivelson, S. A., and Tranquada, J. M. (1999). Stripe phases in high-temperature superconductors. *Proceedings of the National Academy of Sciences*, 96(16):8814–8817. 42

Fang, C., Xu, B., Dai, P., Xiang, T., and Hu, J. (2012). Magnetic frustration and iron-vacancy ordering in iron chalcogenide. *Phys. Rev. B*, 85:134406. 10

Fang, M.-H., Wang, H.-D., Dong, C.-H., Li, Z.-J., Feng, C.-M., Chen, J., and Yuan, H. Q. (2011). Fe-based superconductivity with T_c =31K bordering an antiferromagnetic insulator in (Tl,K)Fe_xSe_2. *EPL (Europhysics Letters)*, 94(2):27009. 7

Fobes, D., Zaliznyak, I. A., Xu, Z., Zhong, R., Gu, G., Tranquada, J. M., Harriger, L., Singh, D., Garlea, V. O., Lumsden, M., and Winn, B. (2013). Ferro-orbital ordering transition in iron telluride Fe_{1+y}Te(y=0.09(1)). *arXiv:1307.7162*. 83

Graser, S., Maier, T. A., Hirschfeld, P. J., and Scalapino, D. J. (2009). Near-degeneracy of several pairing channels in multiorbital models for the Fe pnictides. *New J. Phys.*, 11(2):025016 (34pp). xi, 14, 28, 37, 41, 55, 57, 65, 66, 68, 77, 114

Gretarsson, H., Lupascu, A., Kim, J., Casa, D., Gog, T., Wu, W., Julian, S. R., Xu, Z. J., Wen, J. S., Gu, G. D., Yuan, R. H., Chen, Z. G., Wang, N.-L., Khim, S., Kim, K. H., Ishikado, M., Jarrige, I., Shamoto, S., Chu, J.-H., Fisher, I. R., and Kim, Y.-J. (2011). Revealing the dual nature of magnetism in iron pnictides and iron chalcogenides using x-ray emission spectroscopy. *Phys. Rev. B*, 84:100509. 76

Guo, J., Jin, S., Wang, G., Wang, S., Zhu, K., Zhou, T., He, M., and Chen, X. (2010). Superconductivity in the iron selenide $K_xFe_2Se_2$ ($0 \leq x \leq 1.0$). *Phys. Rev. B*, 82:180520. 7, 54, 63

Hotta, T., Moraghebi, M., Feiguin, A., Moreo, A., Yunoki, S., and Dagotto, E. (2003). Unveiling new magnetic phases of undoped and doped Manganites. *Phys. Rev. Lett.*, 90:247203. 82

Hotta, T., Takada, Y., Koizumi, H., and Dagotto, E. (2000). Topological scenario for stripe formation in manganese oxides. *Phys. Rev. Lett.*, 84:2477–2480. 61

Ishida, H. and Liebsch, A. (2010). Fermi-liquid, non-Fermi-liquid, and Mott phases in iron pnictides and cuprates. *Phys. Rev. B*, 81:054513. 35

Jayasekara, W., Lee, Y., Pandey, A., Tucker, G. S., Sapkota, A., Lamsal, J., Calder, S., Abernathy, D. L., Niedziela, J. L., Harmon, B. N., Kreyssig, A., Vaknin, D., Johnston, D. C., Goldman, A. I., and McQueeney, R. J. (2013). Stripe antiferromagnetic spin fluctuations in $SrCo_2As_2$. *Phys. Rev. Lett.*, 111:157001. 13, 82

Johnson, D. D. (1988). Modified Broyden's method for accelerating convergence in self-consistent calculations. *Phys. Rev. B*, 38:12807–12813. 57

Johnston, D. (2010). The puzzle of high temperature superconductivity in layered iron pnictides and chalcogenides. *Advances in Physics*, 59(6):803–1061. 1, 3, 63, 80, 95

Kamihara, Y., Watanabe, T., Hirano, M., and Hosono, H. (2008). Iron-based layered superconductor $La[O_{1-x}F_x]FeAs$ (x = 0.050.12) with T_c = 26 K. *Journal of the American Chemical Society*, 130(11):3296–3297. 1, 2

Khasanov, R., Bendele, M., Amato, A., Babkevich, P., Boothroyd, A. T., Cervellino, A., Conder, K., Gvasaliya, S. N., Keller, H., Klauss, H.-H., Luetkens, H., Pomjakushin, V., Pomjakushina, E., and Roessli, B. (2009). Coexistence of incommensurate magnetism and superconductivity in $Fe_{1+y}Se_xTe_{1-x}$. *Phys. Rev. B*, 80:140511. 3

Korshunov, M. M. and Eremin, I. (2008). Theory of magnetic excitations in iron-based layered superconductors. *Phys. Rev. B*, 78:140509. 14

Ku, W., Rosner, H., Pickett, W. E., and Scalettar, R. T. (2002). Insulating ferromagnetism in $La_4Ba_2Cu_2O_{10}$: An *Ab Initio* wannier function analysis. *Phys. Rev. Lett.*, 89:167204. 66

Kuroki, K., Onari, S., Arita, R., Usui, H., Tanaka, Y., Kontani, H., and Aoki, H. (2008). Unconventional pairing originating from the disconnected fermi surfaces of superconducting $LaFeAsO_{1-x}F_x$. *Phys. Rev. Lett.*, 101:087004. 14, 41

Laad, M. S. and Craco, L. (2009). Theory of multiband superconductivity in iron pnictides. *Phys. Rev. Lett.*, 103:017002. 14

Lamsal, J., Tucker, G. S., Heitmann, T. W., Kreyssig, A., Jesche, A., Pandey, A., Tian, W., McQueeney, R. J., Johnston, D. C., and Goldman, A. I. (2013). Persistence of local-moment antiferromagnetic order in $Ba_{1-x}K_xMn_2As_2$. *Phys. Rev. B*, 87:144418. 12

Laplace, Y., Bobroff, J., Rullier-Albenque, F., Colson, D., and Forget, A. (2009). Atomic coexistence of superconductivity and incommensurate magnetic order in the pnictide $Ba(Fe_{1-x}Co_x)_2As_2$. *Phys. Rev. B*, 80:140501. 42

Lee, C.-C., Yin, W.-G., and Ku, W. (2009). Ferro-orbital order and strong magnetic anisotropy in the parent compounds of iron-pnictide superconductors. *Phys. Rev. Lett.*, 103:267001. 14

Lee, C. H., Kihou, K., Kawano-Furukawa, H., Saito, T., Iyo, A., Eisaki, H., Fukazawa, H., Kohori, Y., Suzuki, K., Usui, H., Kuroki, K., and Yamada, K. (2011). Incommensurate spin fluctuations in hole-overdoped superconductor KFe_2As_2. *Phys. Rev. Lett.*, 106:067003. 41

Lee, P. A. and Wen, X.-G. (2008). Spin-triplet p-wave pairing in a three-orbital model for iron pnictide superconductors. *Phys. Rev. B*, 78:144517. 14

Lee, S.-H., Xu, G., Ku, W., Wen, J. S., Lee, C. C., Katayama, N., Xu, Z. J., Ji, S., Lin, Z. W., Gu, G. D., Yang, H.-B., Johnson, P. D., Pan, Z.-H., Valla, T., Fujita, M., Sato, T. J., Chang, S., Yamada, K., and Tranquada, J. M. (2010). Coupling of spin and orbital excitations in the iron-based superconductor $FeSe_{0.5}Te_{0.5}$. *Phys. Rev. B*, 81:220502. 41

Lei, H., Ryu, H., Frenkel, A. I., and Petrovic, C. (2011). Anisotropy in $BaFe_2Se_3$ single crystals with double chains of FeSe tetrahedra. *Phys. Rev. B*, 84:214511. 10, 12, 63, 64, 70, 72

Lester, C., Chu, J.-H., Analytis, J. G., Perring, T. G., Fisher, I. R., and Hayden, S. M. (2010). Dispersive spin fluctuations in the nearly optimally doped superconductor $Ba(Fe_{1-x}Co_x)_2As_2$ (x=0.065). *Phys. Rev. B*, 81:064505. 42

Li, S., de la Cruz, C., Huang, Q., Chen, Y., Lynn, J. W., Hu, J., Huang, Y.-L., Hsu, F.-C., Yeh, K.-W., Wu, M.-K., and Dai, P. (2009). First-order magnetic and structural phase transitions in $Fe_{1+y}Se_xTe_{1-x}$. *Phys. Rev. B*, 79:054503. 82

Li, W., Dong, S., Fang, C., and Hu, J. (2012). Block antiferromagnetism and checkerboard charge ordering in the alkali-doped iron selenides $R_{1-x}Fe_{2-y}Se_2$. *Phys. Rev. B*, 85:100407. 82

Liang, S., Alvarez, G., Şen, C., Moreo, A., and Dagotto, E. (2012). Anisotropy of electrical transport in pnictide superconductors studied using Monte Carlo simulations of the Spin-Fermion model. *Phys. Rev. Lett.*, 109:047001. 79

Liang, S., Moreo, A., and Dagotto, E. (2013). Nematic state of pnictides stabilized by interplay between spin, orbital, and lattice degrees of freedom. *Phys. Rev. Lett.*, 111:047004. 79

Lorenzana, J., Seibold, G., Ortix, C., and Grilli, M. (2008). Competing orders in FeAs layers. *Phys. Rev. Lett.*, 101:186402. 14, 44, 80

Luca de' Medici, Gianluca Giovannetti, M. C. (2012). Selective mottness as a key to iron superconductors. *arXiv:1212.3966*. 76, 79

Luetkens, H., Klauss, H.-H., Kraken, M., Litterst, F. J., Dellmann, T., Klingeler, R., Hess, C., Khasanov, R., Amato, A., Baines, C., Kosmala, M., Schumann, O. J., Braden, M., Hamann-Borrero, J., Leps, N., Kondrat, A., Behr, G., Werner, J., and Buchner, B. (2009). The electronic phase diagram of the $LaO_{1-x}F_xFeAs$ superconductor. *Nature Materials*, 8:305–309. 3

Lumsden, M. D. and Christianson, A. D. (2010). Magnetism in Fe-based superconductors. *Journal of Physics: Condensed Matter*, 22(20):203203. xii, 1, 2

Luo, Q., Martins, G., Yao, D.-X., Daghofer, M., Yu, R., Moreo, A., and Dagotto, E. (2010). Neutron and ARPES constraints on the couplings of the multiorbital hubbard model for the iron pnictides. *Phys. Rev. B*, 82:104508. 49, 55, 59, 68, 70, 77, 88

Luo, Q., Nicholson, A., Riera, J., Yao, D.-X., Moreo, A., and Dagotto, E. (2011). Magnetic state of $K_{0.8}Fe_{1.6}Se_2$ from a five-orbital Hubbard model in the Hartree-Fock approximation. *Phys. Rev. B*, 84:140506. 70, 82

Luo, Q., Nicholson, A., Rincón, J., Liang, S., Riera, J., Alvarez, G., Wang, L., Ku, W., Samolyuk, G. D., Moreo, A., and Dagotto, E. (2013). Magnetic states of the two-leg-ladder alkali metal iron selenides AFe_2Se_3. *Phys. Rev. B*, 87:024404. 80, 82

Lv, W., Lee, W.-C., and Phillips, P. (2011). Vacancy-driven orbital and magnetic order in $(K,Tl,Cs)_yFe_{2-x}Se_2$. *Phys. Rev. B*, 84:155107. 55, 59, 94

Lynn, J. W. and Dai, P. (2009). Neutron studies of the iron-based family of high T_c magnetic superconductors. *Physica C: Superconductivity*, 469(912):469 – 476. xii, 1, 2, 3, 4

Margadonna, S., Takabayashi, Y., McDonald, M. T., Brunelli, M., Wu, G., Liu, R. H., Chen, X. H., and Prassides, K. (2009). Crystal structure and phase transitions across the metal-superconductor boundary in the $SmFeAsO_{1-x}F_x$ (0¡x¡0.20) family. *Phys. Rev. B*, 79:014503. 3

Mazin, I. I. and Johannes, M. D. (2009). A key role for unusual spin dynamics in ferropnictides. *Nature Physics*, 5:141145. 45

Misawa, T., Nakamura, K., and Imada, M. (2012). *Ab Initio* evidence for strong correlation associated with Mott proximity in iron-based superconductors. *Phys. Rev. Lett.*, 108:177007. 76, 79

Miyake, T., Nakamura, K., Arita, R., and Imada, M. (2010). Comparison of *Ab initio* low-energy models for LaFePO, LaFeAsO, $BaFe_2As_2$, LiFeAs, FeSe, and FeTe: Electron correlation and covalency. *Journal of the Physical Society of Japan*, 79(4):044705. 35

Moreo, A., Daghofer, M., Nicholson, A., and Dagotto, E. (2009a). Interband pairing in multiorbital systems. *Phys. Rev. B*, 80:104507. 14

Moreo, A., Daghofer, M., Riera, J. A., and Dagotto, E. (2009b). Properties of a two-orbital model for oxypnictide superconductors: Magnetic order, B_{2g} spin-singlet pairing channel, and its nodal structure. *Phys. Rev. B*, 79:134502. xv, xvi, 14, 41, 43, 44, 46, 48, 49, 52

Nambu, Y., Ohgushi, K., Suzuki, S., Du, F., Avdeev, M., Uwatoko, Y., Munakata, K., Fukazawa, H., Chi, S., Ueda, Y., and Sato, T. J. (2012). Block magnetism coupled with local distortion in the iron-based spin-ladder compound $BaFe_2Se_3$. *Phys. Rev. B*, 85:064413. 10, 12, 63, 68, 72

Nicholson, A., Ge, W., Zhang, X., Riera, J., Daghofer, M., Oleś, A. M., Martins, G. B., Moreo, A., and Dagotto, E. (2011). Competing pairing symmetries in a generalized two-orbital model for the pnictide superconductors. *Phys. Rev. Lett.*, 106:217002. 43, 50

Nomura, T. and Yamada, K. (2000). Magnetic properties of quasi-two-dimensional ruthenates
studied by mean field theoretical approach. *Journal of the Physical Society of Japan*, 69(6):1856–1864. 19

Oleś, A. M. (1983). Antiferromagnetism and correlation of electrons in transition metals. *Phys. Rev. B*, 28:327–339. 27, 44

Poilblanc, D. and Rice, T. M. (1989). Charged solitons in the Hartree-Fock approximation to the large- U Hubbard model. *Phys. Rev. B*, 39:9749–9752. 42

Raghu, S., Qi, X.-L., Liu, C.-X., Scalapino, D. J., and Zhang, S.-C. (2008). Minimal two-band model of the superconducting iron oxypnictides. *Phys. Rev. B*, 77:220503. xv, 14, 41, 43, 50, 51

Rakhmanov, A. L., Rozhkov, A. V., Sboychakov, A. O., and Nori, F. (2013). Phase separation of antiferromagnetic ground states in systems with imperfect nesting. *Phys. Rev. B*, 87:075128. 90, 95

Ricci, A., Poccia, N., Campi, G., Joseph, B., Arrighetti, G., Barba, L., Reynolds, M., Burghammer, M., Takeya, H., Mizuguchi, Y., Takano, Y., Colapietro, M., Saini, N. L., and Bianconi, A. (2011). Nanoscale phase separation in the iron chalcogenide superconductor $K_{0.8}Fe_{1.6}Se_2$ as seen via scanning nanofocused x-ray diffraction. *Phys. Rev. B*, 84:060511. 7, 54

Saparov, B., Calder, S., Sipos, B., Cao, H., Chi, S., Singh, D. J., Christianson, A. D., Lumsden, M. D., and Sefat, A. S. (2011). Spin glass and semiconducting behavior in one-dimensional $BaFe_{2-\delta}Se_3$ ($\delta \approx 0.2$) crystals. *Phys. Rev. B*, 84:245132. 10, 12, 63, 94

Schrieffer, J. R., Wen, X. G., and Zhang, S. C. (1989). Dynamic spin fluctuations and the bag mechanism of high-T_c superconductivity. *Phys. Rev. B*, 39:11663–11679. 27

Schwarz, K., Blaha, P., and Madsen, G. (2002). Electronic structure calculations of solids using the WIEN2k package for material sciences. *Computer Physics Communications*, 147(12):71 – 76. 65

Seo, K., Bernevig, B. A., and Hu, J. (2008). Pairing symmetry in a Two-orbital exchange coupling model of oxypnictides. *Phys. Rev. Lett.*, 101:206404. 14, 41

Shimojima, T., Ishizaka, K., Ishida, Y., Katayama, N., Ohgushi, K., Kiss, T., Okawa, M., Togashi, T., Wang, X.-Y., Chen, C.-T., Watanabe, S., Kadota, R., Oguchi, T., Chainani, A., and Shin, S. (2010). Orbital-dependent modifications of electronic structure across the magnetostructural transition in $BaFe_2As_2$. *Phys. Rev. Lett.*, 104:057002. 26, 33

Si, Q. and Abrahams, E. (2008). Strong correlations and magnetic frustration in the high T_c iron pnictides. *Phys. Rev. Lett.*, 101:076401. 14, 41

Singh, Y., Green, M. A., Huang, Q., Kreyssig, A., McQueeney, R. J., Johnston, D. C., and Goldman, A. I. (2009). Magnetic order in $BaMn_2As_2$ from neutron diffraction measurements. *Phys. Rev. B*, 80:100403. 12, 79

Sknepnek, R., Samolyuk, G., Lee, Y.-b., and Schmalian, J. (2009). Anisotropy of the pairing gap of FeAs-based superconductors induced by spin fluctuations. *Phys. Rev. B*, 79:054511. 14

Svitlyk, V., Chernyshov, D., Pomjakushina, E., Krzton-Maziopa, A., Conder, K., Pomjakushin, V., Pttgen, R., and Dmitriev, V. (2013). Crystal structure of $BaFe_2Se_3$ as a function of temperature and pressure: phase transition phenomena and high-order expansion of Landau potential. *Journal of Physics: Condensed Matter*, 25(31):315403. 10, 63

Wang, C., Li, L., Chi, S., Zhu, Z., Ren, Z., Li, Y., Wang, Y., Lin, X., Luo, Y., Jiang, S., Xu, X., Cao, G., and Xu, Z. (2008). Thorium-dopinginduced superconductivity up to 56k in gd 1x th x feaso. *EPL (Europhysics Letters)*, 83(6):67006. 1

Wang, K., Lei, H., and Petrovic, C. (2011a). Thermoelectric studies of $K_xFe_{2-y}Se_2$ indicating a weakly correlated superconductor. *Phys. Rev. B*, 83:174503. 54

Wang, X., Daghofer, M., Nicholson, A., Moreo, A., Guidry, M., and Dagotto, E. (2010). Constraints imposed by symmetry on pairing operators for the iron pnictides. *Phys. Rev. B*, 81:144509. 14

Wang, X.-P., Qian, T., Richard, P., Zhang, P., Dong, J., Wang, H.-D., Dong, C.-H., Fang, M.-H., and Ding, H. (2011b). Strong nodeless pairing on separate electron Fermi surface sheets in (Tl,K)$Fe_{1.78}Se_2$ probed by ARPES. *EPL (Europhysics Letters)*, 93(5):57001. xiii, 7, 9, 54

Wei Li, Hao Ding, P. D. K. C. C. S. K. H. L. W. X. M. J.-P. H. X. C. and Xue, Q.-K. (2012). Phase separation and magnetic order in K-doped iron selenide superconductor. *Nature Physics*, 8:126–130. 9

Wei Li, Hao Ding, P. Z. P. D. K. C. K. H. S. J. L. W. X. M. J. W. J.-P. H. Q.-K. X. X. C. (2012a). Superconductivity in a single layer alkali-doped FeSe: a weakly coupled two-leg ladder system. *arXiv:1210.4619*. 64

Wei Li, Chandan Setty, X. H. C. J. H. (2012b). Electronic and magnetic structures of chain structured iron selenide compounds. *arXiv:1202.4016*. 64

Yan, X.-W., Gao, M., Lu, Z.-Y., and Xiang, T. (2011). Ternary iron selenide $K_{0.8}Fe_{1.6}Se_2$ is an antiferromagnetic semiconductor. *Phys. Rev. B*, 83:233205. 10

Yanagi, H., Kawamura, R., Kamiya, T., Kamihara, Y., Hirano, M., Nakamura, T., Osawa, H., and Hosono, H. (2008). Itinerant ferromagnetism in the layered crystals LaCoOX (X=P,As). *Phys. Rev. B*, 77:224431. 13

Yang, L. X., Zhang, Y., Ou, H. W., Zhao, J. F., Shen, D. W., Zhou, B., Wei, J., Chen, F., Xu, M., He, C., Chen, Y., Wang, Z. D., Wang, X. F., Wu, T., Wu, G., Chen, X. H., Arita, M., Shimada, K., Taniguchi, M., Lu, Z. Y., Xiang, T., and Feng, D. L. (2009). Electronic structure and unusual exchange splitting in the spin-density-wave state of the $BaFe_2As_2$ parent compound of iron-based superconductors. *Phys. Rev. Lett.*, 102:107002. 26

Ye, F., Chi, S., Bao, W., Wang, X. F., Ying, J. J., Chen, X. H., Wang, H. D., Dong, C. H., and Fang, M. (2011). Common crystalline and magnetic structure of superconducting $A_2Fe_4Se_5$ (A=K,Rb,Cs,Tl) single crystals measured using neutron diffraction. *Phys. Rev. Lett.*, 107:137003. 7

Yi, M., Lu, D. H., Analytis, J. G., Chu, J.-H., Mo, S.-K., He, R.-H., Hashimoto, M., Moore, R. G., Mazin, I. I., Singh, D. J., Hussain, Z., Fisher, I. R., and Shen, Z.-X. (2009). Unconventional electronic reconstruction in undoped (Ba,Sr)Fe_2As_2 across the spin density wave transition. *Phys. Rev. B*, 80:174510. xii, 3, 6, 33

Yin, W.-G., Lee, C.-C., and Ku, W. (2010). Unified picture for magnetic correlations in iron-based superconductors. *Phys. Rev. Lett.*, 105:107004. xvi, 52, 53, 82

Yin, W.-G., Lin, C.-H., and Ku, W. (2012). Insulating magnetism in vacancy-ordered $K_{0.8}Fe_{1.6}Se_2$. *Phys. Rev. B*, 86:081106. xvii, 10, 55, 57, 58, 59, 61, 94

Yu, R., Goswami, P., and Si, Q. (2011). Magnetic phase diagram of an extended J_1 - J_2 model on a modulated square lattice and its implications for the antiferromagnetic phase of $K_yFe_xSe_2$. *Phys. Rev. B*, 84:094451. xvii, 10, 55, 57, 58, 61, 94

Yu, R., Trinh, K. T., Moreo, A., Daghofer, M., Riera, J. A., Haas, S., and Dagotto, E. (2009). Magnetic and metallic state at intermediate Hubbard U coupling in multiorbital models for undoped iron pnictides. *Phys. Rev. B*, 79:104510. 14, 27, 29, 33, 41, 49, 68, 70

Yunoki, S., Hu, J., Malvezzi, A. L., Moreo, A., Furukawa, N., and Dagotto, E. (1998a). Phase separation in electronic models for Manganites. *Phys. Rev. Lett.*, 80:845–848. 88, 95

Yunoki, S., Moreo, A., and Dagotto, E. (1998b). Phase separation induced by orbital degrees of freedom in models for Manganites with Jahn-Teller phonons. *Phys. Rev. Lett.*, 81:5612–5615. 88, 95

Zaanen, J. and Gunnarsson, O. (1989). Charged magnetic domain lines and the magnetism of high-T_c oxides. *Phys. Rev. B*, 40:7391–7394. 42

Zhang, Y.-Z., Lee, H., Lin, H.-Q., Wu, C.-Q., Jeschke, H. O., and Valentí, R. (2012). General mechanism for orbital selective phase transitions. *Phys. Rev. B*, 85:035123. 70

Zhao, J., Huang, Q., de la Cruz, C., Li, S., Lynn, J. W., Chen, Y., Green, M. A., Chen, G. F., Li, G., Li, Z., Luo, J. L., Wang, N. L., and Dai, P. (2008). Structural and magnetic phase diagram of $CeFeAsO_{1-x}F_x$ and its relation to high-temperature superconductivity. *Nature Materials*, 7(12):953–959. xii, 3, 5

Zhou, S. and Wang, Z. (2010). Electron correlation and spin density wave order in iron pnictides. *Phys. Rev. Lett.*, 105:096401. 35

Appendix

Appendix A

Parameters of Five-orbital Model 1 in Chapter 3

Table A.1: Parameters for the tight-binding portion of the five-orbital Model 1, following a similar notation as in Ref. [Graser et al. (2009)]. The overall energy unit is electron volts.

t_i^{mn}	$i = x$	$i = y$	$i = xy$	$i = xx$	$i = xxy$	$i = xyy$	$i = xxyy$
$mn = 11$	-0.355	-0.17	0.21	-0.1	0.01	0	0
$mn = 33$	0.1		0.137	-0.03			
$mn = 44$	0.193		-0.115	0	0		0
$mn = 55$	-0.213			0	0		0
$mn = 12$			-0.22		0		0
$mn = 13$	-0.35		0.01		0.02		
$mn = 14$	0.55		-0.13		0.01		
$mn = 15$	-0.25		0				0
$mn = 34$					-0.009		
$mn = 35$	0.06				-0.06		
$mn = 45$			-0.05				0

ϵ_{11}	ϵ_{33}	ϵ_{44}	ϵ_{55}
0.31	-0.25	0.43	-0.8

Appendix B

Hopping matrices for the $BaFe_2Se_3$ material obtained from first principles techniques, used in Chapter 6

Table B.1: Hopping matrices for the $BaFe_2Se_3$ material obtained from a tight-binding Wannier function analysis of the first principles results (in eV units). The matrices are written in the orbital basis $\{d_{z^2}, d_{x^2-y^2}, d_{yz}, d_{xz}, d_{xy}\}$. The long (short) direction of the ladder is oriented along the y (x) axis. The convention for the iron site labels is in Fig.6.2.

Matrix	$BaFe_2Se_3$
t^{OnSite}	$\begin{pmatrix} -0.4604 & -0.0617 & 0.0534 & -0.0345 & -0.0178 \\ -0.0617 & -0.5947 & -0.0851 & 0.0371 & 0.0169 \\ 0.0534 & -0.0851 & -0.0719 & -0.0030 & 0.0165 \\ -0.0345 & 0.0371 & -0.0030 & -0.1669 & 0.0286 \\ -0.0178 & 0.0169 & 0.0165 & 0.0286 & -0.1632 \end{pmatrix}$
$t^{\text{NN}}_{\text{leg},1\to 8}$	$\begin{pmatrix} -0.0807 & -0.3276 & -0.0139 & 0.2734 & 0.0456 \\ -0.3276 & -0.2875 & -0.0702 & 0.2661 & 0.0228 \\ 0.0139 & 0.0702 & -0.1477 & -0.0531 & 0.2714 \\ 0.2734 & 0.2661 & 0.0531 & -0.2733 & 0.0373 \\ -0.0456 & -0.0228 & 0.2714 & -0.0373 & -0.0397 \end{pmatrix}$
$t^{\text{NN}}_{\text{leg},1'\to 8}$	$\begin{pmatrix} 0.0497 & -0.2674 & 0.0187 & -0.1186 & -0.0738 \\ -0.2674 & -0.3943 & -0.0388 & -0.3449 & -0.0195 \\ -0.0187 & 0.0388 & -0.0580 & 0.0199 & -0.2689 \\ -0.1190 & -0.3449 & -0.0199 & -0.3107 & -0.0147 \\ 0.0738 & 0.0195 & -0.2689 & 0.0147 & -0.1343 \end{pmatrix}$
$t^{\text{NN}}_{\text{rung},8\to 7}$	$\begin{pmatrix} -0.0421 & 0.2853 & -0.1718 & -0.0162 & 0.0055 \\ 0.2853 & -0.3801 & 0.3311 & 0.0411 & 0.0098 \\ -0.1718 & 0.3311 & -0.2881 & -0.0115 & -0.0259 \\ -0.0162 & 0.0411 & -0.0115 & -0.0058 & -0.2303 \\ 0.0055 & 0.0098 & -0.0259 & -0.2303 & -0.0153 \end{pmatrix}$
$t^{\text{NN}}_{\text{rung},1\to 2'}$	$\begin{pmatrix} -0.0421 & 0.2853 & 0.1718 & -0.0162 & -0.0055 \\ 0.2853 & -0.3801 & -0.3311 & 0.0411 & -0.0098 \\ 0.1718 & -0.3311 & -0.2881 & 0.0115 & -0.0259 \\ -0.0162 & 0.0411 & 0.0115 & -0.0058 & 0.2303 \\ -0.0055 & -0.0098 & -0.0259 & 0.2303 & -0.0153 \end{pmatrix}$
$t^{\text{NNN}}_{2\to 8}$	$\begin{pmatrix} -0.0185 & 0.0054 & 0.1140 & 0.0893 & -0.0721 \\ -0.0159 & -0.0379 & -0.0661 & 0.0603 & -0.0118 \\ -0.1483 & 0.0837 & 0.2117 & 0.0843 & 0.0679 \\ -0.1442 & -0.0490 & 0.0801 & 0.1823 & 0.0559 \\ -0.0879 & -0.0017 & -0.0304 & -0.0529 & 0.0644 \end{pmatrix}$
$t^{\text{NNN}}_{2'\to 8}$	$\begin{pmatrix} -0.0185 & 0.0054 & -0.1140 & 0.0893 & 0.0721 \\ -0.0159 & -0.0379 & 0.0661 & 0.0603 & 0.0118 \\ 0.1483 & -0.0837 & 0.2117 & -0.0843 & 0.0679 \\ -0.1442 & -0.0490 & -0.0801 & 0.1823 & -0.0559 \\ 0.0879 & 0.0017 & -0.0304 & 0.0529 & 0.0644 \end{pmatrix}$

Vita

Qinlong Luo was born in Wuhan, China, where he spent 18 years. He attended the University of Science and Technology of China (USTC) in Hefei, China. After a 4-year study of mathematics and physics, he received his Bachelor of Science degree on Condensed Matter Physics in 2008. After graduation, he chose to continue his education in the Ph.D program at the University of Tennesse, Knoxville. He joined Dr. Dagotto's research group as a Graduate Research Assistant. He focused on the numerical study of the multi-orbital Hubbard model for the iron-based superconductors. During the course of his study towards the Ph.D degree, he attended some conferences and published eight papers as the first author or co-author. He is scheduled to defend his Ph.D. in December 2013.